# FORMATION AND EVOLUTION OF TIN SURFACE DEFECTS DURING CYCLIC MECHANICAL LOADING

by

**Xi Chen**

**A Dissertation**

*Submitted to the Faculty of Purdue University*

*In Partial Fulfillment of the Requirements for the degree of*

**Doctor of Philosophy**


School of Materials Engineering

West Lafayette, Indiana

August 2020

**THE PURDUE UNIVERSITY GRADUATE SCHOOL**
**STATEMENT OF COMMITTEE APPROVAL**

**Dr. Carol A. Handwerker, Co-Chair**
School of Materials Engineering

**Dr. John E. Blendell, Co-Chair**
School of Materials Engineering

**Dr. Eric P. Kvam**
School of Materials Engineering

**Dr. David R. Johnson**
School of Materials Engineering

**Approved by:**
Dr. David Bahr

*For my parents and friends*

# ACKNOWLEDGMENTS

I acknowledge the support of the NSF-DMR under Contract DMR 1610420. I would like to thank Maureen Williams and Daniel Josell at NIST for assistance of Physical Vapor Deposition (PVD) process, and thank Dr. Joon Hyeong Park of Purdue University for assistance with sample fabrication and PVD deposition process.

I am grateful to my advisors----Prof. Carol A. Handwerker and John E. Blendell, and my colleagues---- Thomas C. Reeve, John. R. Holaday, David Lowing, Xianyi Hu, and Congying Wang. Prof. Eric. P. Kvam and David. R. Johnson from Purdue University are also acknowledged for their valuable discussions. Lastly, I want to thank my parents, Airen Chen and Xuemei Zhang for their continuing support and love during my PhD life.

# TABLE OF CONTENTS

# LIST OF TABLES

# LIST OF FIGURES

# ABSTRACT

Stress relaxation in tin films can result in microstructural changes visible on the surface, referred to as "surface defects," and can include whisker and hillock formation, cracking, nucleation of new grains, and grain growth. Sn whiskers are of particular concern for microelectronics reliability in which Sn whiskers growing from component surface and cause catastrophic short-circuiting. While prior research has identified the conditions and mechanisms for surface defect evolution during aging and thermal cycling, the response of tin films due to mechanical stress, especially high frequency vibration, is not fully understood. In practical terms, high frequency vibration is an important source of mechanical stress generation in microelectronics for automotive and aerospace applications. This research, based on high frequency vibration of cantilevers, adds to the existing mechanisms for stress relaxation process in metal thin films, not just for tin films, as well as proposed new mechanisms for such processes.

In the first study, the piezoelectric drive of small atomic force microscopy (AFM) cantilevers vibrated at resonance are used for high frequency cyclic bending experiments. Intermetallic (IMC) formation as well as initial film morphology and thickness (corresponding to surface grain size) all influence the response of tin films for cyclic bending. A laser doppler vibrometer (LDV) system was used to identify the real-time strain along the cantilever during cycling, suggesting that the small strains are responsible for the limited nucleation and growth for defects though the defect density increases with the number of cycles and strain distribution along the cantilever.

In the second study, the effect of larger strains on defect evolution was determined using vibration of larger cantilevers at resonance as a function of number of cycles, frequency, temperature, and whether the vibration was continuous or interrupted for SEM characterization of defect type and density. In addition to typical micro-sized whiskers and hillocks, intragranular breakup (IGB) with intrusions and extrusions and nanowhiskers (NWs) with diameters < 1 $\mu$m were observed. Both increasing number of cycles and strain amplitude/rate promote defect formation for a fixed frequency, with the defect density being strongly frequency dependent.

Vibration at low temperature and interrupting measurements for SEM characterization affected the relative densities. The density of larger surface defects is strongly influenced by interruptions while NW density is almost unaffected. Both low resonant frequency and low T (223 K) promote IGB formation during cyclic bending due to large maximum strain amplitude and

slower diffusion/creep at low T, respectively. Though the overall defect density for low T is smaller than that at room temperature (RT), the response of films is similar to that at RT, indicating the same mechanisms. The defect density decrease at low T is mainly determined by NW formation, and there is a transition from micro-sized surface defects to IGBs for cyclic bending at low T.

This research demonstrated that cyclic bending of cantilevers can be used to quantify the stress relaxation of tin films in an important stress regime for microelectronics and to develop defect mitigation strategies to improve the reliability of interconnects in electronic applications.

# 1. INTRODUCTION

## 1.1 Tin Films in the Electronics Industry

Tin films have been a final finish in the electronics industry for their many excellent properties, such as outstanding performance in corrosion resistance, electrical conductivity and solderability [1]. However, the problem of whiskers and hillocks is a severe concern in tin films. Sn surface defects such as whiskers can grow spontaneously from polycrystalline films even at room temperature (RT) or during aging process. The typical morphology of a Sn whisker is shown in Figure 1.1. Sn whiskers can connect between electronic components as a bridge with maximum length of several millimeters [2]. This causes current leakage and short circuits in industrial components, which will bring catastrophic consequences to the whole integrated circuit.

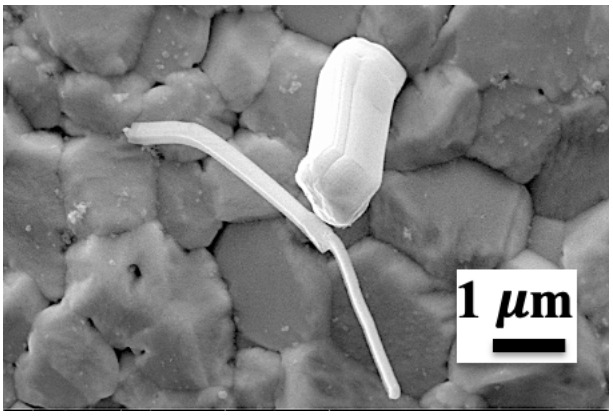


Figure 1.1. SEM image of a Sn whisker formed from the in-plane grain on electroplated films

In 1966, based on the fact that the addition of Pb to tin films greatly reduced the propensity of Sn surface defects, Sn-Pb films become the common practice in electronics industry [3]. Recently, attention to environmental-friendly industry and sustainable development has brought Pb-free films back into the public view [4]. One example is the regional restriction of Pb in electronics industry from “Restriction of Hazardous Substances (RoHS)” established by European Union in 2006. As a consequence, the risk of Sn whiskers and hillocks has come back due to the reliability concerns. To solve this issue, many studies and theoretical research have focused on whisker mitigation strategies and the formation mechanisms of all kinds of Sn surface defects (not only limited to whiskers and hillocks, but also popped grains, sunken grains and irregular growth).

## 1.2 The Properties of $\beta$-Sn

The kinetically stable phase for tin films at and above RT (~298 K) is β-Sn with a low melting temperature of 505 K. β-Sn has a body-centered-tetragonal (BCT) structure (c=0.3183 nm, a=0.5583 nm, c/a ≈0.6) with highly anisotropic thermal expansion and elasticity dependent on the crystallographic directions. For example, the coefficient of thermal expansion (CTE) of c axis is $32\times10^{-6}$/K while that of a axis is only $16.4\times10^{-6}$/K at RT [5]. The stiffness difference between c axis and a axis is also significant with a factor of about 3 at RT. The c-axis has the highest value in CTE and stiffness among all the crystallographic directions.

Since RT is ~0.58 of $\beta$-Sn melting temperature, Coble creep that is dominant at high homologous temperature occurs. Diffusion of atoms is achieved by movement of vacancies along grain boundaries (GBs) in Coble creep process. Thus, several mechanisms happen simultaneously for tin films under stress at RT, including dislocation creep, Coble creep and GB sliding (GBS).

β-Sn has as many as 32 active systems [6], as shown in Table 1.1. Under applied load, the slip of tin films is quite complex due to the variety of slip systems and is highly dependent on the preferred global grain orientation. Not all of the slip systems are activated at once and there are no rules for the possibility of activating slip systems. All these increase the difficulty to analyze and predict the mechanism of tin film deformation.

Table 1.1. Slip systems in $\beta$-Sn crystal

| **Slip system family** | **Number in family** |
|---|---|
| {100} <001> | 2 |
| {110} <001> | 2 |
| {100} <010> | 2 |
| {110} <1$\bar{1}$1>/2 | 4 |
| {110} <1$\bar{1}$0> | 2 |
| {100} <011> | 4 |
| {001} <010> | 2 |
| {001} <110> | 2 |
| {011} <01$\bar{1}$> | 4 |
| {211} <01$\bar{1}$> | 8 |

In addition to the above-mentioned properties of β-Sn, the behavior of tin films under mechanical stress is also highly dependent on the local grain orientation. Specific film grain orientation can lead to high local stress in a limited area, and this may promote the growth of Sn surface defects via diffusion and mass transport as a stress relaxation mechanism for tin films under compressive stress [7,8].

## 1.3 Mechanism of Tin Whisker and Hillock Formation

### 1.3.1 Stress Relaxation Methods

In addition to surface defects formation, other major stress relaxation mechanisms in thin films are creep and diffusion. The dominated stress relaxation mechanism is sensitive to the inherent properties of the film and the environment and test methods the film experiences. An overview of these mechanisms before the specific further discussion on stress relaxation by surface defects can help understand the coupling and competition between these mechanisms, which helps identify the preferred conditions for defect formation.

In additional to Coble creep, Harper--Dorn (HD) creep process, which features the glide or climb of dislocations, is the most common creep behavior of tin films as mentioned by Clore [9]. The creep curve shows a linear relationship between the steady-state creep rate and the stress that is independent of grain size in precious research by Osenbach [10]. The activation energy is mainly the lattice self-diffusion energy, and the climb-controlled dislocation creep mechanism dominates under low stress conditions.

Another mechanism to relax stress is grain growth by material diffusion between grains in the film surface. Thompson [11] observed stress relaxation by stress-driven grain growth in tin films with the nonuniform stress in the grains of the films.

The creep process promotes volumetric growth of tin films while diffusion promotes grain growth, which can function together leading to the third main stress relaxation method in tin films: the formation of surface defects. Sarobol et al. [12] discovered that there are shallow grains with oblique GBs beneath the whisker, as is shown in the cross-section image of Figure 1.2. These shallow grains act as preferred nucleation sites for surface defects with accretion of atoms at the oblique GBs.

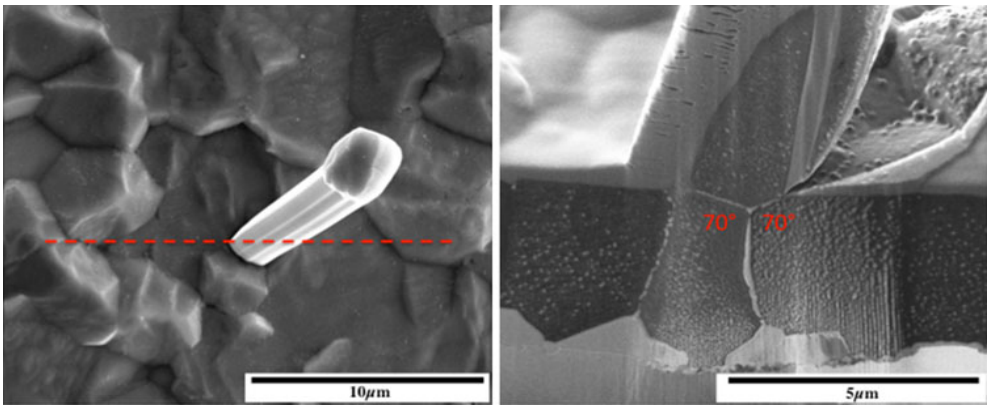


Figure 1.2. SEM image shows the top view (left) and corresponding cross-section view of a whisker with oblique grain boundaries (GBs) beneath it (right). From Acta Materialia, vol. 61, no. 6, Sarobol et al, "Whisker and hillock growth via coupled localized Coble creep, grain boundary sliding, and shear induced grain boundary migration", pp. 1991-2003, copyright 2013, with permission from Elsevier. [12]

### 1.3.2 **The Formation of Hillocks and Whiskers**

There are many issues that need to be taken into consideration when explaining the formation of whiskers and hillocks. The most simplified situation is discussed firstly to get a general idea of the mechanism for surface defect formation. The actual situation can be approached step by step as more parameters are considered in progress.

Firstly, by ignoring local film properties, that is by ignoring the accommodation of compressive stress due to the interaction of neighboring grains in the film, the effects of global film properties on growth of surface defects are focused on. There are many sources of global stresses in electroplated tin films, such as the formation of $Cu_6Sn_5$ intermetallic compounds (IMCs) [8] at the interface between the film and the substrate and residual stress from plating process [13]. The global stress gradients, resulting from the coupling of all the local stress gradients, provide a driving force for surface defect formation. Global grain orientations and strain energy density are the combined effect of all individual strain components that influence surface defect density [14]. To identify and predict the relationship between global film properties and surface defects, the microstructure is simulated due to an actual stress condition and the simulation results is compared with the actual microstructure evolution. The matched results between simulation and experiment results indicate that the simulation can be used to predict defect formation on tin films [14].

Global stress and grain orientation are not enough to explain why nucleation and growth of hillocks and whiskers often appear at a specific local site. With the consideration of local grain

orientations and local stress and strain gradients due to $\beta$-tin anisotropy, a defect growth model that is closer to actual situation can be developed. Local grain orientations of surface defects in the normal direction (ND) to film surface measured by X-ray diffraction (XRD) usually deviate from the dominant global grain orientation significantly [15]. Elastic backscattered diffraction (EBSD) is also an alternative to check local grain orientation by revealing the preferred orientation for surface defects as well as the relationship and difference with neighboring grains [16]. It has been proved that the variations of the overall elastic strain energy density for tin films is a function of simulated texture orientation for elastic stress, which emphasizes the important effect of microstructure on the stress state of films [17]. Nucleation sites for defects are usually grains with the highest out of plane local strain due to the ease of cracking the oxide layer on top of films [1]. Other possible nucleation sites for whiskers are grains that can occur plastic deformation easily in films [18,19]. Since there is no stress relaxation in non-deforming grains, it is confirmed that a stress gradient must exist in films to drive the diffusion process for defect formation [7].

The formation of surface defects is also needed to be taken into consideration for the surface grain geometry [3]. Pre-existing shallow grains with oblique GBs beneath the whisker can act as preferred nucleation sites for whiskers and hillocks with commonly columnar structure for neighboring grains [12,16]. The growth of surface defects can be promoted by the accumulation of Sn atoms at the atomic sink created by the sliding of GBs of surface grains [20].

The origin of surface grains as nuclei for whiskers and hillocks have been much debated, whether surface grains are pre-existing grains from the film deposition process [16], or new grains that formed via surface recrystallization after the deposition process [21,22]. Asymmetrical growth at the whisker root can lead to curved whiskers and hillocks with a change in orientation of the whisker as it grows [23]. The growth morphology for a given whisker and hillock may change over time, and since surface diffusion is suppressed by the presence of the surface oxide, the morphological changes over time are presented in its surface shape [18].

In addition to global and local crystallographic texture as well as grain geometry discussed above, there are other processing parameters influencing defect formation, such as film thickness, composition and orientation relationships between the film and the substrate [17,24,25]. There also exist interactions between various material processes during the formation of surface defects, including but not limited to diffusion, phase transformation and stress relaxation [26]. All these increase the complexity for understanding surface defect formation mechanisms.

### 1.3.3 **Sources of Film Stress**

The compressive stress in tin films provides the driving force for the formation of surface defects [1,7,21,27]. There are many sources of stress, including but not limited to thermally dependent mechanisms due to the mismatch of CTE, $Cu_6Sn_5$ IMC formation due to atom diffusion, residual stress from plating process, oxidation products and externally applied mechanical stress. Since the evolution of these sources of stress is critical to the formation of surface defects, a quick review of these stresses is necessary.

Firstly, the thermal expansion of a constrained material will prompt stress in the film [14]. To simplify the model, the film is often assumed to be thin enough to guarantee constant stress from the free surface of the film to the substrate. For common Sn alloys (such as Sn-Cu, Sn-Pb and Sn-Ag), the CTE of the substrate is usually smaller than or at least equal to that of $a_{Tin}$. At elevated temperature, the film experiences a compressive stress while the substrates experience a tensile stress, and this promotes defect formation. When cooling down to RT or below RT, the stress will be reversed. It leads to defect retraction that is limited by the oxide layer on the film surface. The above process repeats when tin film on a substrate experiences a thermal cycling process [28], and it leads to the evolution of Sn surface defects with decreasing diameter.

For tin films with Sn-Cu alloy or pure Cu layer as the substrate, there always exists an IMC layer composed of $Cu_6Sn_5$ at the interface caused by atom diffusion even at RT [29]. Since the diffusion of Cu into Sn is much faster than that of Sn into Cu, $Cu_6Sn_5$ usually grows preferentially along Sn side. The addition of Cu into tin films causes compressive stress during IMC growth process, and the stress increases with the evolution of IMC from the interface towards tin film surface during aging process.

Due to the variation of electrolytes and electroplating conditions, the plating stress can be compressive or tensile. If the initial plating stress is compressive, surface defects can show up quickly even for room aging after the deposition [14]. Since this stress is produced during the plating process, it is impossible to generate the stress again upon relaxation.

Oxide formation is another source of stress, which is the common response of tin films in high temperature and high humidity environment [30]. When oxygen or $OH^-$ ions diffuse and react with Sn, volume expansion of the film causes lattice strain. Since oxidation layer usually forms at free surface of tin films, the oxidation process is not influenced by the substrate or underlayer [31].

The last but not the least source of stress is externally applied mechanical forces. For example, a static bending test can apply mechanical forces to films [32]. In order to illustrate the relationship between pressure and growth rate of whiskers, Fisher et al [7] did ring type clamp experiment to exert mechanical forces on Sn plated specimens. It was concluded that growth rate of Sn whiskers was enhanced by continuous increasing pressure. There were typically three stages for whisker growth under mechanical pressure: an induction period, a steady growth period and an abrupt slower growth period. For the steady growth period, the growth rate of Sn whiskers varies linearly with mechanical pressure. The whiskers induced by mechanical forces grow rapidly at RT and formation of IMCs may be suppressed due to this high growth rate [33]. All these suggest that the mechanism for Sn surface defect formation due to mechanical force is somewhat different from that of other circumstance, and this emphasizes the importance of research on evolution of tin films due to applied mechanical forces.

The total stress in the film results from the coupling of all above-mentioned stress sources, and all the sources of stress can be dynamic instead of static. They can evolve with time, especially for IMC induced stress and plating stress. For the present research focused on cyclic bending, IMC formation and mechanical forces are the major stress sources that are taken into consideration.

### 1.3.4 **Reported Surface Defect Growth Model**

In order to explain mechanisms for surface defect formation explicitly, researchers have come up with various kinds of models. These models are all based on the consensus that relaxing the compressive stress is the driving force for the formation of surface defects. All established models lay a foundation for the future research of tin films and surface defect formation.

In Lee and Lee's model [1], for a constant in plane biaxial stress, grains with different orientations lead to different strain in the ND to the free surface of the film due to the anisotropic elasticity. Thus, cracking of the oxidation layer of Sn free surface occurs with different strains for whisker formation. The crystallographic orientation of whiskers is usually different from the preferred orientation of the film. Whiskers grow through the cracks, which acts as a mechanism to relieve the compressive stress induced by the formation of $Cu_6Sn_5$ IMCs. The formation of non-flat IMCs in the GBs of the tin film and the interface between the tin film and bronze substrate is shown clearly in Figure 1.3.

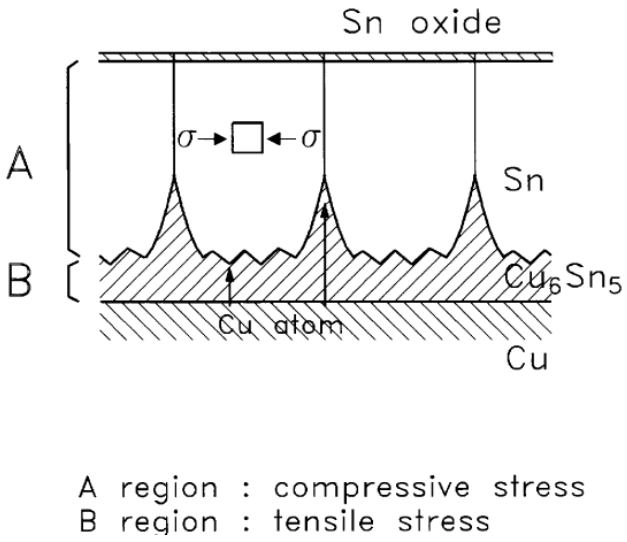


Figure 1.3. A schematic diagram shows the formation of $Cu_6Sn_5$ in interface between tin film and the substrate as well as GBs. From Acta Materialia, vol. 46, no. 10, B.Z. Lee and D.N. Lee, "Spontaneous growth mechanism of tin whiskers", pp. 3701-3714, copyright 1998, with permission from Elsevier. [1]

Tu et al [24] emphasized the role of Sn oxide in whisker formation. The oxidation layer inhibits the source and sink of vacancies on tin film surfaces and prevents the migration of Sn lattice planes, which makes it difficult to relief the compressive stress caused by IMC formation. The stress gradient caused by cracking the surface oxide layer prompts the diffusion of Sn atoms, which finally leads to whisker growth by long-range mass transport. The oxidation of whisker surfaces confines whiskers to grow in one dimensional direction by blocking lateral growth, which can be seen clearly in Figure 1.4. Vacancies sink at the whisker base due to crack of oxidation layer helps sustain whisker growth.

Boettinger et al. [21] put forward an idea that GB migration leads to hillock formation while GB pinning leads to whisker formation, and equiaxial grains prevent Sn defect formation. Stress relaxation mechanisms of pure Sn, Sn-Cu and Sn-Pb electrodeposits vary due to the grain morphology and mobility of GBs. Pure Sn has a columnar grain structure with easy GB migration, so hillocks are pervasive. Sn-Cu alloy with pinned GBs promotes the upward motion of material and thus forms whiskers. Sn-Pb alloy allows for a uniform accretion of Sn due to its non-columnar structure. The strain-rate associated creep is much higher than that for whisker growth, thus whisker growth is not the dominate stress-relaxation mechanism in Sn-Pb films. The detailed illustration of the grain morphology in different material is shown clearly in Figure 1.5. Boettinger

also set up a model for whisker growth from a columnar grain structure under biaxial compressive stress. This model assesses the GB diffusion path through a three-dimensional network of columnar grain faces connecting to oblique grain faces near the deposit surface. The path of Sn atoms to relieve stress is along columnar grain faces within the deposit, through the triple lines, and across the oblique faces. Accretion of Sn on these faces provides the driving force for whisker formation above the deposit surface, as shown in Figure 1.6.

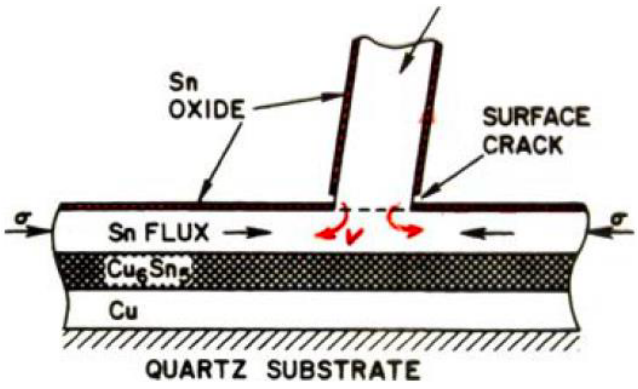


Figure 1.4. A schematic diagram shows the oxidation on the surface of Sn whiskers. From Journal of Materials Science, vol. 18, no. 13, Tu et al, "Stress analysis of spontaneous Sn whisker growth", pp. 269-281, copyright 2007, with permission from Springer Nature. [24]

Vianco et al. [4] proposed that the formation of surface defects is related to dynamic recrystallization (DRX). Due to the higher driving force for recrystallization than that for grain growth, recrystallization is favorable to reduce strain energy for tin films experiencing mechanical force. The growth of whiskers and hillocks, which acts as a form of DRX, can be generated under compressive stress with mass transport through long-range diffusion. The sequence of steps for whisker growth under the proposed DRX model is illustrated in Figure 1.7. Figure 1.7 (a) shows that the compressive stress caused by deformation creates dislocations that pile up at pre-existing GBs. The resulting strain energy increases until to the point where new grains are initiated as the DRX grain refinement step. Then the new grains grow into the regions of accumulated defects by boundary migration, which is illustrated by the progression shown in Figure 1.7 (b) to (c). As shown in Figure 1.7 (d), whisker growth occurs by the movement of atoms across the DRX GB with mass transport once the grain size of the recrystallized grain is similar to that of the neighboring in-plane grains.

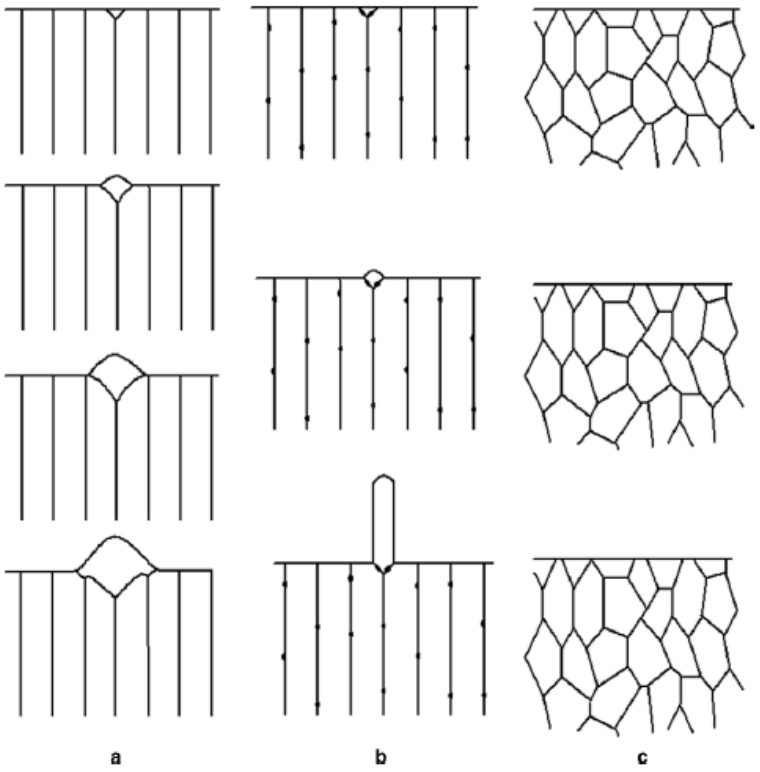


Figure 1.5. Schematics show the surface morphology of different alloys. (a) Sn; (b) Sn-Cu; (c) Sn-Pb. From Acta Materialia, vol. 53, Boettinger et al, "Whisker and Hillock formation on Sn, Sn-Cu and Sn-Pb electrodeposits", pp. 5033-5050, copyright 2005, with permission from Elsevier. [21]

Sarobol et. al [34] modeled the shallow surface grain as a stepped-cone shape composed of cylindrical disks. A simplified 2-D cross-section of a surface defect growing straightly normal to film surface is schematically shown in Figure 1.8. GBs are faceted into two components, namely accretion plane and sliding plane. Localized Coble creep leads to the atomic flux to surface grain, and this flux causes shear at the GBs by stress accumulation. For this proposed growth model of whiskers, two coupled processes control whisker growth: atom accretion along GBs on planes normal to the growth direction of whiskers resisted by GB sliding friction parallel to the growth direction. Once the friction is overcome, whisker growth occurs by stress relaxation. Since the critical stress is dependent on GB area, it is highly sensitive to the grain geometry. It is concluded that the growth rate is a function of GB sliding coefficient, film stress as well as the angle between whisker normal and the oblique GBs, and the angle is determined by the surface grain geometry and grain size of the whisker grain.

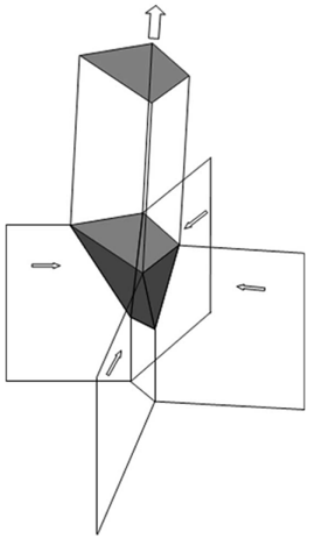

Figure 1.6. A schematic shows the mechanism for whisker growth due to Sn atom accretion from different directions as the stress relaxation mechanism. From Acta Materialia, vol. 53, Boettinger et al, "Whisker and Hillock formation on Sn, Sn-Cu and Sn-Pb electrodeposits", pp. 5033-5050, copyright 2005, with permission from Elsevier. [21]

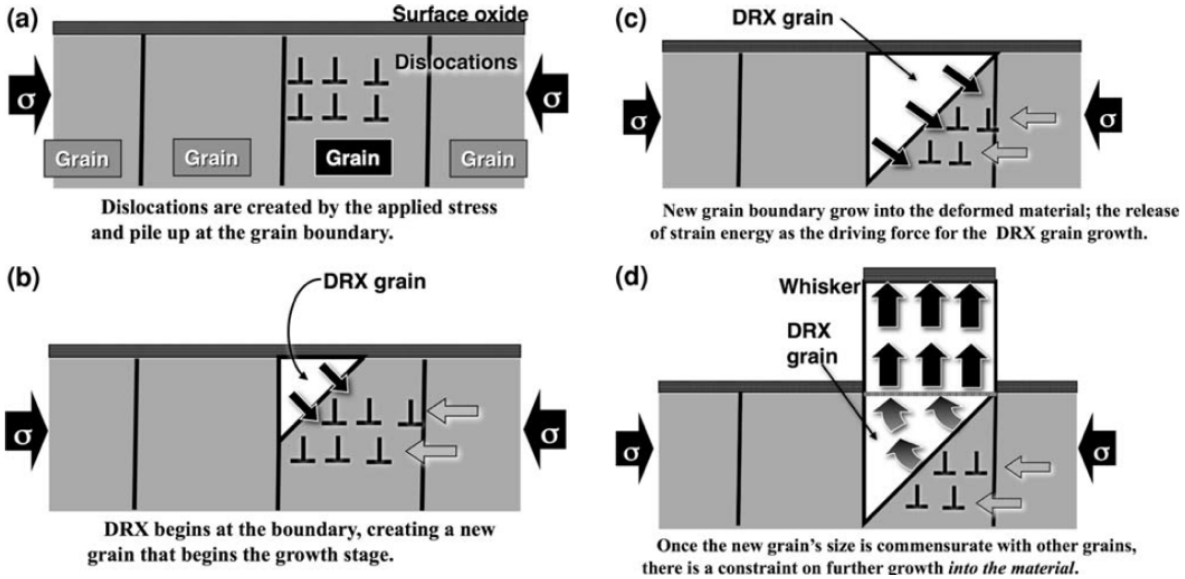


Figure 1.7. A series of schematics shows whisker formation by Dynamic Recrystallization (DRX). (a) Applied stress creates dislocations that pile up at GBs. (b) Nucleation of the recrystallized grain by DRX at GBs with stress accumulation by continuous applied stress. (c) The recrystallized grain continues to grow into the regions with high concentration of dislocations. (d) Whisker growth from the surface occurs once the grain size is similar to that of in-plane grains. From Journal of Electronic Materials, vol. 38, no. 9, Vianco et al, "Dynamic Recrystallization (DRX) as the Mechanism for Sn Whisker Development. Part I: A Model," pp. 1815-1825, copyright 2009, with permission from Springer. [4]

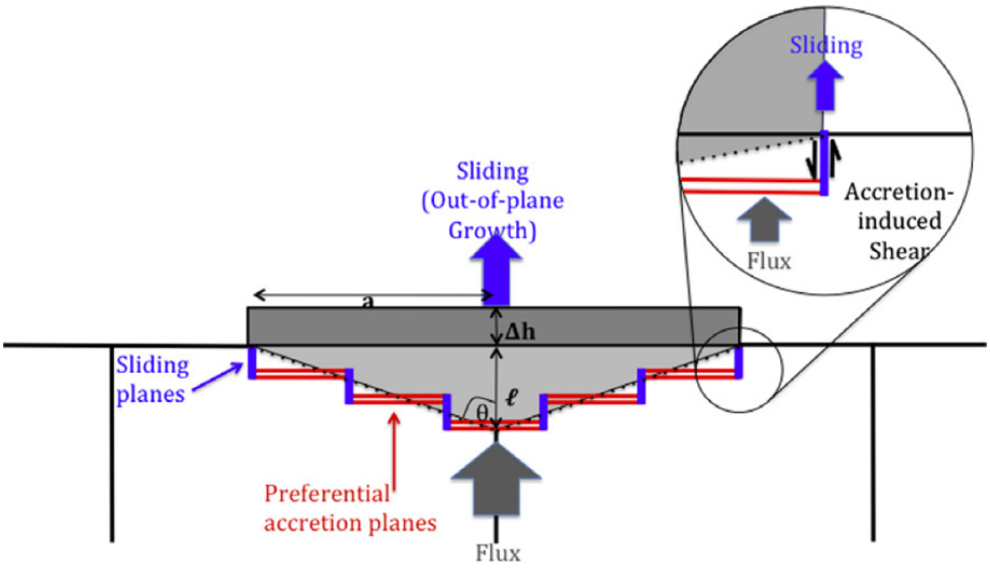


Figure 1.8. A schematic model shows whisker formation considering atomic accretion and GB sliding (GBS) from a shallow surface grain. From JOM, vol. 65, no. 10, Sarabol et al, "A Predictive Model for Whisker Formation Based on Local Microstructure and Grain Boundary Properties," pp. 1350-1361, copyright 2013, with permission from Springer Nature. [34]

Wang's model [35] focused on evolution of Sn whiskers and subsiding grains in thermal cycling. Figure 1.9 is a schematic of the whisker "pinch-off" phenomenon due to thermal cycling process. The red arrows show the directions of the stress. As illustrated in Figure 1.9 (a), whisker grows due to compressive stress upon heating. The oxidation of newly exposed Sn surfaces also occurs during this stage, as Sn oxidizes rapidly once exposed to air. Then cracks form along whisker GBs due to the tensile stress generated during the cooling phase of thermal cycling (Figure 1.9 (b)). The oxidation of the freshly exposed Sn surfaces prevents the cracks from closing. In the subsequent heating phase (Figure 1.9 (c)), under compressive stress, Sn atoms diffuse to the whisker grain via the intact GBs and the whisker grows with a smaller radius. Figure 1.9 (d) and (e) show that the tensile stress during subsequent cooling leads to further cracking along whisker GBs and the process repeats. This leads to continuous formation and oxidization of GB grooves and more fragile whiskers due to the decreasing diameter of the whisker. When the whisker radius is small enough, it pinches and breaks off, as shown clearly in Figure 1.9 (f). Sn whiskers experience compressive and tensile stress during the thermal cycling process, which are the same kinds of stress that also exist in the cyclic bending experiment of the present research. Though the present research eliminates the effect of CTE, this model can still serve as a guideline for understanding the mechanism for response of tin films during cyclic bending.

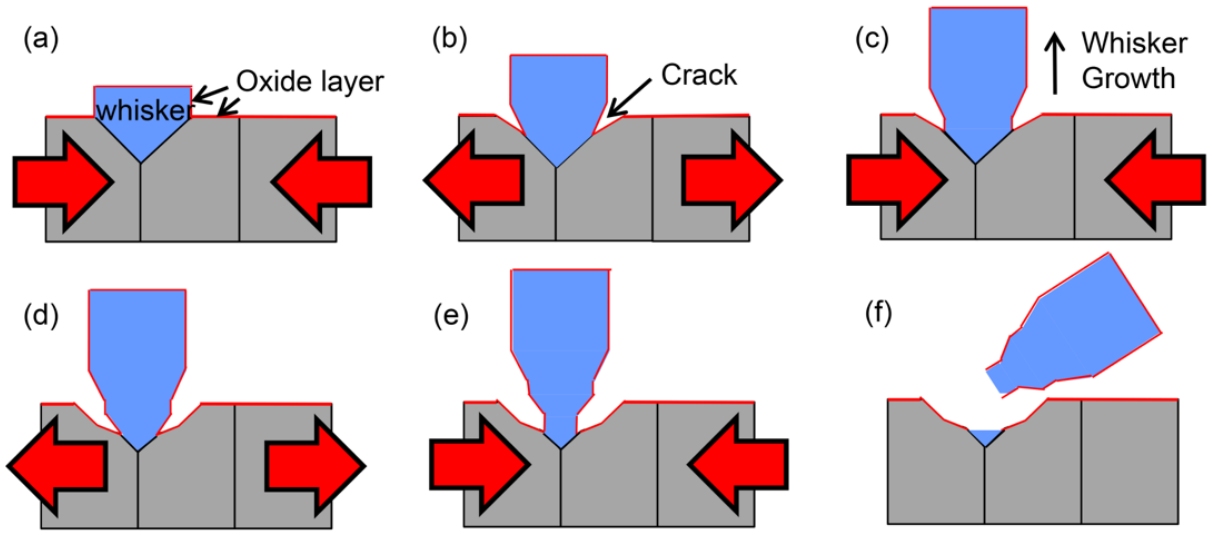


Figure 1.9. A series of schematics show whisker "pinch-off" phenomenon during thermal cycling. (a) whisker formation due to compressive stress upon heating; (b) crack formation at whisker root due to tensile stress upon cooling; (c) whisker growth with a decreased radius; (d) crack propagation along GBs; (e) continuous whisker growth with a further smaller radius; (f) final whisker "pinch-off". From Journal of Materials Science, vol. 65, Wang et al, "Evolution of tin whiskers and subsiding grains in thermal cycling," pp. 1099-1113, copyright 2014, with permission from Springer Nature. [35]

## 1.4 **Deformation Mechanisms of Tin Films**

The deformation behavior of thin films subjected to different forms of loading must be taken into consideration prior to material design. In the actual deformation process of tin films, not all of 32 slip systems activate due to the misorientation between grains and stress axis as mentioned above. The grain size and morphology of tin films influence deformation behavior. For instance, larger grains hinder the slip process [36], thus whisker formation that is related to slip creep mechanism becomes more difficult for large grain samples. Since the recrystallization temperature of Sn is below RT [37], strain hardening is not observed when Sn is deformed at RT and above. The most representative theories to explain the behavior of tin films due to mechanical forces are creep-based model, threshold stress model and growth model [37]. The interrelation and interaction of these three models provides the theoretical basis to explain evolution of tin films.

The creep-based model is due to the fact that tin films deform in orthogonal directions when applying mechanical forces to its surface and creep occurs in tin films at RT to relax stress. Since the actual tin film is usually very thin in the semiconductor industry, low stress and small "raised"

volume are expected during the creep process inducing a multiaxial stress concentration outside the pressured area. Although stress relaxation occurs, multiaxial stress components remain as residual stresses. The residual stress can interact with GBs of tin films and facilitate mass diffusion and whisker formation [38].

To initialize the growth of surface defects, the stress induced by applied mechanical forces must be greater than the surface energy of these defects. Thus, there exists a stress value called the threshold stress above which growth of surface defects is promoted. The total surface energy $\Delta U_s$ of a whisker that grows by $\Delta l$ with an assumed grain size of $2a$ is shown as below [39]:

$$\Delta U_s = \gamma_s \cdot \left(4\sqrt{2}a\right) \cdot \Delta l \qquad \text{Eq. 1-1}$$

Where $\gamma_s$ is the surface energy per unit area (J/m$^2$). Since the total surface energy $\Delta U_s$ is proportional to grain size $2a$, whiskers are more prone to pop-up from tin films with smaller grain size, in consistent to the previous results [36]. Once the stress induced by mechanical forces exceeds the surface energy of defects, Sn whiskers begin to grow at a growth rate that has a linear relationship with the applied force [7], which lays the foundation for growth model.

## 1.5 Cyclic Bending of Thin Films

### 1.5.1 The Benefits of Cyclic Bending Experiment

While there is significant research on tin films during thermal aging and thermal cycling [23,35,40,41], devices are also subject to vibration, making it reasonable to also examine stress relaxation under these conditions. The cyclic bending experiment is a high-throughput technique that samples a range of strain conditions in just a single experiment set-up. For the most simplified first mode vibration, the strain amplitude varies linearly from maximum at the fixed end to zero at the free end of the cantilever, as shown clearly in Figure 1.10 (a). Several types of damage can be co-existing and distributed along the cantilever during the cyclic bending experiment. The dominant damage response and the ratio between different defect types is the results from coupling of different stress relaxation mechanisms. Figure 1.10 (b) illustrates that the damage area also extends from the fixed end of the cantilever with additional number of cycles due to the increasing fatigue damage accumulation.

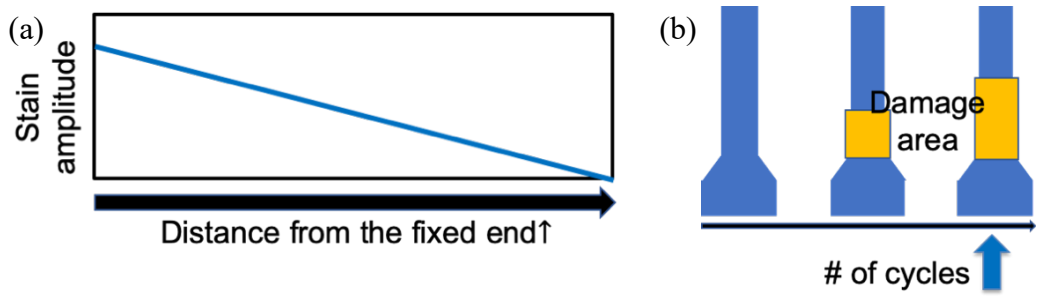


Figure 1.10. Schematics show (a) strain amplitude distribution along the cantilever during cyclic bending; (b) extension of damage area with increasing number of cycles for the first mode vibration

### 1.5.2 **Cyclic Bending of Other Materials Systems**

There are several researches focused on the cyclic bending of films with other materials systems, such as Cu and Al. The focus of these research includes the types and quantitative analysis of damage in film surface developed during cyclic bending, the fatigue life of the film and the corresponding influence of strain amplitude, strain gradient, material, number of cycles, film thickness as well as interface properties and initial microstructure on the defects and fatigue life. Several mechanisms have been thrown out to explain the results, considering creep, dislocation glide and accumulation, GB and interface influence.

Trinks and Volkert [42] investigated five different damage types for cyclic bending of Cu films on silicon nitride Atomic Force Microscopy (AFM) cantilevers with frequencies of 120-140 kHz. The damage types include extrusions, short cracks, twin growth, grooves, GB hillocks and twin boundary (TB) extrusions, and the partitioning among different types of defects varied with film thickness. For a particular kind of defects as response to fatigue damage accumulation, its density increases with increasing strain amplitude approaching the fixed end of the cantilever at designated number of cycles (Figure 1.11 (a)) and with more number of cycles at fixed strain amplitude (Figure 1.11 (b)). Those are also very important parameters in the present research. Two mechanisms are coupling and competing with each other during the cyclic bending, i.e. “creep” and “dislocation glide” model. “Creep” model shows that surface defect formation initializes when the multiple of the plastic strain accumulation per cycle and number of cycles N exceeds some critical plastic strain, thus the threshold strain amplitude deceases with increasing N. “Dislocation glide” model requires the strain amplitude per cycle overwhelms the critical strain to achieve damage accumulation since the strain below the critical strain is reversable. This causes a constant

strain amplitude whatever the number of cycles is. The different response of strain amplitude to number of cycles can help predict the mechanism for surface defect formation.

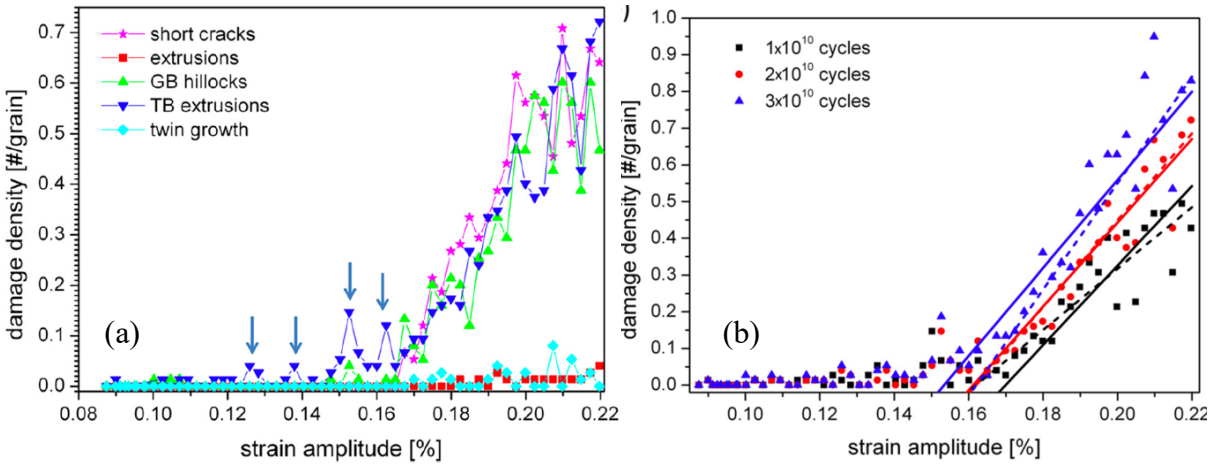


Figure 1.11. Plot of damage distribution along the cantilever for Cu films on silicon nitride AFM cantilevers with a film thickness of 150 nm (a) all kinds of damage at $2\times10^{10}$ cycles; (b) twin boundary (TB) extrusions with different number of cycles. From Journal of Applied Physics, vol. 114, no. 9, C. Trinks, C.A. Volkert, "Transition from dislocation glide to creep controlled damage in fatigued thin Cu films," pp. 093510, copyright 2013, with permission from AIP Publishing. [42]

Schwaiger et al. [43] focused on the influence of film thickness for lifetime of Cu films on polyimide substrate. Three film thickness is selected, 0.4 $\mu$m, 0.8 $\mu$m and 3.0 $\mu$m. All the films exhibit similar stress-strain relationship with much higher maximum stress of 420 MPa for 0.4 $\mu$m films while 0.8 $\mu$m and 3.0 $\mu$m films have similar maximum stress of about 300 MPa. The damage types are cracks, extrusions and voids. The propagation of cracks is usually along GBs while the extrusions are intragranular. Voids usually show up at the interface between the film and the substrate just below the extrusions and extend towards the surface. To explain the void formation, a simplistic schematic of a columnar structure is assumed. Edge dislocation annihilation creates voids at the interface and the voids can diffuse quickly to the surface and GBs upon formation, as shown in Figure 1.12. However, for some particular grain orientation <111>, due to pure screw dislocations at the interface, vacancies cannot be created by dislocation annihilation. This leads to the lack of voids at the interface for <111>-oriented grains.

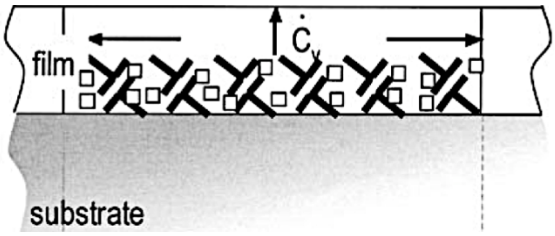


Figure 1.12. A schematic shows vacancy formation at the interface between Cu films and polyimide substrate during cyclic bending. From Philosophical Magazine, vol. 83, no. 6, Schwaiger et al, "Cyclic deformation of polycrystalline Cu films," pp. 693-710, copyright 2003, with permission from Taylor & Francis. [43]

Burger [44] investigated the evolution of Cu and Al films on Si substrate for cyclic bending of large cantilevers in mm range. The influence of strain amplitude and heat treatment as well as Ti interlayer between the film and the substrate for a specific number of cycles has been analyzed in detail. Heat-treatment and Ti interlayer leads to the grain size difference in the film regardless of the film components. For both Cu and Al films, the amount of fatigue damage increases with increasing strain amplitude from the free end to the fixed end of the cantilever. The damage at the surface is observed to be a mixture of grain growth, hillocks, extrusions, pores and crack formation. The dominated damage type and distribution varies with the materials of the film and the initial state of the film due to heat treatment and the interface. The extrusions at the film surface and the pores throughout the film and at the interface between the substrate and film can be seen clearly in the cross-section images. Table 1.2 summarizes the relationship between responses and the proposed deformation mechanisms in Cu and Al films, which verifies the role of different processes. These processes can also exist simultaneously for tin films and the coupling and competing between these processes during cyclic bending determines the response of stress relaxation. Both cyclic bending of Cu and Al are done at RT with a face-centered-cubic (FCC) structure. The BCT structure of Sn makes the situation more complicated as mentioned earlier.

Eberl et al. [45] observed three categories of extrusions, namely high-aspect ratio extrusions (HA), grain-like extrusions (GL) and half-height extrusions (HH) for cyclic bending of Al films on piezoelectric substrate at an ultra-high frequency of 915 MHz. Voids formed due to tensile stress were located near extrusions similar to what has been observed in Schwaiger's research while the extrusions due to compressive stress were intergranular. Grain rotation and shifts were also observed through scanning electron microscope (SEM) images. Kraft et al. [46] found large voids at the film-substrate interface under the extrusions for large grains, whereas cracks propagate

through fine grains. Thinner films are more resist to fatigues, which is also in consistent with Schwaiger's observations.

Table 1.2. Summary of correlation between damage types and possible mechanisms for Cu and Al films on Si substrate for cyclic bending experiment. From KIT PhD thesis, S. Burger, "High Cycle Fatigue of Al and Cu Thin Films by a Novel High-Throughput Method," pp. 104, copyright 2012, with permission from KIT Scientific Publishing. [44]

| mechanism | grain growth | hillock formation | extrusion formation | pore formation | short cracks |
|---|---|---|---|---|---|
| Al 'as dep' | | | | | |
| Al 'an' | | | | | |
| Cu 'as dep' | | | | | |
| Cu 'an' | | | | | |
| Cu 'on Ti' | | | | | |

*diffusion mediated processes* *dislocation mediated processes*

*grain boundary influences* *surface/interface influences*

## 1.6 **Summary**

To sum up, Sn has several anisotropic thermal and elastic properties due to the BCT structure, and this leads to the influence of preferred grain orientation on evolution of tin films. The plastic deformation for each grain may vary significantly due to the highly elastic anisotropy, and it contributes to different stress relaxation mechanisms. The multiple sources of compressive stress generated during film deposition process, room aging and cyclic bending experiment contributes to the complexity of analyzing stress relaxation of tin films for the high-throughput cyclic bending experiment.

Several work has been done to show the evolution of surface defects during room aging, oxidation environment, or thermal cycling. Some of the previous work just focused on the grain orientation and morphology change under specific conditions without quantitative analysis. Some work is done more systematically, revealing the relationship between time, number of thermal cycles, film thickness and composition with whisker density, IMC volume/area and stress in tin films. It helps explain the mechanism for surface defect formation more clearly. For the present research focused on cyclic bending of tin films, the influence of strain amplitude, strain rate, resonant frequency, number of cycles and temperature can be figured out with quantitative analysis of surface defect density/volume varying with those parameters.

Much work needs to be done to correlate the mechanical forces to different critical factors that influence the formation of surface defects by careful experiment design and build-up of models. There are multiple factors that may influence the formation of surface defects, and there should be only one parameter for each set of experiment. The prospective model should distinguish the critical mechanism that leads to different stress relaxation responses based on dislocation movement, diffusion and mass transport. The model should also refer to previous established models, and reveals the difference between room aging, thermal cycling and mechanical cyclic bending. This helps distinguish the contribution of elastic stress, plastic stress as well as thermoelastic stress to surface defect formation. Performing cyclic bending experiments with tin at its high homologous temperature provides an opportunity to study the partitioning of surface defect formation as well as the similarities and differences from whiskers growth observed with IMC formation and thermal cycling. The ultimate goal is to help make significant progress in interpreting the mechanisms of surface defects to film stress relaxation and to promote further design evolution in semiconductor industry.

# 2. CYCLIC BENDING OF AFM CANTILEVERS

## 2.1 **Motivation**

Several research has been focused on tin films in room aging and thermal cycling environment. There are two aspects contributing to this research hot spot, one is due to the actual application and storage of electronic devices, the other is due to the convenient experiment set-up and a few simplified mechanisms that need to be taken into consideration when building up the model. For reproducible films with similar thickness prepared by the same electroplating solutions, the stress generated by IMC formation should always be the same under all conditions. For thermal cycling experiment, the additional source of stress from CTE mismatch makes the system a little more complicated. The CTE-oriented stress is influenced by how the thermal cycling is operated. It depends on the temperature range for the cyclic experiment, the hold time at extreme temperature, the heating and cooling rate, etc. For mechanical cycling experiment at RT, the parameters include strain amplitude/rate, number of cycles, as well as resonant frequency even though the effect of thermal stress is excluded. It is hypothesized that all the parameters mentioned above in mechanical cycling experiment will influence the type and density of surface defects. The difference between thermal cycling and mechanical cycling helps distinguish the influence of thermal and mechanical stress, separately. For room aging and thermal cycling experiment, only one condition can be achieved in one experiment set-up, for example one storage condition or one CTE mismatch profile. The multiple stress conditions that can be achieved in just one experiment set-up makes cyclic bending an outstanding high-throughput technique. The intention to separate thermal and mechanical effect as well as the effort to increase research efficiency lays the foundation for cyclic bending experiment.

AFM apparatus is a powerful tool to measure the mechanical properties and get the topography shape of the sample. It can be achieved by controlling the force between the AFM cantilever tip and the sample through different imaging modes. The AFM cantilever is vibrated at resonant frequency with the piezo element installed in the holder. To achieve the idea of cyclic bending on small scale samples, tin films are prepared on standard AFM cantilevers and then the cantilever can be vibrated using AFM testing platform. The focus is the AFM probe instead of the sample, and the maximum strain and cyclic numbers can be controlled by driving voltage and time,

respectively. The common resonant frequency of AFM cantilevers in tens of kilohertz range due to the small dimensions also makes it possible to achieve as many as hundreds of millions of cycles in just a few minutes. Thus, the effect of stress accumulation with an increasing number of cycles can be studied efficiently and effectively.

The idea for this work was borrowed from the systematic analysis of damage evolution and distribution for Cu films on silicon nitride AFM cantilevers by Trinks and Volkert [42]. In the research presented here, two kinds of films prepared by different methods have been investigated, namely physical vapor deposition (PVD) films and electroplated films. The influence of strain distribution along the cantilever and cyclic numbers is analyzed in detail. The role of different film thickness to substrate ratio and IMC formation have been revealed by comparing between the response of PVD and electroplated films during cyclic bending with other factors constant. This helps understand mechanisms and provides guidelines for controlling fatigue stress accumulation in tin films utilized at ultra-high frequencies.

## 2.2 **Procedures**

Standard Si AFM cantilevers (450 $\mu$m * 50 $\mu$m * 2 $\mu$m; spring constant=0.2 N/m) were used as substrates for these ultra-high frequency cyclic bending experiments. The resonant frequency of the as-prepared cantilevers is about 13 kHz. The films were prepared by two methods. One is directly prepared on Si substrate by PVD, the other is prepared by commercial electroplating method with PVD Ti & Cu layers as interfaces.

For PVD films, a 1 $\mu$m Sn layer was directly deposited on the as-received Si AFM cantilevers by e-beam deposition. For electroplated films, since tin films cannot be directly prepared on Si substrate due to the conductive issues, a 300 nm Cu layer was deposited to facilitate the electroplating process. To effectively limit the diffusion of Cu into Si causing deep-level defects, a 10 nm Ti layer was deposited firstly on Si substrate acting as an adhesion layer to connect between Si and Cu. Both Ti and Cu layer were deposited by rf magnetron sputtering.

The electroplating process was done with commercial electrolyte (Dow Solderon SC) at a current density of 10 mA/cm$^2$.A pure Sn foil was used as the anode and the AFM cantilever was the cathode. Nitrogen was bubbled through the electroplating solution to remove dissolved oxygen just before the electroplating process. In order to guarantee uniform film thickness, a magnet stirrer

was used to assist the process. The final film thickness of ~12 $\mu$m was much thicker than that of PVD films. The schematic of the fabrication process is shown in Figure 2.1.

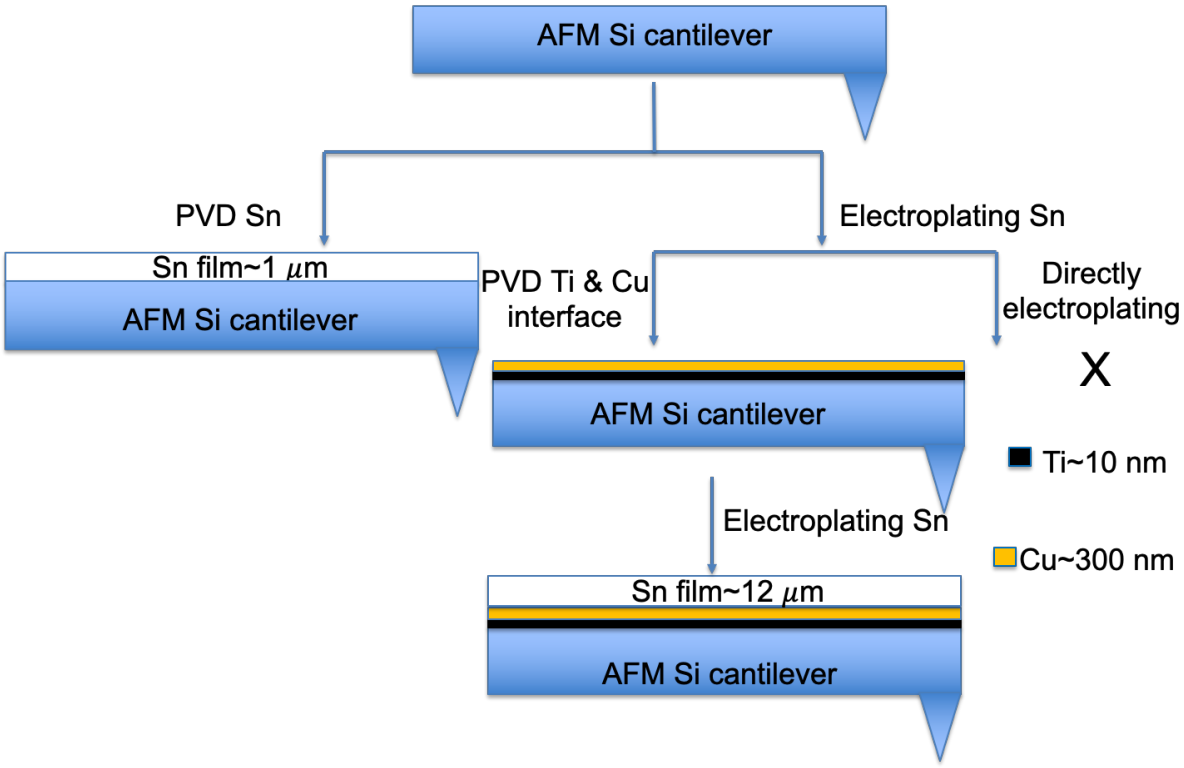


Figure 2.1. A schematic shows fabrication of AFM samples for cyclic bending experiment

The measurement for the resonant frequency of the AFM cantilevers was done by sweeping a designated range of frequencies. Then the oscillation of AFM cantilevers at the resonant frequency was done using the piezoelectric drive of an AFM (multimode AFM, Veeco) by controlling the input to the z-piezo actuator. The fundamental mode vibration guarantees the equivalence of strain amplitude and surface strain of the cantilevers.

The surface defect density and morphological evolution of the samples were measured as a function of the designated number of cycles and position (corresponding to strain amplitude distribution) along the cantilevers using SEM (Nova NanoSEM, FEI). The cantilever was re-mounted in the AFM apparatus repeatedly several times with inspections starting at a few million cycles and continued with small to large intervals to millions of cycles. To characterize surface defect formation as a function of position along the cantilever, the cantilever was divided equally into 11 areas and the number of surface defects in each area was counted as a function of the

cumulative number of cycles. Selected cross-section areas of the samples to reveal the surface grain geometry and grain size were obtained by focused ion beam (FIB) milling and imaging (Quanta 3d, FEI).

The main differences between these two methods are that there is IMC formation for samples with underneath wetting Cu layer and the obvious thickness difference. This may influence the stress relaxation response for the cyclic bending experiment.

## 2.3 Results and Discussion

### 2.3.1 Evolution of PVD Tin Films Morphologies

The surface morphology and structure of the PVD tin films are shown in Figure 2.2. As shown in Figure 2.2 (a), the film with a in-plane grain size of 1 $\mu$m is very flat without obvious roughness due to the PVD preparation method. The cross-section image exhibited in Figure 2.2 (b) shows columnar structure with thickness of 1 $\mu$m. The overall cantilever has large length to width ration of 9:1 with very sharp free end (Figure 2.2 (c)). The AFM tip can be seen clearly in the enlarged SEM image (Figure 2.2 (d)).

As described in section 2.2, the PVD tin films were deposited directly on Si AFM cantilevers without a Cu wetting interlayer. This leads to the lack of IMCs at the interface propagating into films, which is a source of compressive stress for tin films on Cu substrate. Thus, the response of the films to bending stresses are determined here without the confounding effect of IMC formation.

There are two dominated kinds of surface defects to be observed on tin films after cyclic bending process, one is the pre-existing surface defects from the PVD process, the other is the newly formed surface defects from cyclic bending process. Figure 2.3 and Figure 2.4 shows the evolution of the pre-existing and new surface defects, respectively. All surface defects grew from pre-existing in-plane grains, as determined by tracking surface grain shapes as a function of the number of cycles.

The pre-existing surface defects remained its original shape during the cyclic bending with cyclic process up to 22M cycles, as shown from Figure 2.3 (a) to (c). The additional number of cycles tracking until 1640M cycles verifies that the pre-existing surface defects caused by plating stress seem to be almost unaffected by the cyclic bending process with several interruptions for imaging.

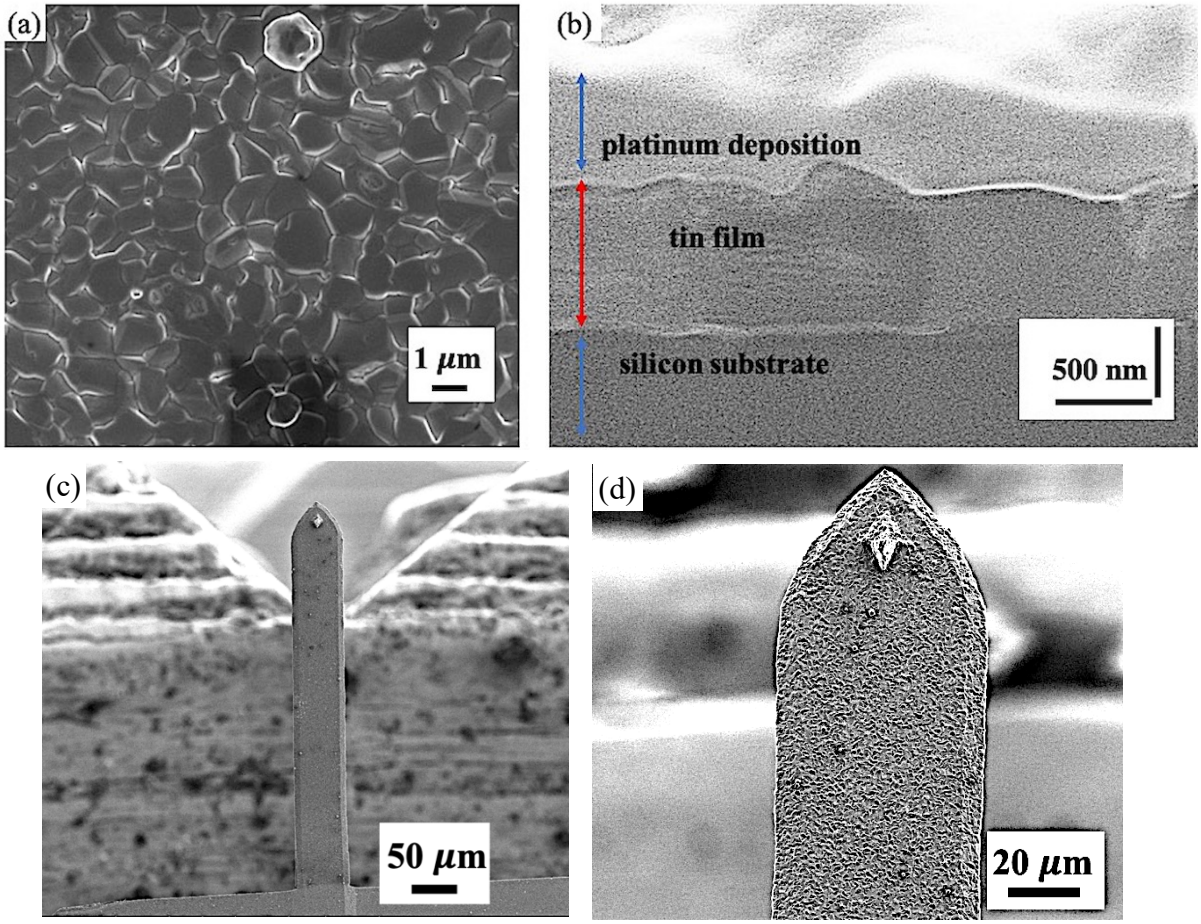


Figure 2.2. SEM images of the as-prepared PVD tin films. (a) surface morphology with uniform grain size of 1 $\mu$m; (b) cross-section image by FIB cut shows columnar structure of films; (c) the overall shape of the AFM cantilever; (d) the enlarged image of the cantilever sharp tip

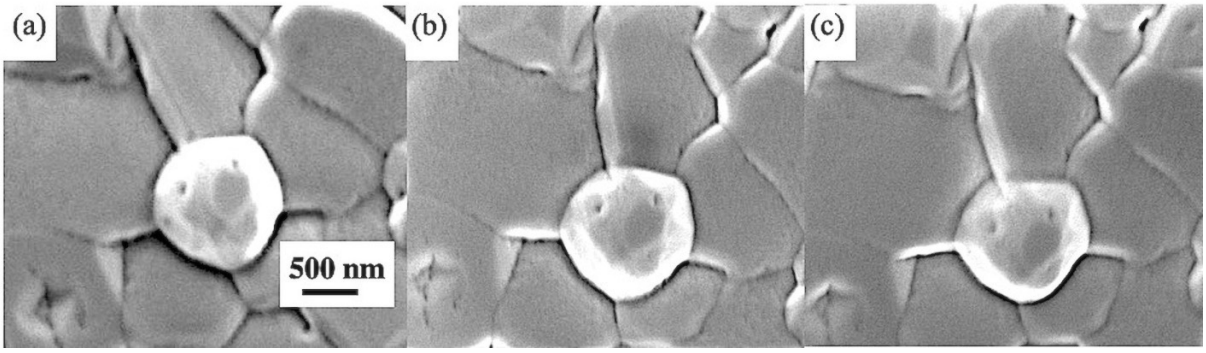


Figure 2.3. SEM images show the evolution of pre-existing surface defects during cyclic bending. (a) as-prepared; (b) after 4.3M cycles; (c) after 22M cycles. Very little changes were observed for pre-existing defects.

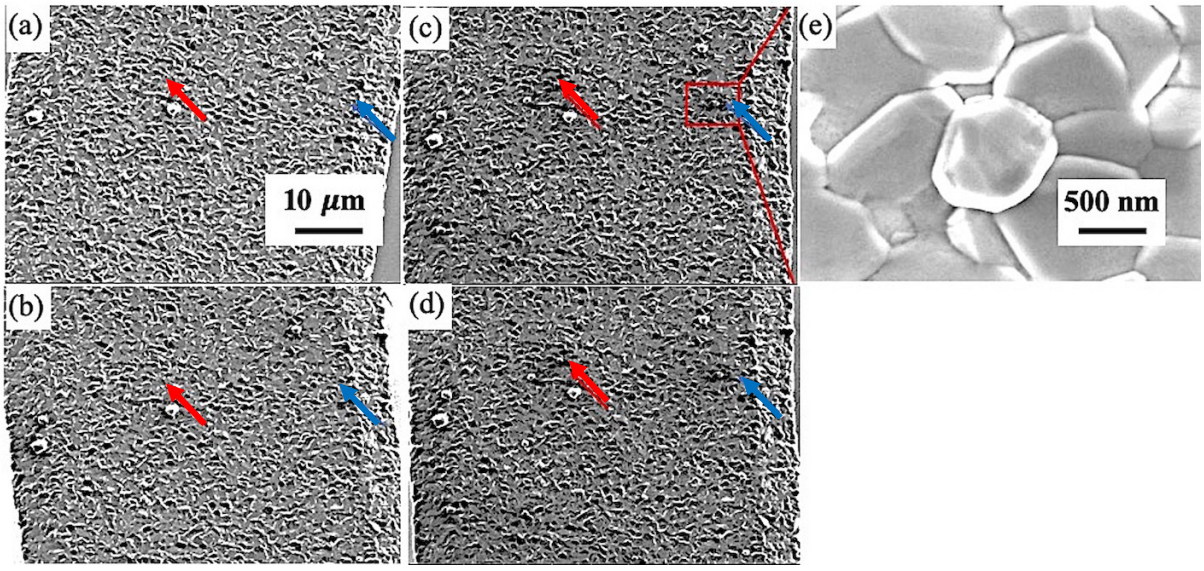


Figure 2.4. SEM images show surface defects formation during cyclic bending. (a) as-prepared; (b) after 4.3M cycles; (c) after 22M cycles; (d) after 86M cycles; (e) the enlarged image of one of the newly formed surface defects marked in the rectangular area in fig. (c)

Only two new defects formed between 4.3M cycles (Figure 2.4 (b)) and 22M cycles (Figure 2.4 (c)), as their position indicated by the red and blue arrows in Figure 2.4 (a) to (d), respectively. The new surface defects have similar morphology as pre-existing surface defects, as seen by comparing Figure 2.3 with Figure 2.4 (e). Once the surface defects formed, they did not grow out-of-plane after vibrating for additional cycles, which can be seen clearly from Figure 2.4 (c) and (d). This is the same situation as for pre-existing surface defects, as shown in Figure 2.3.

Figure 2.5 shows the typical cross-section image of the surface defect formed on PVD tin films. As similar to the widely accepted grain geometry for electroplated film [12,21,35], some surface grains are shallow grains with oblique GBs beneath it (Figure 2.5 (b) and (d)). Figure 2.5 (d) shows that the intersection of the GBs beneath the defect almost reaches the substrate. For other surface defects, the GBs just pass through vertically from the film surface to the interface, showing similar geometry as the neighboring grains (Figure 2.5 (e)). The height of the defect is similar to the film thickness or at most twice of the film thickness, which indicates the similar morphology and size of defect grains compared to the surface grains on tin films.

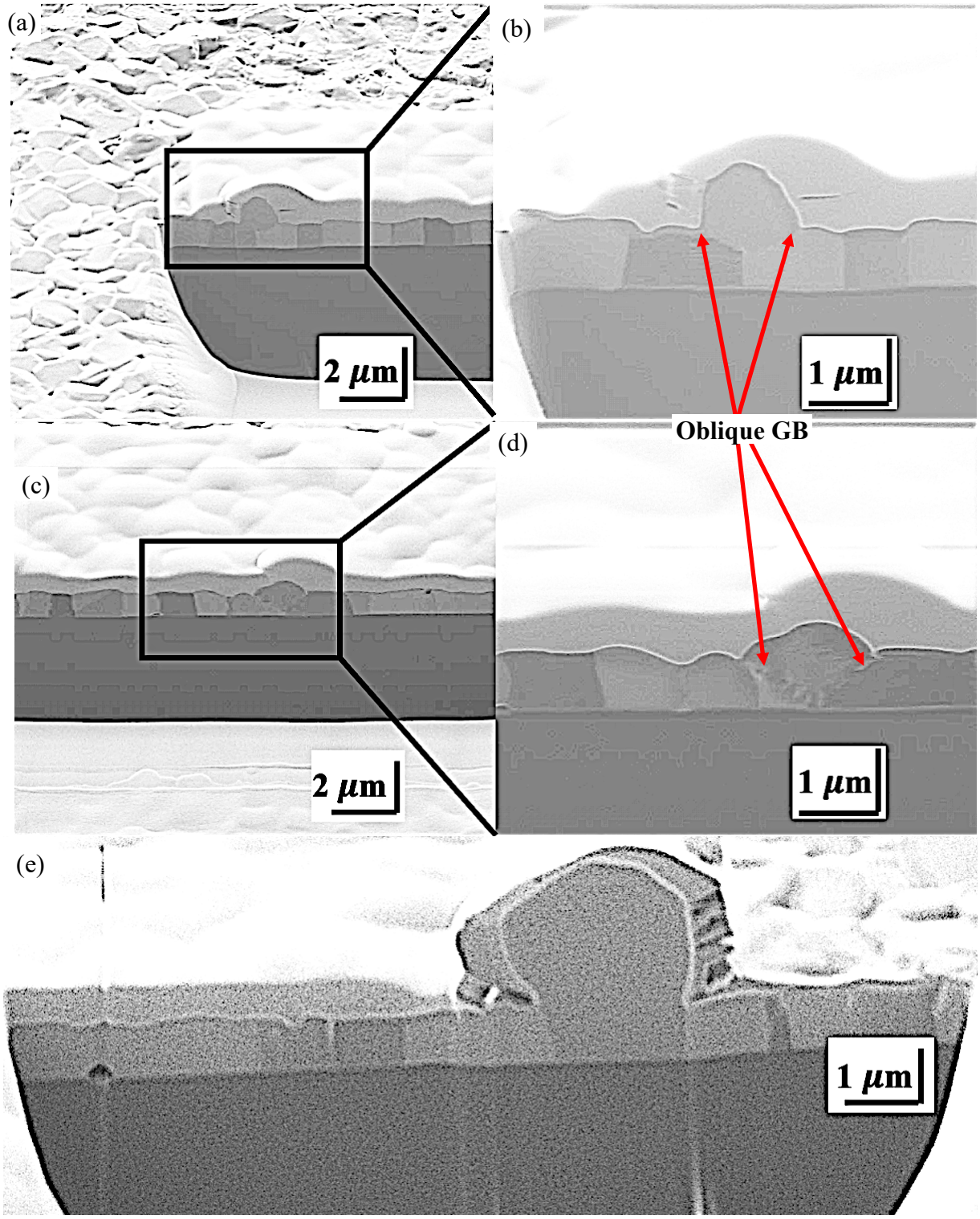


Figure 2.5. (a), (c), (e) the different GB geometry of the surface defects on PVD tin films; (b), (d) the enlarged images of the area in fig. (a) and (c), respectively. The oblique GBs beneath the shallow grains (a), (c) and straight GBs from film surface to the interface (e) can be seen clearly.

Since surface defect formation is only one form of stress relaxation and there are multiple stress relaxation mechanisms, the cumulative volume of all the new surface defects indicated the extent of stress relaxation by defect formation. Due to the uniform grain size of tin films prepared by PVD process (Figure 2.2 (b)), the volume for each individual grain only depends on the defect height. The total extent of stress relaxation is a coupling function of defect height and density. If the strain amplitude is the only driving force for whisker growth, the volume of the defects would then depend on the strain amplitude distribution along the cantilever.

To get the exact height for each defect above the film surface, defects were projected at two angles (0° and 45°). The images shown in Figure 2.6 were taken at 45° in (a), (b) and 0° in (c), (d) to get the projected height for the same defect. Figure 2.7 shows the height of the surface defects from the free end to the fixed end of the cantilever. The numbers on the x axis are the corresponding analysis sections from 1 approaching the free end to 11 near the fixed end. All the surface defects show a nearly constant height of 1.2 $\mu$m, and it indicates that the contribution of stress relaxation by each individual grain is almost the same along the cantilever with the smaller defect height to diameter ratio of about 1.2. The surface defects were short compared to those formed in other situations such as room aging and thermal cycling [8,34,35,40].

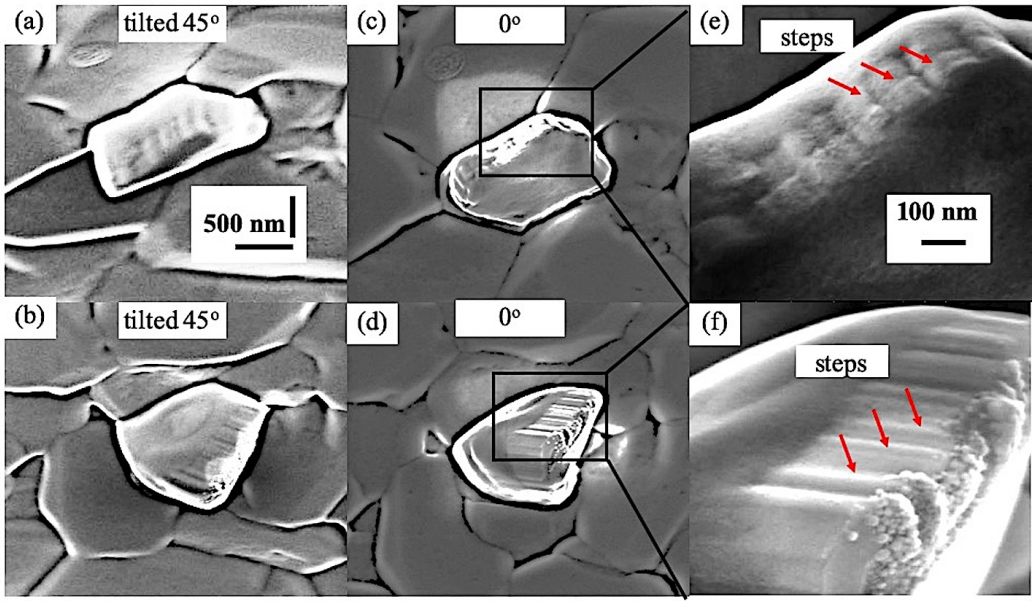


Figure 2.6. SEM images show the typical morphology of new surface defects after 730M cycles. (a), (b) SEM images of surface defects projected at 45° degree; (c), (d) the same surface defect in (a), (b) respectively at 0° degree; (e), (f) enlarged images of the squared areas in fig. (c), (d) respectively showing characterization of steps.

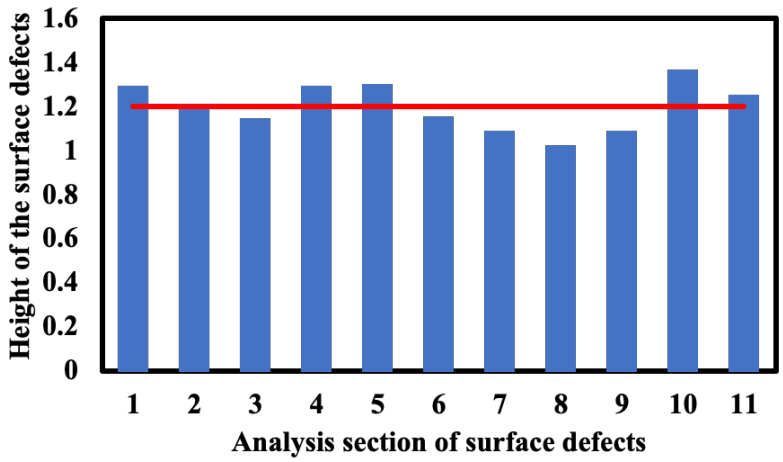


Figure 2.7. A plot shows height distribution of surface defects along PVD AFM cantilever. The red line indicates the average of the defect height.

The cumulative volume of all the surface defects can be expressed as

$$Cumulative\ volume\ of\ defect = number\ of\ defects * \pi(diameter/2)^2 * height$$

With constant height and area distribution along the cantilever, it can be concluded that the total volume of all the defects is only proportional to the defect density.

Striation steps can be seen clearly on one side of new surface defects formed after hundreds of million cycles (Figure 2.6 (e) and (f)). The steps indicate the evolution of defect morphology, namely the non-uniform defect growth out of the plane with changeable diameters. The striations found in this research are similar to the striations on whiskers formed during room aging [34], conventional thermal cycling from -40° C to 125° C (1 cycle/hour, 0.28 °C/s heating and cooling rate, 20 min hold time at extremes) [40], as well as rapid thermal cycling (RTC) where films are cycled in the temperature range of -45 °C to 85 °C (3 cycles/hour, 10 min hold time at extremes) [35]. The irregular stick-slip growth as well as GB sliding and migration contribute to the steps perpendicular to the growth direction of the defects [34,35,40]. The irregular-spaced striations are common on defects due to IMC formation during room aging. For thermal cycling, there exists repeated transition between compressive stress during heating half cycle and tensile stress during cooling half cycle, and whisker growth corresponds to the compressive half cycle. The number of cycles is always more than that of the striations indicates the "stick-slip" growth model. The striations and discontinued growth after the initial nucleation and growth for surface defects in the present research indicates a similar "stick-slip" behavior that will be discussed later. The rotation of surface defects (Figure 2.8) shows that some GBs remain in-plane while others grow out of the

film. It reflects the defects' changing diameter and non-constant growth out of the plane during cyclic bending. The asymmetrical growth for surface defects indicates different GB sliding and accretion rates based on the GB geometry.

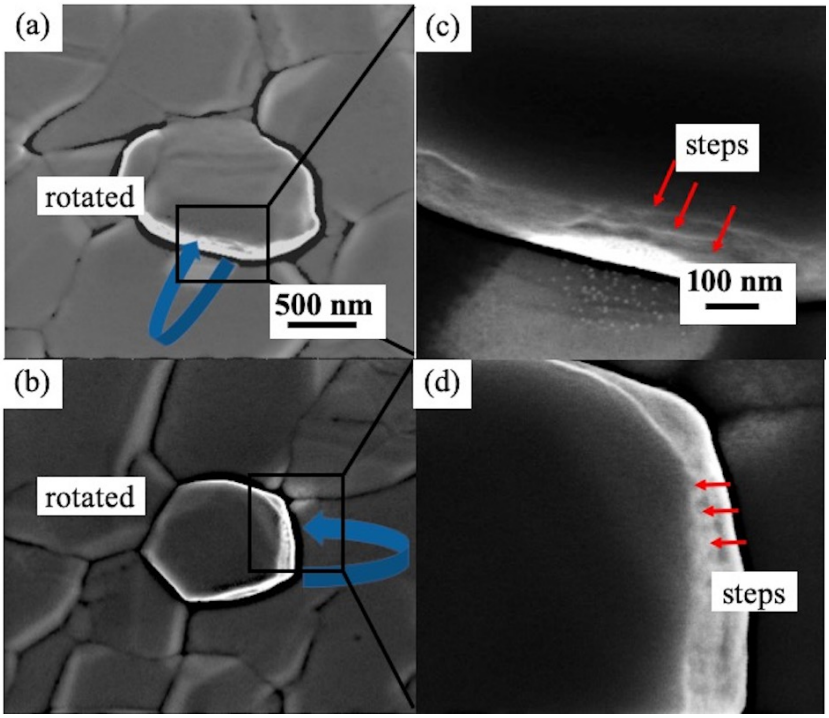


Figure 2.8. (a), (b) SEM images of new surface defects with irregular growth rate along GBs after 350M cycles; (c), (d) the enlarged area of the rotation part marked in fig. (a), (b), respectively.

In addition to the new short whiskers formed on film surface, there are also cracks formed as a stress relaxation mechanism occurring during this ultra-high frequency cyclic bending (Figure 2.9). Cracks can be seen along GBs, and they reflect the incompatible stress and strain accommodation between grains due to the significant difference between elastic modulus of Si and that of Sn. The elastic modulus of Si is in the range of 130-170 GPa [47], which is much larger than the average value of only a little over 40 GPa for Sn. Thus, the film needs to extend more with the same applied stress. Once the strain generated in the film cannot be relaxed quickly through other mechanisms, cracks propagate along the GBs as a response to the incompatible strain accommodation between grains. Cracks were also observed for cyclic bending of Cu films [42] as well as RTC of tin films on Si at significant strain [35]. The number of cracks is only 1 or 2 for each sample, and the few cracks distribute randomly and sparsely along the cantilever, thus the

quantitative analysis of cracks is ignored in the following part. It reflects the trade-off of different stress relaxation mechanisms, and defect formation overwhelms cracking in this research.

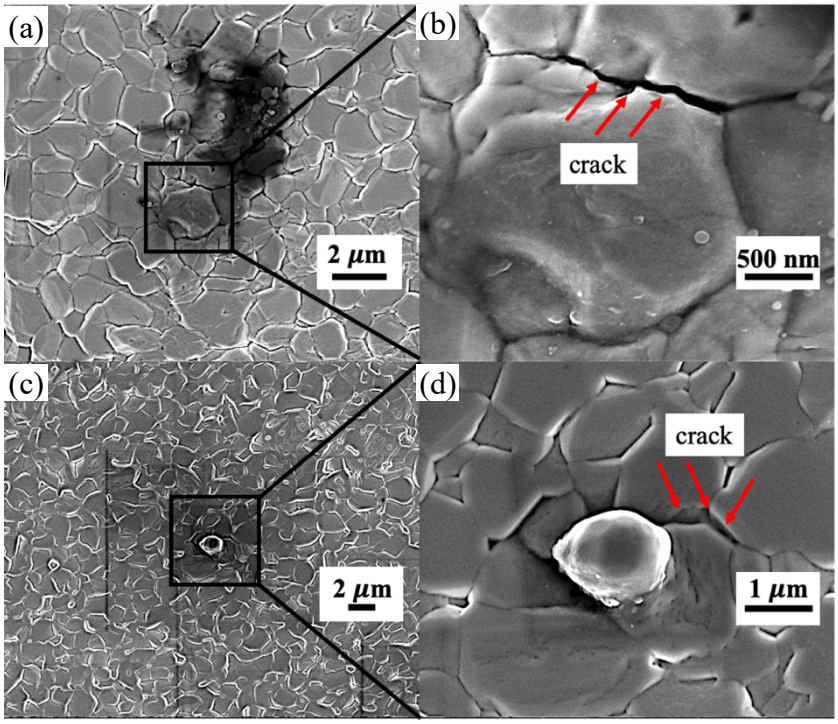


Figure 2.9. (a), (c) SEM images of cracks formed on tin films after 300M cycles for the first mode vibration; (b), (d) the enlarged SEM image of the area marked in fig. (a), (c) respectively

### 2.3.2 **Quantitative Analysis of PVD Tin Films**

For the cyclic bending experiment, the cantilevers were vibrated in two modes, namely first mode and second mode. The resonant frequency for the first mode was measured as 10.40 kHz while that for the second mode was 72 kHz. The case for the first mode is the most simplified, as mentioned earlier in section 1.5.1. The strain distribution along the cantilever is either all tensile or all compressive during cyclic bending with maximum strain always located at the fixed end. For the second mode, the strain is either tensile or compressive determined by the position of the cantilever during cyclic bending, increasing the complexation of stress distribution. The maximum strain amplitude with opposite sign can be achieved at two positions: one is at the fixed end as same as for the first mode vibration, the other is a local maximum strain at about 0.5 $L$ of the whole length from the fixed end [48]. For cyclic bending operated at different modes, the deflection $y_n$ (x) can be calculated through the following equation [49]:

$$y_n(x) = y_0\left[(cosk_nx - coshk_nx) - \frac{cosk_nL+coshk_nL}{sink_nL+sinhk_nL}(sink_nx - sinhk_nx)\right] \quad \text{Eq. 2-1}$$

Where $x$ is the distance from the fixed end, $y_0$ is the vibrational amplitude, $k_nL$ is the wave number of an infinite set of flexural vibration modes, and $L$ is the length of the cantilever. Based on cantilever vibration theory, $k_1L$=1.875 and $k_2L$=4.694. The curvature of the deflection distribution along the cantilever can be obtained by doing the second derivative of Eq. 2-1:

$$y_n''(x) = -k_n^2 y_0\left[(cosk_nx + coshk_nx) - \frac{cosk_nL+coshk_nL}{sink_nL+sinhk_nL}(sink_nx + sinhk_nx)\right] \quad \text{Eq. 2-2}$$

Since the strain on the surface along the cantilever has a linear relationship with the curvature of deflection, the form of strain distribution can be achieved even without the exact $y_0$ [48].

Figure 2.10 shows defect/area and defect/1,000 grains of 9 cantilevers with as-prepared films before cyclic bending. The original defect density per area varies within the range of 1800-3000/mm$^2$, and the large variations is due to the small dimensions of the cantilevers. The area of the film surface is only 0.0225 mm$^2$ (450 $\mu$m * 50 $\mu$m), and even one additional surface defect can change the defect density by 45/mm$^2$. As contrast to defect density per area, defect density per 1,000 grains does not change too much with the large quantitative cardinal number of 1,000 grains. The average original surface defect density is about 2200/mm$^2$ and 2.2/1,000 grains, indicated by the red line in Figure 2.10 (a) and (b), respectively. This is much higher than the defect density of 300/mm$^2$ for 1.45 $\mu$m electroplated film at room aging condition due to IMC formation [50]. This indicates that even though the PVD films eliminate the effect of IMC formation, the compressive stress generated through the PVD process is much larger than the combine stress originated from both plating process and IMC formation for electroplated films.

To investigate the influence of stress accumulation on defect formation, Figure 2.11 (a) shows the relationship between surface defect density/area and number of cycles for both the first and second mode vibration. One sample was followed for the first mode vibration, while two samples marked as “sample 1” and “sample 2” in blue and orange color were studied for the second mode vibration. Figure 2.11 (b) is used to show the defect evolution for the first mode more clearly. Inspections with several intervals to about 340M cycles was conducted for the first mode vibration. For the second mode vibration, one sample stopped at 1640M cycles and the other stopped at 1840M cycles. The overall tendency is increasing surface defect density with additional number of cycles. The plot shows S-shape behavior, and it can be roughly divided into three distinct stages marked as I, II, III, which is shown clearly in Figure 2.11 (a) and (b).

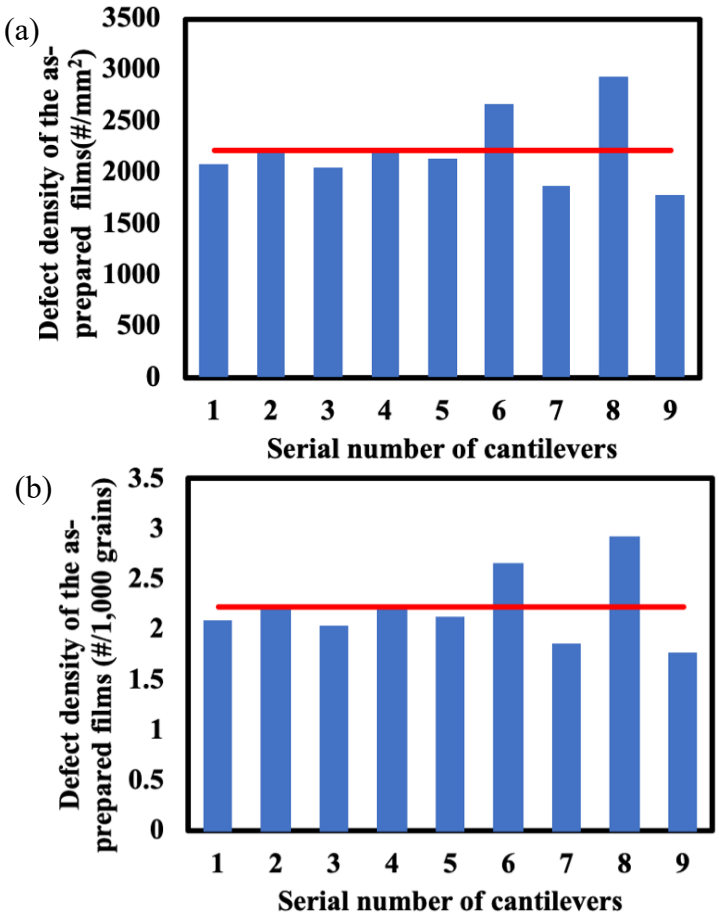


Figure 2.10. Plots show defect density exhibited as (a) defect/area; (b) defect/1,000 grains of the as-prepared PVD tin films. The orange line in the plots indicates the average defect density.

The nucleation process for new surface defects follows a "dwell-pop-up" process as shown through stage I and stage II. Stage I refers to few or no surface defects formation before some critical number of cycles. It is about 75M and 250M cycles for the first and second mode vibration, respectively. For example, there were even no surface defects formation before 21.6M cycles for sample 1 of the second mode vibration. This indicates stress accumulation through fatigue damage for defect nucleation despite continuous stress relaxation. Once the threshold stress is overcome, the main period for the nucleation of new surface defects shows up with outburst of most surface defects (stage II). This varies with different samples, and the range of cycle numbers is from 125M-500M cycles. By still using sample 1 of the second mode as an example, a small quantity of surface defects showed up at 43.2M cycles and remained constant until 150M cycles, with a few more shows up at about 250M cycles. The majority of surface defects nucleated between 21.6M cycles

and 400M cycles with most surface defects popping up between 250-350M cycles. The wide range of stage II may relate to grain orientation difference of the as-prepared films for different modes. The increase in surface defect formation becomes much slower at some critical number of cycles with the final steady density of about 1160-1380/mm$^2$ (stage III). This steady stage can be either a permanent saturation of defects with this specific cyclic bending situation or another incubation stage for the "dwell-pop-up" process, which may be similar as stage I shown here. Only more cyclic bending can distinguish the mechanism. The number of cycles to initialize stage II and achieve the ultimate steady defect density for the first mode (Figure 2.11 (b)) is much smaller compared to that for the second mode (Figure 2.11 (a)), indicating a more rapid stress accumulation and relaxation for the first mode. The overall stress accumulation during cyclic bending is critical for surface defect formation, and it corresponds to the "creep" model in previous research [42].

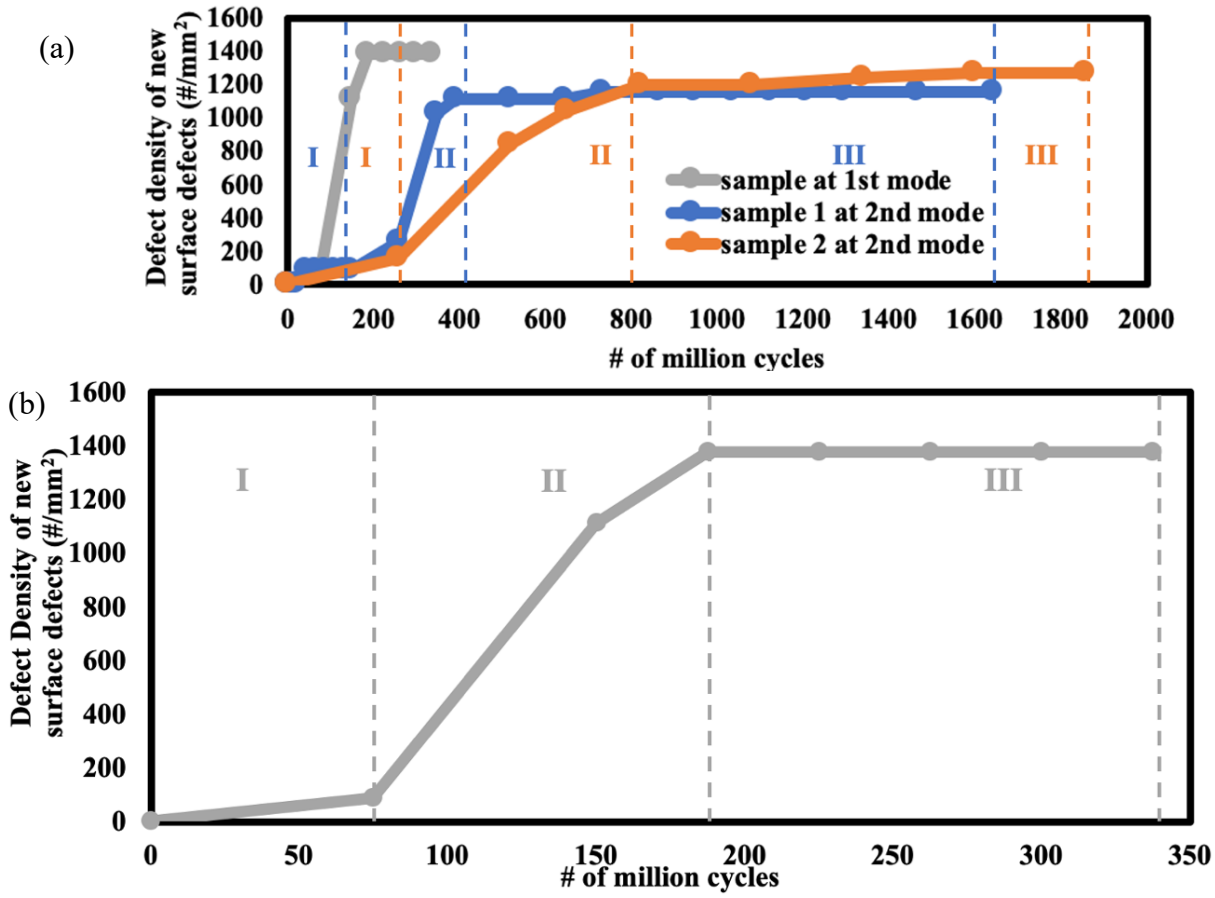


Figure 2.11. (a) Plot shows new surface defect density per area as a function of cyclic numbers for both the first and second mode; (b) magnification of the analysis for the first mode. The "I", "II", "III" refers to the three distinct stages for defect density increase during cyclic bending.

Figure 2.11 reveals the relationship between stress accumulated across the whole cantilever and cyclic numbers, and the influence of strain distribution along the cantilever can be figured out through the number of surface defects as a function of distance from the free end (Figure 2.12). The black dashed line showed the absolute value for the strain distribution along the cantilever got by Eq. 2-2. For both modes, there are no new surface defects approaching the free end of the cantilever, and nucleation of surface defects only showed up in area from the fixed end to about 50 % and 80 % of the whole length for first mode and second mode vibration, respectively. The lack of surface defect formation approaching the free end of the cantilever indicates that there is a critical strain amplitude per cycle for defect formation. The tendency for surface defect density agrees well with the tendency for strain distribution, and the position with highest absolute strain has the highest defect density. This means that strain amplitude is critical for defect formation at a designated frequency and number of cycles in addition to the stress accumulated through increasing number of cycles (Figure 2.11). According to the model established by Trinks and Volkert [42], the mechanism for defect formation during this ultra-high frequency cyclic bending should be the combined effect of "creep" and "dislocation glide" model. The effect of strain amplitude along the cantilever is more obvious for the second mode with spread of defects along the cantilever while the defects concentrate near the fixed end for the first mode. The maximum number of surface defects along the cantilever is 10 for the first mode, which is almost 50 % more than that for the second mode with a value of 7. It reflects statistics limitation for cyclic bending of AFM cantilevers.

It can be obtained from Figure 2.12 that the total number of surface defects for the first and second mode is 31 and 26, respectively. With a grain size of 1 $\mu$m (Figure 2.1) and a similar height of 1.2 $\mu$m (Figure 2.7), the total volume of the defects is about only 24.4 $\mu m^3$ and 20.4 $\mu m^3$ for the first and second mode, respectively. The area of the film surface is 22500 $\mu m^2$ (450 $\mu$m * 50 $\mu$m), and the corresponding change of film thickness during the cyclic bending is only 1.08 nm and 0.91 nm for the first and second mode, respectively. The film thickness is almost constant during the cyclic bending, and it indicates limited mass transport and diffusion for defect formation during cyclic bending of AFM cantilevers that will be discussed in detail.

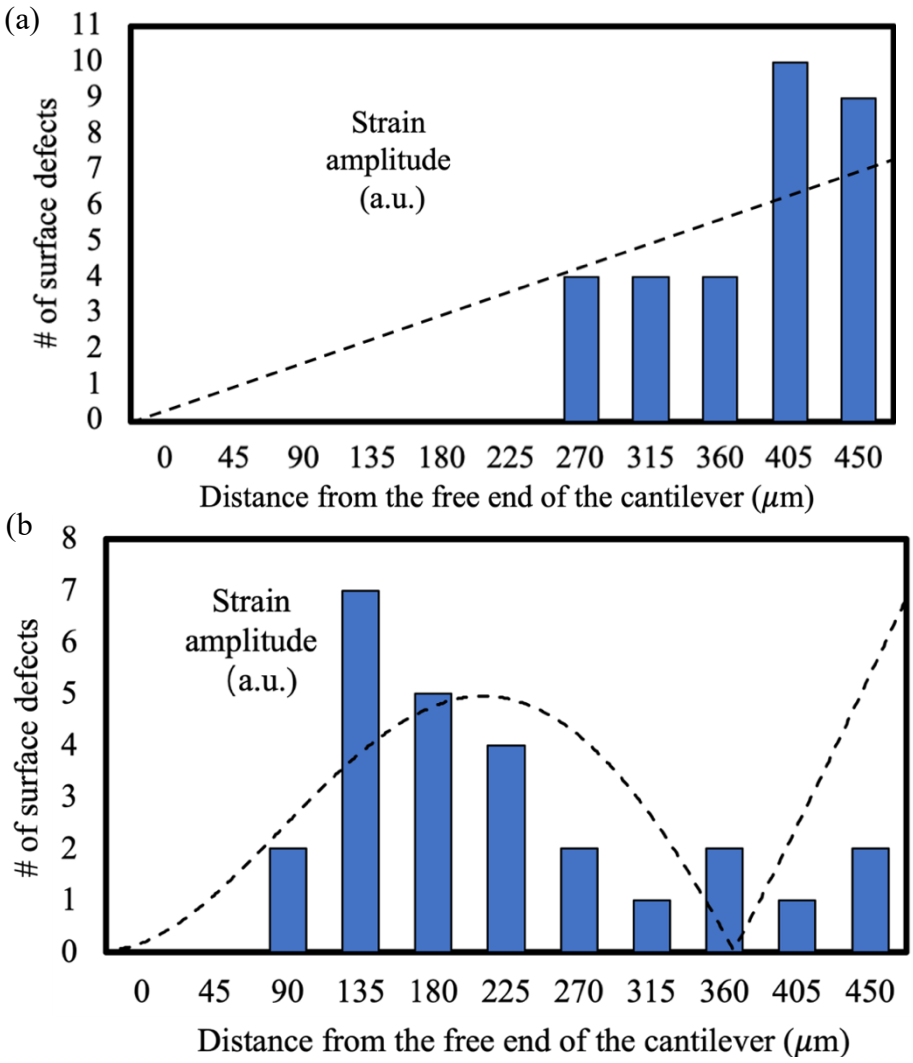


Figure 2.12. Plots show number of surface defects along the cantilever at stage III in Figure 2.9. (a) first mode vibration; (b) sample 1 of second mode vibration. The dot line indicates the form of absolute strain distribution along the cantilever.

### 2.3.3 **Discussion for The Behavior of PVD Tin Films During Cyclic Bending**

The surface defects with striation steps on the surface after millions of cycles vibration and the "dwell-pop-up" process for the relationship between surface defect density and number of cycles are both interesting phenomena that can be explained through the "stick-slip" mechanism during the defect formation. It is a consensus that the static friction coefficient is larger than the kinetic friction coefficient. Based on the previous GB sliding model [12,34], the force acting at the whisker base should firstly overcome the static friction as well as break the surface oxide to activate GB sliding. Since the kinetic dynamic friction coefficient is smaller than the static friction

coefficient, the sliding accelerates once the force exceeds the static friction due to the decreasing friction resistance in dynamic mode motion. The force to sustain the sliding decreases with continuous stress relaxation. Therefore, the sliding slows down until the force drops below the static friction limit. The oxide forms again, and defect growth stops. Then the driving force for out-of-plane growth needs to accumulate again to repeat the as-mentioned "static-dynamic" friction process for continue growth of existing surface defects and more nucleation of surface defects. This helps explain the phenomenon that the number of striation steps on film surface does not correspond exactly to the number of cycles (Figure 2.6 and Figure 2.8). The formation of striation steps only happens during the dynamic friction period, which leads to the fewer striation steps than the actual number of cycles the film experienced. Persistent slip bands (PSB) can be easily created during cyclic bending due to the formation and accumulation of mainly edge dislocations. The evolution of PSB leads to the striation steps on the defect surface, which verifies the role of dislocation motion during cyclic bending. The nucleation of new surface defects also happens during the dynamic friction period, thus there is an incubation time before the outburst of surface defects (Figure 2.11). It is similar to what has been observed for thermal cycling with the out-of-plane growth only occurs during the heating half cycle [35]. For whisker growth due to RT IMC formation, the striations are irregularly spaced, reflecting a stick-slip growth mode and changes in the whisker diameter by GB migration [18]. The average height of the defect is 1.2 $\mu$m and the cyclic experiment was done for at least hundreds of million cycles, thus the average growth height for each cycle is far less than 1 nm. It is too small to be observed with SEM images. The fact that significant defect growth can be seen between striations also verifies that the number of striations is smaller than the cyclic numbers during this ultra-high frequency cyclic bending. Since the total volume of all the surface defects is only related to the surface defect density with the similar height of surface defects (Figure 2.7), it is proportional to strain amplitude due to the positive correlation between defect density and strain distribution (Figure 2.12).

To observe the evolution of surface defect morphology, the cyclic bending experiment done in this research is stopped several times during the whole process, which can be named as "interrupted cyclic bending", contrast to "continuous cyclic bending" without any interruption. One big issue with interrupted cyclic bending is that there is continuous stress relaxation including when the cantilever is static while stress accumulation only happens during dynamic cycling. It is hypothesized that the global stress remaining in the film after the first interruption is almost fully

relaxed before cyclic bending for additional cycles. Thus, more numbers of cycles are needed to satisfy the threshold local stress for surface defect formation. This also contributes to the dwell-popup process for surface defect formation with increasing number of cycles (Figure 2.11). Once the stress accumulated during cyclic bending cannot overcome continuous stress relaxation, saturation for the number of surface defects happens as one of the hypotheses explaining stage III in Figure 2.11.

There may also exist a load drop for the strain amplitude in each cycle that leads to limited nucleation and lack of defect growth due to the corresponding decreased stress. The sources of the drop are multiple. It can be formation of cracks and pores (Figure 2.9), local tension at the GBs beneath surface defects with continuous mass transport from GBs to sustain defect growth, and local plastic flow caused by Coble creep. The decreased stress is hypothesized to be too small to overcome the GB sliding [12,34] to achieve nucleation of new defects and sustain defect growth.

The SEM imaging process may also play a role in evolution of surface defects. The immersion mode of SEM is used for ultra-high magnification imaging in order to increase the resolution, and it leads to local surface damage due to electron concentration and a thin C layer deposition in this limited local area. The damaged area may prevent the subsequent defect growth. The C layer can function similar as the oxide layer on film surface [12,24,34], and it increases the difficulty for defect growth for the requirement of breaking both C and oxide layer on film surface instead of only breaking oxide layer for Sn surface defect formation under other conditions. The accumulated stress may never reach a critical stress to sustain defect growth.

As mentioned earlier, the critical condition for defect growth is that the driving shear force on the GBs parallel to the direction of growth can overcome the force caused by GB sliding [12,34]. The growth rate of whiskers and hillocks is determined by the coupling of GB sliding coefficient and surface grain geometry. A high GB sliding coefficient or deep grains is favorable for short defect formation due to the low growth rate. Though both grains with a shallow grain geometry (Figure 2.5 (b) and (d)) and grain with cylindrical geometry (Figure 2.5 (e)) can develop into a surface defect, their growth rates are different. For shallow surface grains, the whiskers are short even with the preferred grain geometry for defect growth, indicating high GB sliding coefficient. The influence of GB sliding dominates over that of surface grain geometry. For defect growing through the thickness of the film to the film surface, the deep grain geometry already has an adverse influence for defect growth regardless of the GB sliding coefficient.

### 2.3.4 **Evolution of Electroplated Tin Films Morphologies**

Figure 2.13 shows the SEM images of the as-prepared electroplated tin films with a grain size of about 3 $\mu$m. The surface morphology of electroplated tin films (Figure 2.13 (a)) on PVD Cu/as-received Si cantilevers is a little different from the tin film on Cu substrate or as-plated Sn films on PVD Cu/as-received Si substrate for samples with large dimensions [23]. It shows more roughness with wrinkles, and it may relate to the small dimensions of AFM cantilevers. Even through the same current density was used in the electroplating process, it can vary a lot even with small current difference. For instance, the current density may vary 4.45 A/cm$^2$ with only 1 mA difference. It is hypothesized that the difference of current density is a critical parameter for controlling surface defect morphology [17]. The free end of the cantilever has a very sharp tip (Figure 2.2 (d)), and this leads to a high divergence electric field with large local charge density, causing significant unbalanced electric field during electroplating process, and this is hypothesized to be another possible reason for the rough film surface.

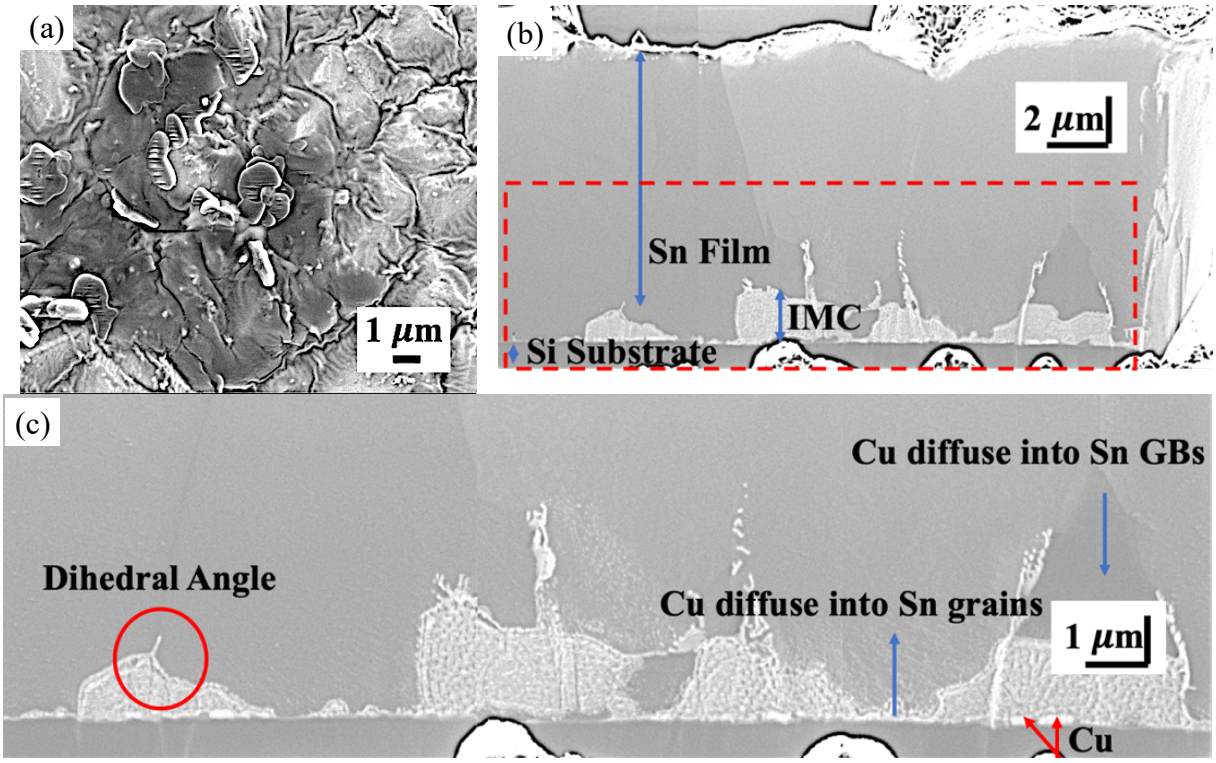


Figure 2.13. SEM images of the as-prepared electroplated tin films. (a) surface morphology; (b) cross-section image by FIB cut; (c) enlarged image of the marked area in fig. (b)

The IMC layer grew at the interface between Cu and tin films by diffusion of Cu into Sn grains and GBs, as exhibited in the cross-section images (Figure 2.13 (b) and (c)). The film thickness is about 12 $\mu$m, much thicker than that for PVD films. The remaining of Cu near the interface decreases with time as Cu reacted with Sn to form IMC. The dihedral angle between GBs and IMC interface (Figure 2.13 (c)) has an effect on stress evolution due to the force balance requirement at this special site, thus influencing the final stress relaxation response.

The evolution of the electroplated films is shown in Figure 2.14. As contrast to PVD films, no new surface defects showed up with increasing number of cycles. The only stress relaxation mechanisms are cracks and partial fall-off of pre-existing surface defects. The cracks became more severe with both increasing crack length and width for addition cyclic bending (compared between Figure 2.14 (e) and (f)). This is related to the incompatible stress at GBs as mentioned before.

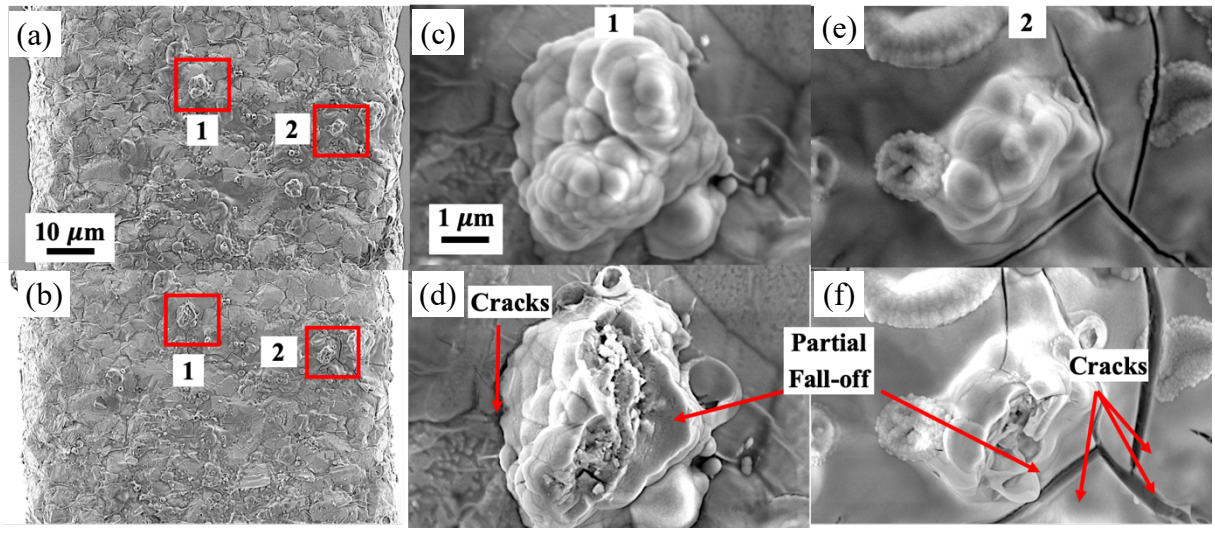


Figure 2.14. SEM images show the evolution of the same area on electroplated tin films during cyclic bending. (a), (c), (e) after 48M cycles; (b), (d), (f) after 348M cycles. "1" and "2" are features on film surface. (c), (d) enlarged image of the feature 1; (e), (f) enlarged image of the feature 2

### 2.3.5 **Effect of Film Preparation Methods on Stress Relaxation Mechanism**

The previous sections discussed the responses of tin films prepared by different methods for cyclic bending of AFM cantilevers. The dominated stress relaxation method for PVD film are short whiskers whereas that for electroplated films are cracks and partial fall-off.

One possible hypothesis for this difference is related to the role of IMC during cyclic bending. With 300 nm Cu layer beneath the electroplated film, the formation of IMC may change the stress

state of the film thus influence the response to fatigue damage accumulation. The $Cu_6Sn_5$ IMC is much harder and has larger elastic modulus than Sn [51], and it causes much higher strain in tin films than in IMC layer under stress during the cyclic bending. Thus, tin films break firstly with integral IMC layer beneath it, leading to the cracks on the film surface (Figure 2.14 (e) and (f)).

Another hypothesis is due to the influence of obvious film thickness difference in the stress relaxation and mass transport process. Chason et al. [50] conducted a series of experiment with two sets of tin film conditions, one is different film thickness with corresponding different grain size and the other is different film thickness with similar grain size by "etching back" method. It is confirmed that the IMC growth rate is greater for larger grain size but does not depend on the thickness of Sn layer. The steady state stress depends on the layer thickness even when the grain size is kept constant. The whisker density is always lower for thicker films due to the smaller steady state compressive stress. Relaxation is enhanced by increasing the length both in the vertical and horizontal direction. The film thickness difference may influence IMC volume and stress as well as whisker density for room aging experiment, and this also happens during cyclic bending experiment. The stress relaxation is more rapid for thicker electroplated films, thus suppresses defect formation. Instead, cracks and partial fall-off become the dominant response of tin films during cyclic bending as a result of coupling between different stress relaxation mechanisms.

### 2.3.6 **Measurement of Real-time Strain amplitude/Tip displacement**

As mentioned above, there is no grain growth of both pre-existing and new surface defects for PVD and electroplated films though there are limited nucleation of new surface defects on PVD films. Based on the whisker growth model through GB sliding controlled creep [12,34], the force at the whisker base, which is generated by stress during the compressive half cycle, should overcome the sliding friction and break the oxide layer on the film surface to sustain whisker growth. Thus, it is hypothesized that there is not enough fatigue accumulation per cycle due to small strain in the film to provide the driving force. The laser doppler vibrometer (LDV) system is an efficient apparatus to check the strain amplitude distribution through monitor of real-time displacement along the cantilever during cyclic bending.

The mechanism and principles of LDV system are quite similar to the non-contact mode of AFM. The system can achieve the measurement of out-of-plane velocities by interferometry of phase [52]. The magnitude of the velocity can be changed through control of the excitation voltage

since the voltage varies linearly with the out-of-plane velocity. The phase is determined by the reflection of backscattered laser light from the surface for each scanning point. The scanning pattern consist of several scanning points measured automatically in just a single test by scanning LDV system [53]. Since the velocity is a product of displacement and vibration frequency, the displacement along the cantilever can be easily calculated with settled frequency.

For the first mode vibration, there exists a relationship between base displacement controlled by voltage driving piezoelectric and the tip displacement, as shown clearly in Figure 2.15 (a). The absolute tip displacement is the sum of base displacement generated by input vibration voltage and the relative tip displacement to the base. To get the exact correlation, different voltages were used to drive piezo actuator in LDV system, and the base and tip displacement were monitored simultaneously. It can be seen in Figure 2.15 (b) that there is a linear relationship between the tip and the base displacement. The base displacement is negligible compared to the tip displacement, which verifies the hypothesis of fixed end near the shoulder of the cantilever.

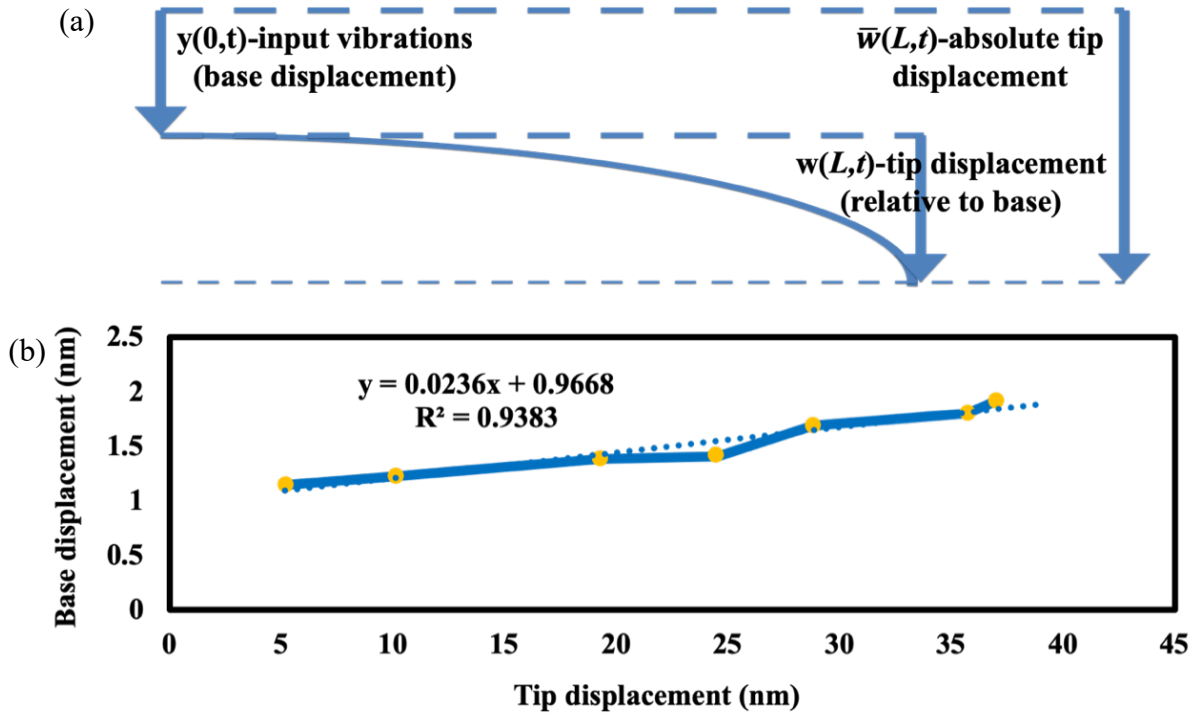


Figure 2.15. (a) schematic image; (b) actual measurement by laser doppler vibrometer (LDV) system showing the relationship between base and tip displacement during cyclic bending

The maximum displacement $u_z^{max}$ achieved at the free end of the cantilever measured by LDV is converted to strain amplitude along cantilever $\varepsilon_a(x)$ for the first mode vibration [44]:

$$\varepsilon_a(x) = \frac{3u_z^{max}h}{2L^3}(L - x) \qquad \text{Eq. 2-3}$$

Where $L$ is the length of the cantilever, $L$=450 $\mu$m; $h$ is the total thickness of the cantilever, including the thickness of both the substrate and the film; $x$ is the distance from the fixed end (base) of the cantilever. With this relationship as well as the correlation between the base displacement controlled by voltage driving piezoelectric and the tip displacement (Figure 2.15 (b)), the strain and the driving voltage can be associated (Figure 2.16). For electroplated film, the film thickness $h$ is about 14 $\mu$m (substrate 2 $\mu$m + film 12 $\mu$m). By using the maximum voltage applicable for LDV system of 10 V to drive the cantilever at resonant frequency with sine function, the measured maximum displacement at $x = L$ is 30.70 nm. The maximum strain amplitude at x = 0 can be calculated with a value of only 0.00032 % by using all the above data into Eq. 2-3. This is far less than 0.1 %, and it indicates that the base excitation by the vibration voltage is not enough. The maximum driving amplitude for AFM is even much smaller, only 800 mV. It can be inferred that the strain amplitude is smaller for this voltage of 800 mV. This small strain is the main reason for the minor changes of tin films on AFM cantilevers during cyclic bending.

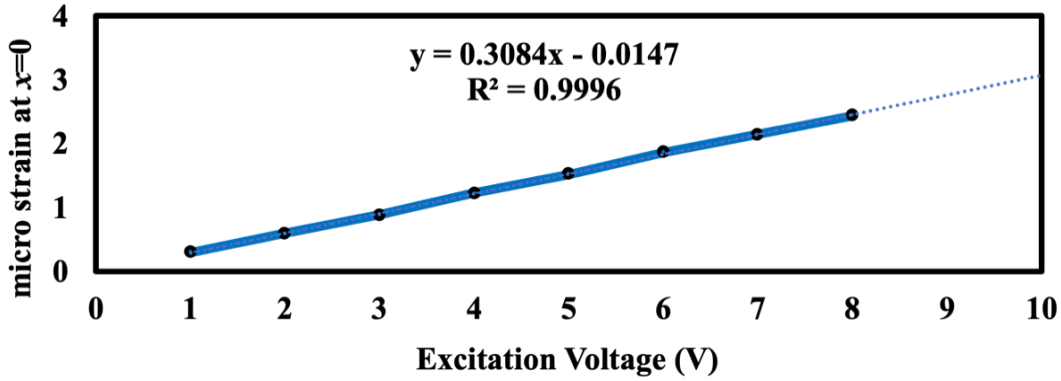


Figure 2.16. Plot shows relationship between the maximum micro strain and excitation voltage at $x$=0 (the fixed end of the cantilever) obtained by LDV system

As shown in Figure 2.11, the final constant defect density of stage III is in the range of 1160-1380/mm$^2$, and it can also be expressed as 1.16-1.38/1,000 grains. Research has been done to focus on tin films with similar grain size under ambient storage conditions. Chason et al reported that the defect density for 1.45 $\mu$m thick films (with a grain size of 1.42 $\mu$m) under 150 h room aging

conditions is 300/mm$^2$ [50]. In previous studies for electroplated 1 $\mu$m tin films prepared using an alkaline bath, the defect density is about 70/mm$^2$ and 350/mm$^2$ after aging for 1000 h and 4500 h, respectively [54,55]. This indicates that the surface defect formation process is promoted for the ultra-high frequency cyclic bending in this research compared to that for room aging. For thermal experiment, there is no pre-existing research focusing on tin films with similar grain size. Thus, defect per 1,000 grains instead of defect per area was used as the comparison to eliminate the effect of grain size. The defect density for 2.5 $\mu$m electroplated tin films after thermal aging at 75 $^o$C for 2 h is 1.5/1,000 grains [56], and it is similar to the defect density in this research. The high temperature may cause GB migration and influence the preferred nucleation sites for defect formation, and it also promotes defect formation. For RTC with temperature range of -40 $^o$C and 85 $^o$C on 5 $\mu$m electroplated tin films [35], the maximum defect density is about 37.5/1,000 grains after 20 cycles. This is much higher than that for cyclic bending experiment in this research, and it is hypothesized to be resulted from different surface grain morphology and geometry as well as the initial stress state of tin films caused by the PVD and electroplating process. The stress caused by CTE mismatch during thermal cycling may also play a dominate role to accelerate defect formation compared with the negligible strain distribution along the cantilever during cyclic bending in this research (Figure 2.16).

Sn shows a low modulus at RT due to the high homologous temperature at RT ($\approx$0.58 RT). The small strain amplitude guarantees the elastic regime for the cyclic process, and it leads to the small stress along the cantilever. The global deformation is mostly elastic and deformation by defect formation only occurs at particular local sites due to the specific grain orientations and localized elastic strain energy leading to limited nucleation sites facilitated by creep in response to localized plastic deformation. Creep processes such as Harper-Dorn Creep controlled by dislocation motion and Coble creep with vacancies moving along GB can happen during the cyclic bending at some local sites with highly localized plastic stress. Coble creep is the dominated behavior for tin films due to the higher diffusivity for GB compared to that for dislocation core. The coupling and competition between creep and defect formation as stress relaxation mechanisms making the analysis more complicated [57].

To achieve the large strain of 0.1 %, the corresponding excitation voltage should be 3.33 kV based on the relationship shown in Figure 2.16. This is beyond the range of AFM and LDV system.

The only solution is using new piezoelectric and amplifier for LDV system to achieve ultra-high frequency cyclic bending, and this is beyond the scope of the research shown here.

The pervasiveness and effectiveness of this research method is restricted by the small dimensions of the samples due to the poor statistics. There is only a total of 22500 grains for PVD tin films on the sample and the number of total grains is even smaller for electroplated films with larger grain size, and it leads to the limited defect density with this small amount of grains. The maximum number of surface defects along the cantilever for both first and second mode vibration for PVD films is only equal to or less than 10, and the extreme situation is only one surface defect in two regions for the second mode vibration (315 $\mu$m and 405 $\mu$m in Figure 2.10 (b)). For the statistic issues, large cantilevers with more grains can be a good option for the future research work, and it will be discussed in detail in the following chapters.

The evolution of GB geometry beneath defects from preferred shallow grain geometry for defect growth to other geometry after defect nucleation is hypothesized to be one possible reason for no additional growth after the defect nucleation. A systematic analysis from FIB images at defect sites can be prospective work in the future.

## 2.4 **Summary**

In this work, an ultra-high frequency method for cyclic bending of tin films on AFM cantilevers has been successfully developed. Two kinds of films prepared by different methods were used, namely PVD films and electroplated films. The evolution of film morphology with increasing number of cycles was followed for both films. The quantitative analysis of defect formation with various parameters including position along the cantilever and increasing number of cycles were discussed in detail for cyclic bending of PVD tin films. The surface defect densities and their morphologies at low strains provide guidelines for comparison not only with tin films stressed under other conditions but also with Cu film cyclic bending results obtained using lower stiffness silicon nitride AFM cantilevers. Finally, the related mechanism and hypothesis for the response of the films were thrown out. The major conclusions were:

(1) Films prepared by different methods show different stress relaxation mechanisms during cyclic bending. Short whiskers with low height/diameter ratio and rotated surface defects are the dominated surface defect morphologies for PVD films. The rotated surface defects and steps on the defect surface indicates asymmetrically growth rate and “stick-

slip" behavior, respectively. There are only cracks and partial fall-off for electroplated films during cyclic bending. Both film thickness and IMC formation influence the dominated stress relaxation mechanisms for tin films prepared by different methods.

(2) For both pre-existing and new surface defects on PVD films, they did not show any growth tendency after its initial appearance with additional cyclic bending. The number of new surface defects was also very small. The insufficient strain amplitude checked by LDV system, continuous global stress relaxation as well as the evolution of film surface and GB geometry during the process may all play a role in suppressing the defect nucleation and further growth after its initial appearance.

(3) Whatever type of stress relaxation mechanism is for both films, the damage of the film corresponding to the surface defect density becomes more severe with additional number of cycles. It indicates that the fatigue damage accumulation is very important for the nucleation of surface defects.

(4) The surface defect density distribution goes well with the strain distribution along the cantilever for both the first and second mode cyclic bending of PVD films, indicating the critical influence of strain amplitude for surface defect formation.

# 3. CYCLIC BENDING OF LARGE CANTILEVERS IN MM RANGE FOR INTERRUPTED CYCLING

## 3.1 **Motivation**

Cyclic bending of AFM cantilevers cannot provide enough stress accumulation for surface evolution, and one alternative solution is switch attention to large cantilevers in mm range. For AFM and large cantilevers vibrated at the same driving voltage, the displacement along the cantilever is more obvious for large cantilevers in mm range due to its dimensions. According to Eq. 2-3, this can provide a significant strain amplitude difference. The large displacement can be achieved with a low driving voltage, and it can fit the operating requirement for LDV system.

There are multiple advantages for using large cantilevers besides the obvious strain amplification. The thickness of electroplated tin film is always in $\mu$m range. The film thickness has significant influence for cyclic bending of AFM cantilevers with comparable thickness of the film (several $\mu$m) and the substrate (2 $\mu$m). Their influence can be neglected for large cantilevers, considering the calculation of the moment of inertia *I* through Stoney's equation.

There exists an equation to calculate the resonant frequency $f_{res}$ by considering the mechanical state and design of the cantilever [44]:

$$f_{res} = \frac{1}{2\pi} \cdot \frac{3.52}{L^2} \cdot \sqrt{\frac{EIL}{m_0}} \cdot \sqrt{\frac{m_0}{m_0+m_{att}}} \qquad \text{Eq. 3-1}$$

Where $L$ is the length of the cantilever, $E$ is the modulus of the substrate (ignoring the influence of the film due to its small thickness), $m_0$ and $m_{att}$ are the mass of the cantilever and the weight attached at the free end of the cantilever, respectively. For large cantilevers, $f_{res}$ is proportional to $(m_0 + m)^{-1/2}$ according to Eq. 3-1. The slope of strain distribution along the cantilever and maximum strain amplitude at the fixed end can also be alternated (Eq. 2-3) by adding different weight at the free end. Thus, research based on cantilevers vibrated at different frequencies can be done to obtain the frequency and slope of strain distribution effect for cyclic bending of cantilevers. The large dimensions and corresponding heavier weight of large cantilevers can lead to frequency decrease drastically compared to that for AFM cantilevers. The effect of frequency in different magnitude range and film thickness can be analyzed when comparing the results between AFM and large cantilevers.

## 3.2 **Procedures**

The fabrication and cyclic bending process is quite similar to that for electroplated films on AFM cantilevers. The same reaction ion etching for fabrication of Si substrate [44] was used to fabricate cantilevers (10 mm * 2 mm* 0.3 mm) from Si wafers. An additional basal square area of 100 $mm^2$ (10 mm * 10 mm) connected to the cantilever was fabricated simultaneously to facilitate the pickup and transfer of the sample. The geometry of the sample was shown in Figure 3.1 (a). The PVD Ti & Cu interface were prepared with the same thickness and method as in the previous electroplated tin films on AFM cantilevers. The current density during the electroplating process was 10 $mA/cm^2$ with a commercial electroplating solution (Dow Solderon SC). The as-prepared films were similar to films investigated for many aging and thermal cycling experiment and have a reproducible surface morphology [18,27,35,50,56,58]. Figure 3.1 (b) exhibits the assembly of the cantilever from the cross-section view. The cantilever was attached to a customized piezo actuator (Mide Technology) with a frequency range of 0-1.4 kHz. The vibration direction of the piezo actuator is in the z direction that can achieve out-of-plane vibration. Mass was attached to the backside of the cantilever near the free end to alter the first mode resonant frequency of the cantilever. The cantilever was attached to the piezo actuator, and then electrical wire was soldered on the piezo actuator which was connected to LDV system. The piezo actuator was placed on a fixed stage to minimize the additional vibration besides cyclic bending. The LDV system was used to measure the resonant frequency and the real-time displacement along the cantilever during the cyclic bending experiment. The arrangement of the cantilevers within the LDV system was schematically shown in Figure 3.1 (c).

Both the surface morphology evolution and quantitative analysis of defects were examined using SEM (Quanta 650, FEI) during each interrupted period. The cantilever was divided into equal areas to help reveal the defect distribution along the cantilever. Since the cyclic bending experiment is stopped several times until the ultimate number of cycles, the cyclic bending described in this Chapter is called “interrupted cyclic bending”, in contrast to “continuous cyclic bending” without any interruptions that will be analyzed in Chapter 4. To achieve the relationship between surface defect density with increasing number of cycles, the number of defects in each equal area was counted repeatedly after designated number of cycles until the ultimate cycle numbers. The cross-section of tin films was done by using FIB milling (Quanta 3d, FEI) to reveal the grain geometry of the surface grains and defects.

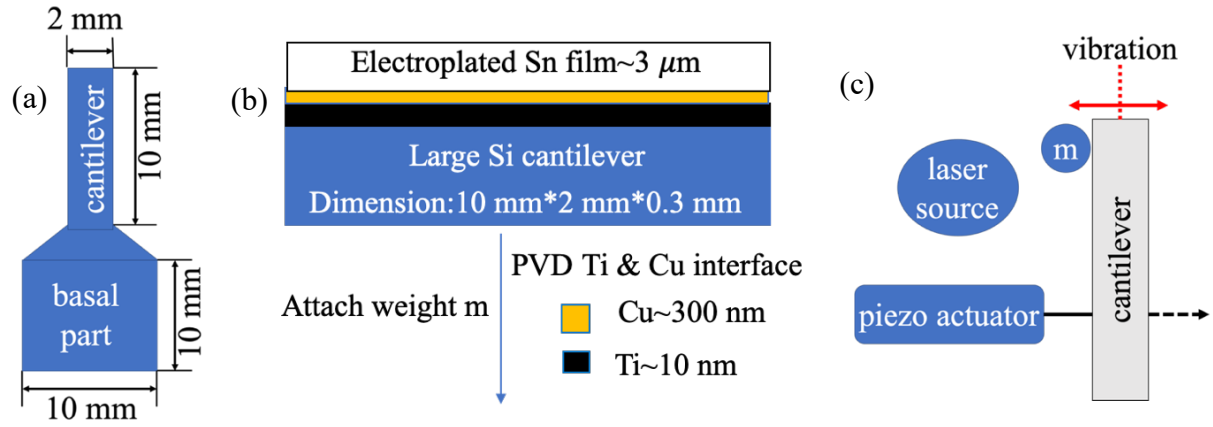


Figure 3.1. schematics show (a) geometry of the cantilever; (b) assembly of the cantilever from the cross-section view; (c) cantilever arrangement during cyclic bending in LDV system

## 3.3 **Results and Discussion**

### 3.3.1 **Evolution of Tin Films Morphologies**

The surface morphology of as-prepared films is similar to that of tin films prepared by using the same parameters in electroplating process for aging and thermal cycling experiment, as shown in Figure 3.2. The grain size is uniform across the film with a range of 2-5 $\mu$m (Figure 3.2 (a)). The film has a columnar grain structure with a thickness of 5 $\mu$m (Figure 3.2 (b)). IMC formed by diffusion of Cu into Sn grains and GBs is seen as the brighter regions at the interface in the cross-section image.

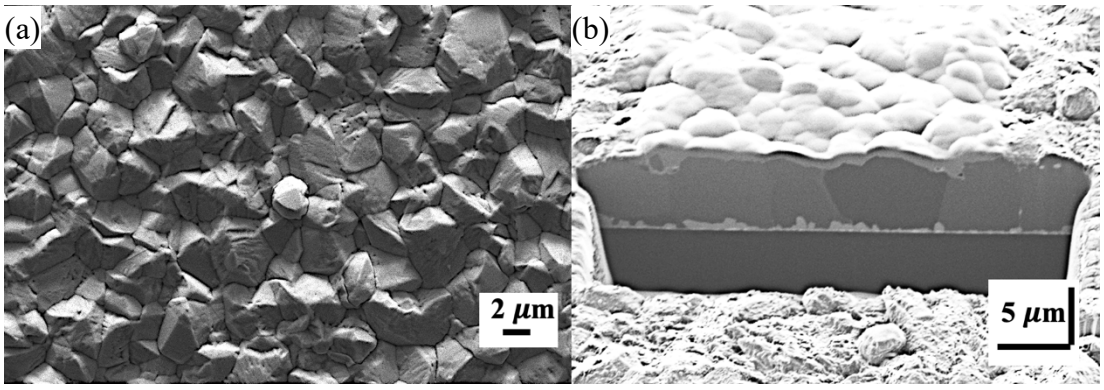


Figure 3.2. (a) SEM image show the uniform surface morphology of as-prepared tin films with a grain size of 2-5 $\mu$m; (b) the cross-section image by FIB cut for films with thickness of 5 $\mu$m. The white region approaching the interface is the IMC distribution.

Figure 3.3 shows the typical evolution of the same area on the film surface during the cyclic bending. The as-prepared film has few surface defects (Figure 3.3 (a)), and a large number of surface defects show up at the first interval of the cyclic bending (Figure 3.3 (b)). Once it is interrupted, increase for surface defect density with additional cyclic bending is much slower, as shown clearly compared between 5.4M (Figure 3.3 (b)) and 7.5M cycles (Figure 3.3 (c)).

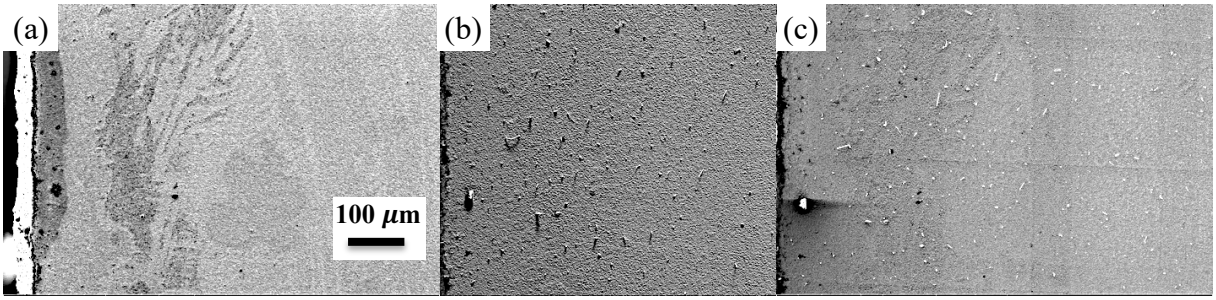


Figure 3.3. SEM images of the same area on film surface during cyclic bending. (a) as-prepared; (b) after 5.4M cycles; (c) after 7.5M cycles

With a magnified SEM image of the surface after the cyclic bending, three kinds of surface defects are observed as morphology evolution: micro-sized surface defects, nanowhiskers (NWs) and intragranular breakup (IGB) (Figure 3.4). Micro-sized surface defects are also main stress relaxation mechanisms for tin films using other conditions (room aging, thermal cycling, etc.). The diameter of NWs is far less than 1 $\mu$m, and its size is much smaller than the in-plane grain size. NWs are unique defects occurring in tin films during cyclic bending compared to tin films under other conditions as well as films of other materials systems during cyclic bending. IGB is a complex morphology with combinations of extrusions and intrusions. It is more complicated than extrusions or cracks defined in the cyclic bending of other materials systems [42–44,46,59]. The micro-sized surface defects, NWs and IGB are spatially close indicating different stress relaxation responses to the local stress state.

Figure 3.5 shows the length increases with change of growth direction for a pre-existing whisker during cyclic bending. The pre-existing surface defects are either IMC-induced surface defects or defect generated by plating stress during deposition process. A new micro-sized surface defect evolves from the in-plane grain with accumulated compressive stress (squared area in Figure 3.5 (a) and (b)). These are similar to what has been observed for tin films using other conditions.

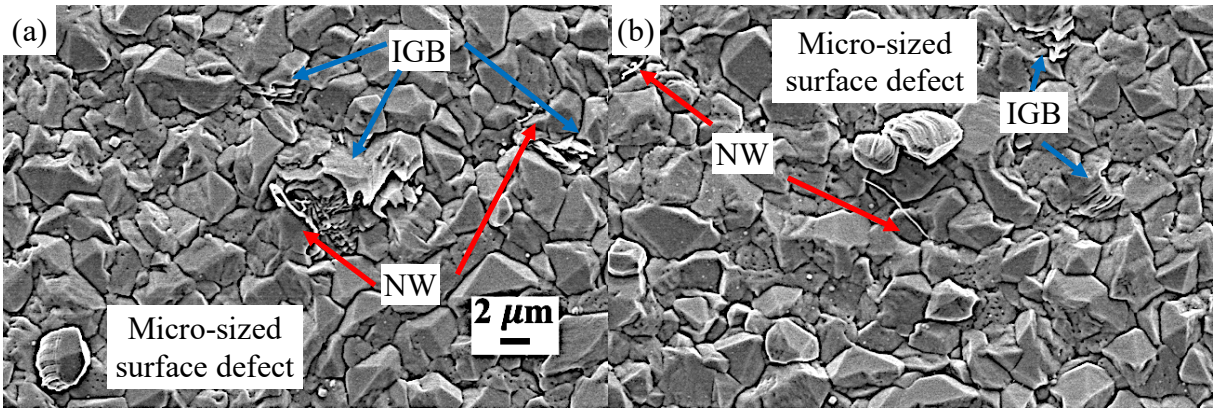


Figure 3.4. SEM images show typical surface morphology of tin films after cyclic bending

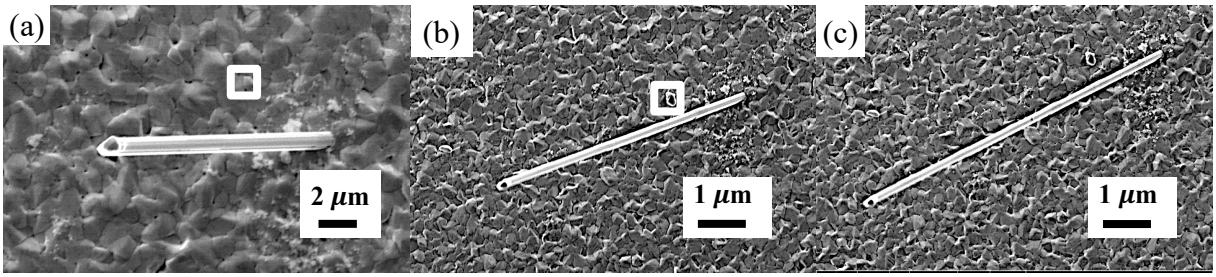


Figure 3.5. SEM images show evolution of pre-existing micro-sized whisker during cyclic bending. (a) as-prepared; (b) after 7.5M cycles; (c) after 14M cycles. The squared area in fig. (a) and (b) emphasizes the nucleation of a micro-sized surface defect from the in-plane surface grain.

The morphology of some micro-sized whiskers and hillocks is complex with increasing diameter from the top to the bottom, as shown clearly in Figure 3.6. The length and morphology also evolve during cyclic bending (compared between Figure 3.6 (a) and (d), (b) and (e), (c) and (f) respectively), similar to what is shown in Figure 3.5. Since Sn surface defect grows from the base to the tip [60] and the tip of the whisker is smooth (Figure 3.6 (g) and (h)) or with vertical striations showing the GB morphology of the defect (Figure 3.6 (i)), it corresponds to the initial rapid growth of the whisker upon nucleation. The larger base with horizontal striations is related to the cyclic bending process with material accumulation at the nucleation site due to the irregular diffusion and GB migration for the whisker growth.

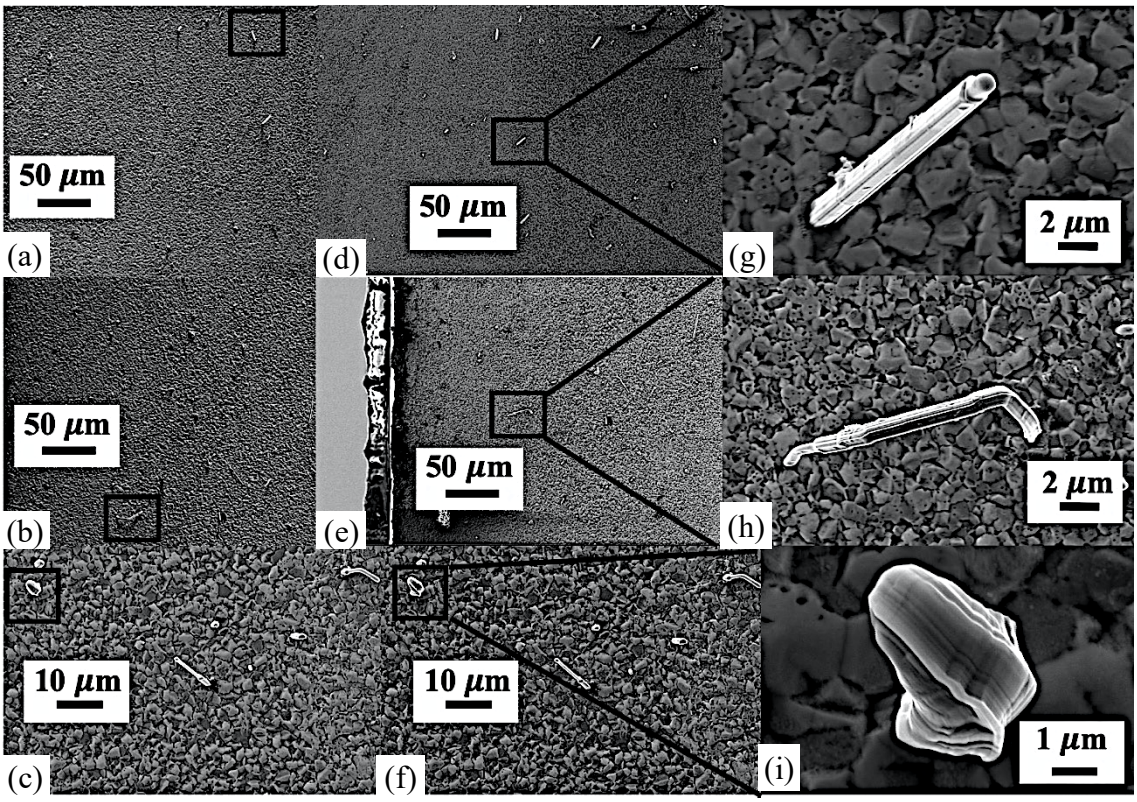


Figure 3.6. SEM images show evolution of micro-sized defects with striation base and smooth top. (a), (b), (c) after 5.4M cycles; (d), (e), (f) the same area of fig. (a), (b), (c) respectively after 7.5M cycles; (g), (h), (i) enlarged images of the rectangle area in fig. (d), (e), (f), respectively

There is no perfect match between the number of horizontal striations on the defect bottom and number of cycles, and it is similar to the striations on the short whiskers for cyclic bending of AFM cantilevers in Chapter 2. The crack tips move into the film along the GB of the whisker grain due to the crack propagation in each individual cycle. The following whisker growth with this movement of crack tips creates a striation ring on the side surface of whiskers, and it is similar to the mechanism for striation steps on surface defects for previous thermal cycling experiment [23]. More magnified SEM images showing the structure of the transition between the smooth top and striation bottom is exhibited in Figure 3.7. The space between the striations is small near the defect root with large space approaching the tip. The large space corresponds to the defect growth during the cyclic bending, and it is hypothesized that the space between striations approaching the defect root will also stretch out and move towards the whisker tip with additional cycles.

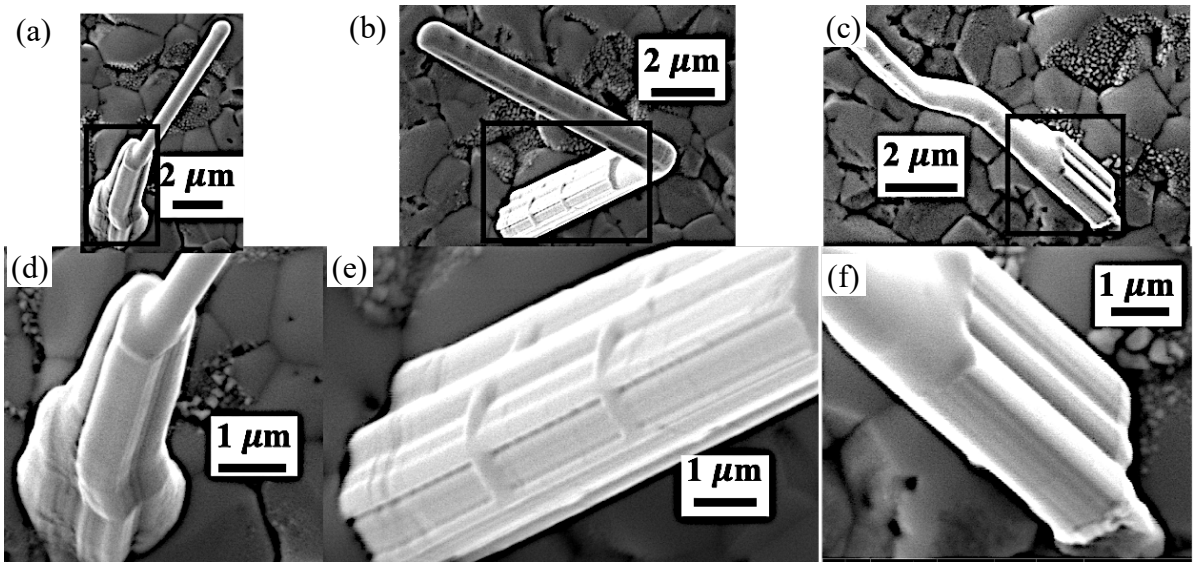


Figure 3.7. (a), (b), (c) Magnified SEM images of more micro-sized surface defects with smooth top and striation base; (d), (e), (f) the enlarged SEM images of the transition part between the top and the bottom marked in the rectangle area in fig. (a), (b), (c), respectively

The SEM images in Figure 3.8 show the formation of NWs during cyclic bending. After 3M cycles (Figure 3.8 (b)), there is a NW formed at a GB that shows no particular GB geometry or surface morphology compared to neighboring grains at 2.7M cycles (Figure 3.8 (a)). The direction and length of NW changes during the growth process with additional number of cycles (compared between Figure 3.8 (c) and (d)) after its initial appearance, and it is similar to the situation for evolution of micro-sized surface defects as discussed earlier. There is no obvious evolution for NWs from 4M (Figure 3.8 (d)) to 5M cycles (Figure 3.8 (e)). It is related to the stress accumulation for defect formation. The interrupted cyclic bending experiment slows the process for obtaining the critical fatigue accumulation, as mentioned earlier for the evolution of short whiskers on AFM cantilevers. The mechanism for accumulation of material at the NW base is similar to that for micro-sized surface defects, and it is related to GB migration and recrystallization at the nucleation site of NWs.

The materials accumulation at the NW root not only happens during the initial cycles (Figure 3.9 (c)), but also happens for additional cycles after interruptions (Figure 3.9 (d) and (e)). The diameter of the NW evolves during the cyclic bending at some critical point when the local coupling of the GB where the NW nucleates is activated. This helps sustain NW growth, and it transits the cross-section shape of the NW from a point with limited area to a broaden line along

the GB, indicating more portion along the GB is activated during the cyclic process. It is hypothesized that an increase in the nucleation area helps maintain the increasing required compressive force for NW growth due to the continuous stress relaxation.

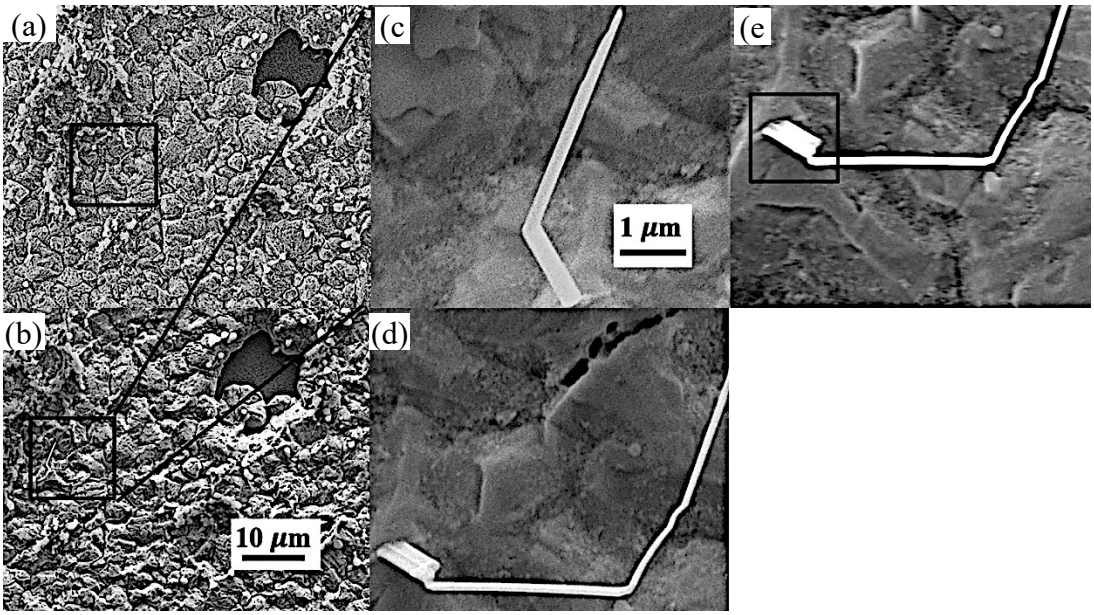


Figure 3.8. SEM images show the nucleation and growth of a nanowhisker (NW) during cyclic bending process. (a) after 2.7M cycles; (b) A NW shows up in the same area after 3M cycles; (c), (d), (e) enlarged images of the NW in fig. (b) after 3M, 4M and 5M cycles, respectively

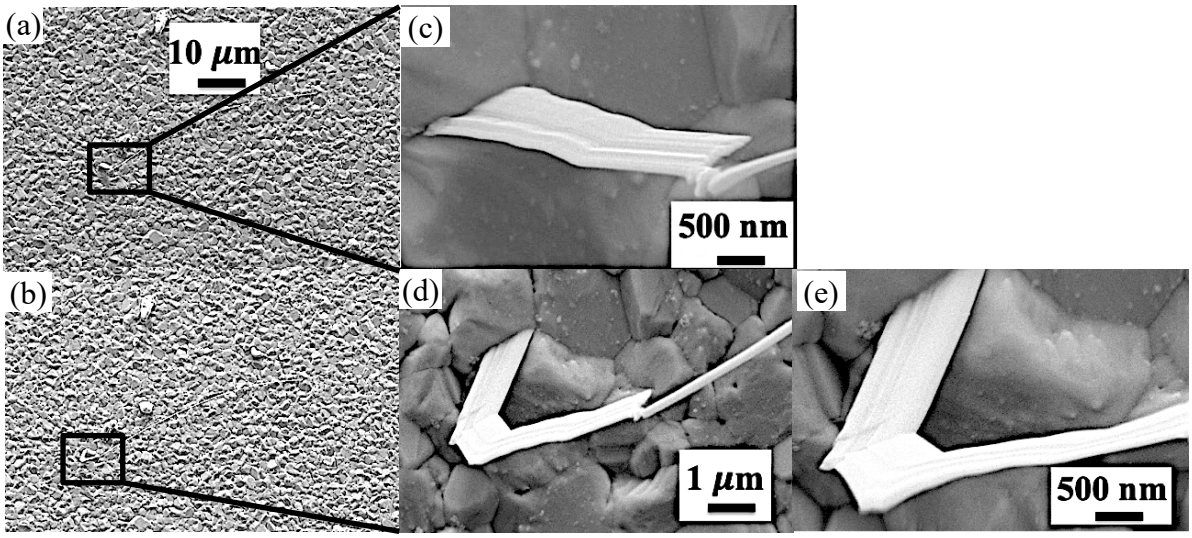


Figure 3.9. SEM images show growth of a NW with two distinct periods of materials accumulation during cyclic bending process. (a), (c) after 4M cycles; (b), (d), (e) the same area after 5M cycles; (c), (d), (e) enlarged images of NW root after 4M and 5M cycles, respectively

An example showing the non-steady state growth process for NW formation during cyclic bending is exhibited in Figure 3.10. A bamboo structure appears approaching the nucleation site of the NW (Figure 3.10 (e)). The growth of NW is achieved by mass deposition at the root via GB diffusion [21,61–64]. Each segment of the bamboo structure is related to stress relaxation during NW formation, and it is similar to the striation bottoms for micro-sized surface defects (Figure 3.6 and Figure 3.7). The distance between two neighboring segments corresponds to the "stick-slip" mechanism as discussed in detail for cyclic bending of PVD AFM cantilevers in Chapter 2. The "stick-slip" mechanism is related to friction and self-organized critical process [65]. The self-organized process is achieved when there is a transition into a marginally stable stationary state for a slowly driven system through scale-invariant avalanches [66]. NW growth happens during cyclic bending once the stress accumulation overcomes the static GB sliding friction at one segment, and it has an accelerating speed due to the decreasing friction resistance. The driving force decreases with NW formation as the stress relaxes, and the NW stops growing once the driving force is below the static friction limit. The stress needs to build up again to resume the NW growth, which creates another segment on the NW surface. The creation of each segment is regarded as a marginally stable stationary state through an avalanche in this research. More bamboo structure is expected with additional number of cycles, indicating the change of stress state during the cyclic bending experiment.

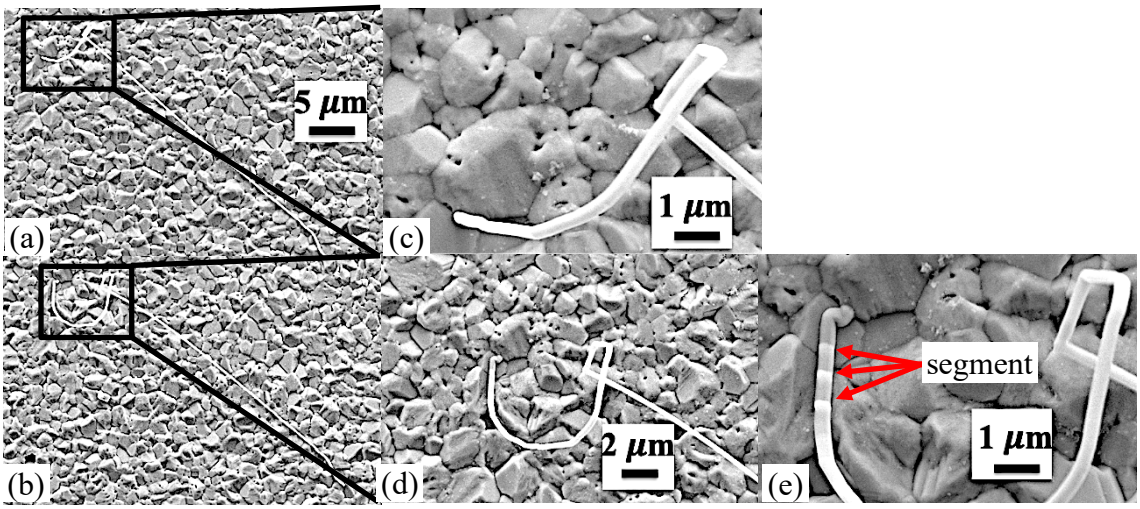


Figure 3.10. SEM images of bamboo structure approaching NW root during cyclic bending process. (a), (c) after 4M cycles; (b), (d), (e) the same area after 5M cycles; (c), (d), (e) enlarged images of the NW root after 4M and 5M cycles, respectively

The spot where nucleation of NW happens is assumed to be oxide-free since the break of oxide layer is the prerequisite for surface defect formation. It is similar to the critical condition for micro-sized surface defect formation [12,23,34]. This "weak spot" on the film surface can be a preferred site for the nucleation of another NW, as shown clearly in Figure 3.11. The length and growth direction of the former NW also changes during the cyclic bending (compare between Figure 3.11 (a) and (b)). Both NWs remain the same morphology for additional cycles (Figure 3.11 (c)). It is similar to the evolution NW shown in Figure 3.8 as well as the evolution of micro-sized surface defects. It is hypothesized that the mechanism and driving force for evolution of NWs are similar to that for micro-sized surface defects, regardless of the size effect. The vertical striations on the NW surface (Figure 3.11 (b), (d) and (f)) that are parallel to the growth direction of NW indicates zigzag GBs that are surrounding the NW. The above-mentioned "weak spot" created by the initial NW can promote the gathering and neighboring of multiple NWs, and an extreme situation is that a cluster of about 10 NWs with similar curvature in a limited local area shown in Figure 3.12. That no obvious change of the NW morphology after addition cycles (Figure 3-11 (e) and Figure 3-12 (b)) indicates the rebuild of oxide layer on film surface.

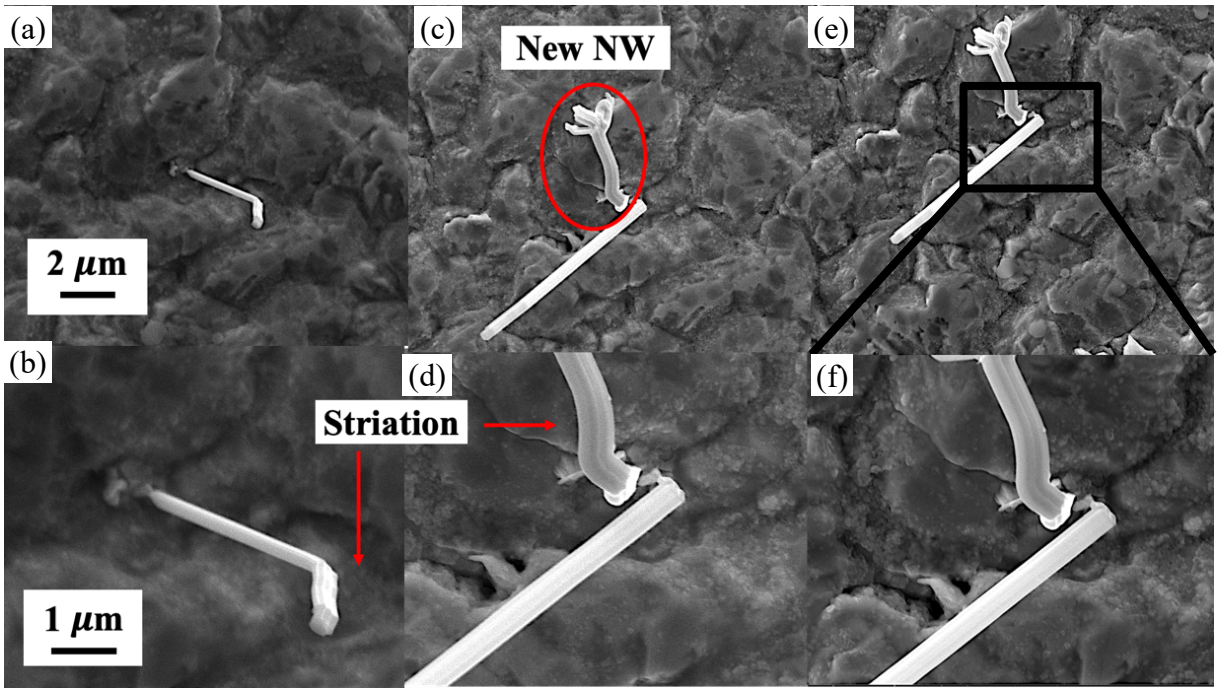


Figure 3.11. SEM images show that a new NW pop-ups at the site where a pre-existing NW has already existed. (a), (b) after 3M cycles; (c), (d) after 4M cycles; (e), (f) after 5M cycles

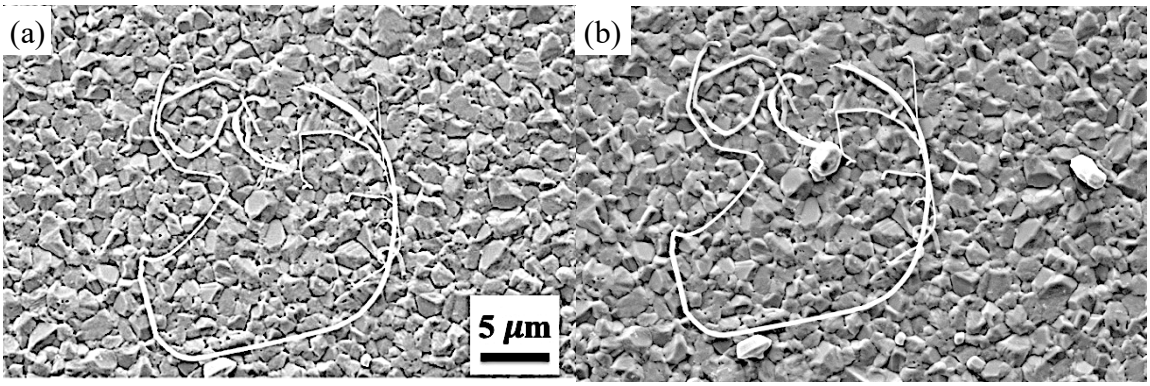


Figure 3.12. SEM images show a cluster of NWs with similar curvature in a local area. (a) after 4M cycles; (b) the same area after 5M cycles. Only new micro-sized surface defects nucleate.

Complicated morphology at the NW tip is seen for some NWs, as shown clearly in Figure 3.11 (e) and Figure 3.13. This corresponds to the initial nucleation and growth period based on the commonly accepted growth theory for whiskers from the base to the tip [60]. This reflects the competition and coupling of multiple processes that contribute to the nucleation of NWs, including but not limited to breakup of oxide layer, non-uniform mass transport rate at NW root and the sliding friction of GB influenced by the GB structure and crystallographic misorientation between two neighboring grains at the local sites [30]. Striations parallel to the growth direction are also observed on NW side surface.

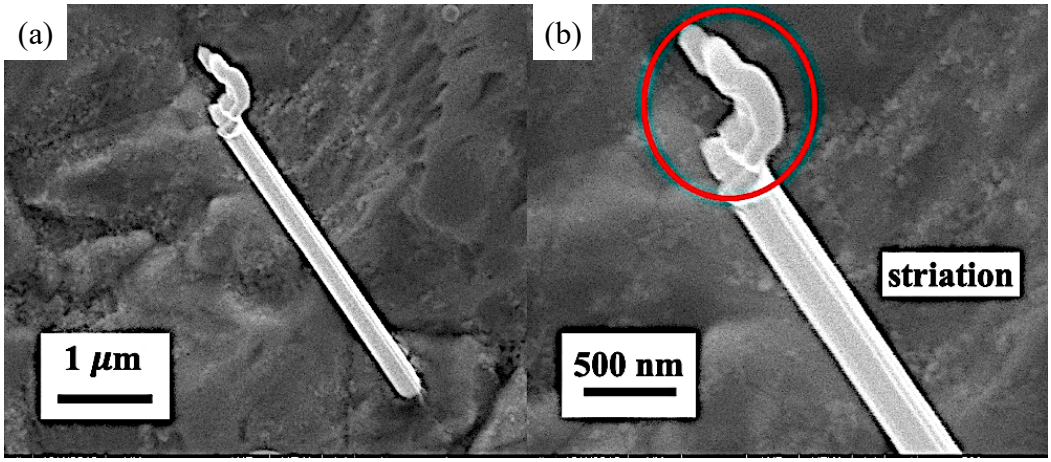


Figure 3.13. (a) SEM image of a NW; (b) enlarged SEM image of the top region of the NW. The circled area is the complicated morphology at the tip.

Some straight NWs not only become longer due to growth process but also evolve into curved NWs with additional cycling (Figure3.12 and Figure 3.14). The preferred sites for NWs are positions with the largest displacement during cyclic bending corresponding to the highest acceleration, thus there should be more curved NWs approaching the free end of the cantilever which is not the actual case. It is due to the fact that the resonant frequency for a NW may not be the same as the resonant frequency for cycling. The more complicated acceleration distribution for NW formation leads to a lack of relationship between the position and NW curvature. A detailed examination at the root of the NWs (Figure 3.14 (e)) shows that NW may originate from the extrusions of IGB besides GBs. Multiple NWs can be originated from extrusions of the same IGB (Figure 3-14 (e)), indicating local preferred nucleation sites for NWs surrounding the IGB area.

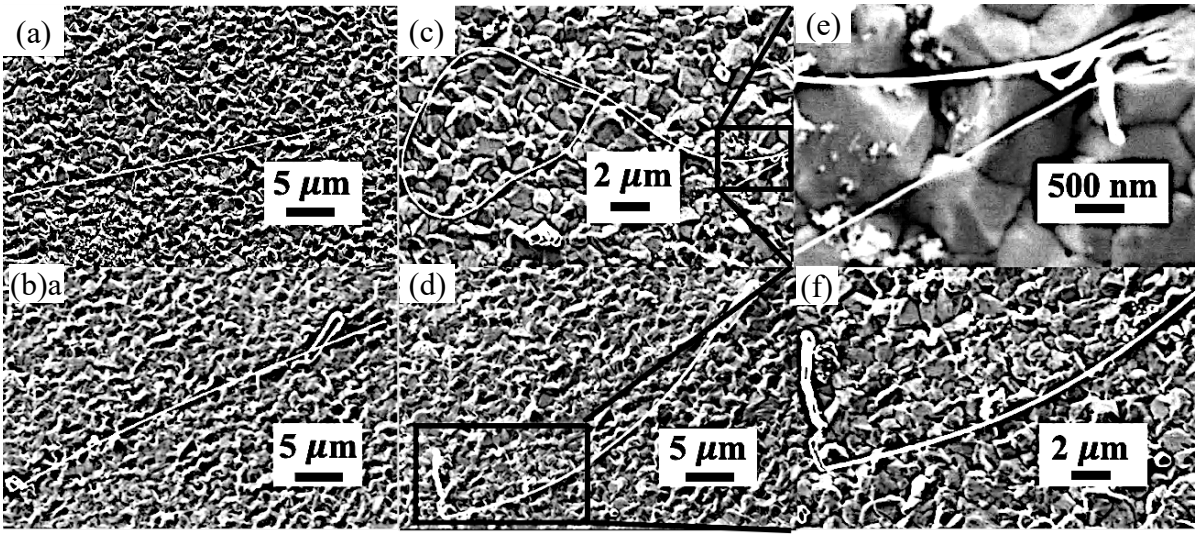


Figure 3.14. SEM images show evolution of straight NWs into curved longer NWs. (a), (b) after 7.5M cycles; (c), (d) the same area of fig. (a), (b) after 14M cycles; (e), (f) enlarged image of the NW root as marked in the rectangular region in fig. (c) and (d), respectively

As mentioned earlier, the GB geometry is very important for surface defect formation [12,16,34], and the GB geometry beneath the micro-sized surface defect and NW is shown in Figure 3.15. The FIB cut was defined as “1” and “2” for the NW and micro-sized surface defect root, respectively. The GB where NW nucleates shows nothing special than the GB of neighboring grains with a straight GB from a columnar grain. There is no significant accumulation of IMC at the GB (Figure 3.15 (b)) as seen for the micro-sized surface defect (Figure 3.15 (d)). It is hypothesized that NW nucleation is not dominated by the stress generated through IMC formation.

There are oblique GBs beneath the micro-sized surface defect (Figure 3.15 (c) and (d)). It is similar to the preferred GB geometry for surface defects in other conditions, and it indicates that the underlying mechanism and mass transport for micro-sized surface defects is the same despite the accelerating high cyclic frequencies and linear strain amplitude distribution along the cantilever.

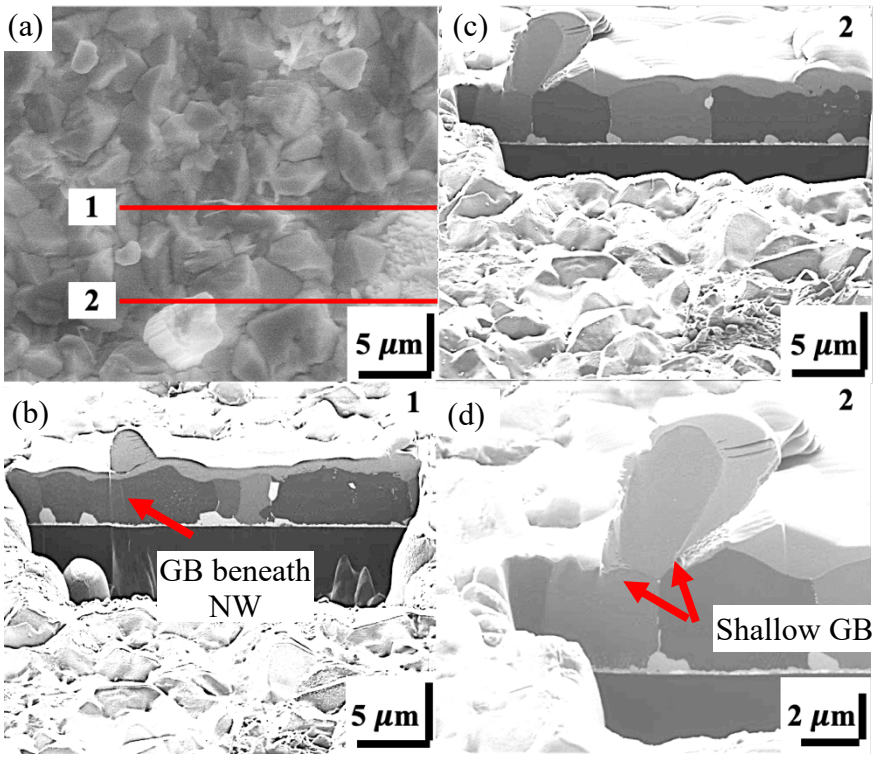


Figure 3.15. (a) the top-view SEM image; (b), (c), (d) the cross-section SEM image taken at 52° of tin films after cyclic bending; (b) the straight GB geometry below the NW (cut "1" in fig. (a)) ; (c), (d) the shallow GB geometry below the micro-sized surface defect (cut "2" in fig. (a))

In additional to micro-sized surface defects and NWs, IGB shows up as another stress relaxation mechanism, as seen clearly in Figure 3.16. The origin of IGB is from GBs, and the part above the grain surface for IGBs shows outward extension of pointed regions. As shown in the very right side of Figure 3.16 (c), the diameter of some extrusions is in nm range, the same magnitude of the diameter of NWs. This is hypothesized to be the initial growth period of NW that originates from IGB, and it is expected that there is continue growth of these extrusions to length of several micrometers as a NW growth, similar to what has been observed in Figure 3.14 (c).The pre-existing surface defects in the area where IGB evolves does not show any morphological changes during cycling (compared Figure 3.16 (a) and (b), (d) and (e), respectively). The IGBs

also do not exhibit any morphology changes after its first appearance depending on the local stress state and orientation.

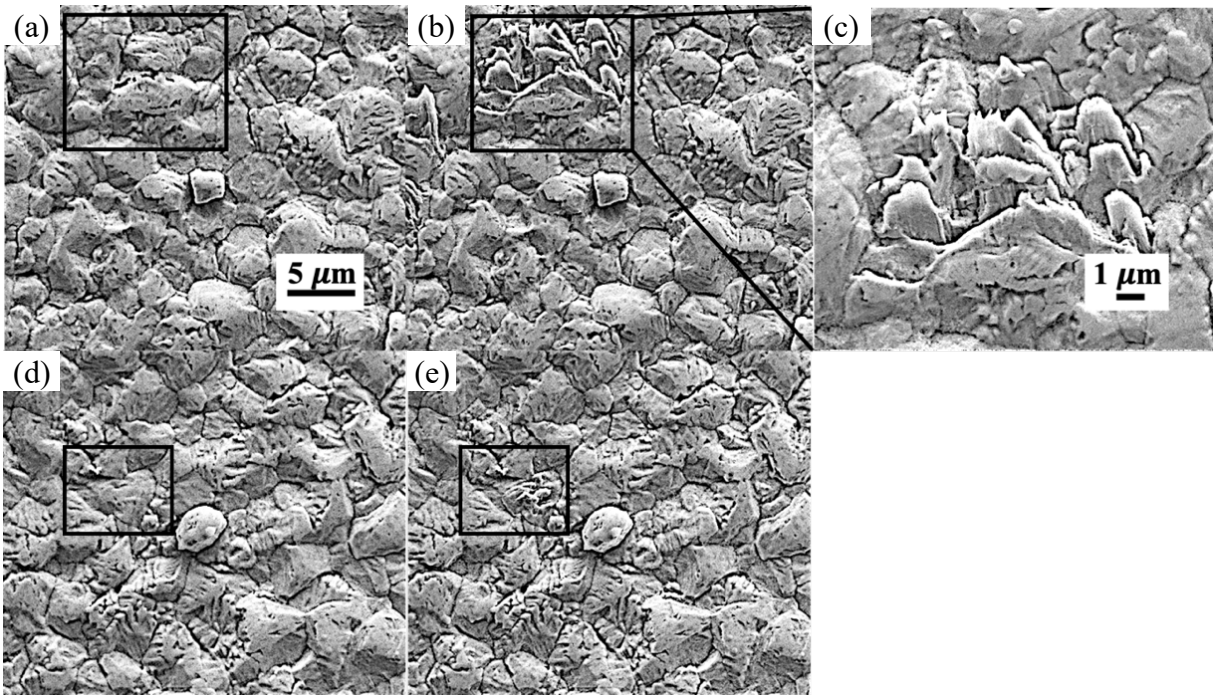


Figure 3.16. SEM images show nucleation of an IGB during cyclic bending. (a), (d) after 4M cycles; (b), (e) after 5M cycles; (c) enlarged SEM image of the rectangular area marked in fig. (b)

Some IGBs show morphology evolution for additional cycles corresponding to the local stress state, as exhibited in Figure 3.17. A new IGB (marked as "1" in Figure 3.17 (a) and (b)) with parallel extrusions propagates from the GB adjacent to a pre-existing short NW and a pre-existing IGB in the local area. There are detached and open regions in the GB initially (Figure 3.17 (a)), and it is hypothesized to be the nucleation site for the new IGB. The pre-existing IGB (marked as "2" in Figure 3.17 (a) and (b)) also evolves with more extrusions after additional cycles. For IGBs with initial complicated morphologies (Figure 3.17 (c) and (e)), morphology evolution reflecting more severe damage with additional number of cycles can be observed (Figure 3.17 (d) and (f)). The striations along the edge of the IGB (Figure 3.17 (b)) relate to cyclic numbers and they remain the same GB as the surface grain beneath it. It indicates that this was a micro-sized surface defect before IGB formation with growth for additional cycles (Figure 3.17 (d)). It indicates that there exists initial overall lift-up of the whole grain as a micro-sized surface defect before IGB formation.

Combined with the analysis for Figure 3.16, the IGB can be evolved from both in-plane grains or micro-sized surface defects.

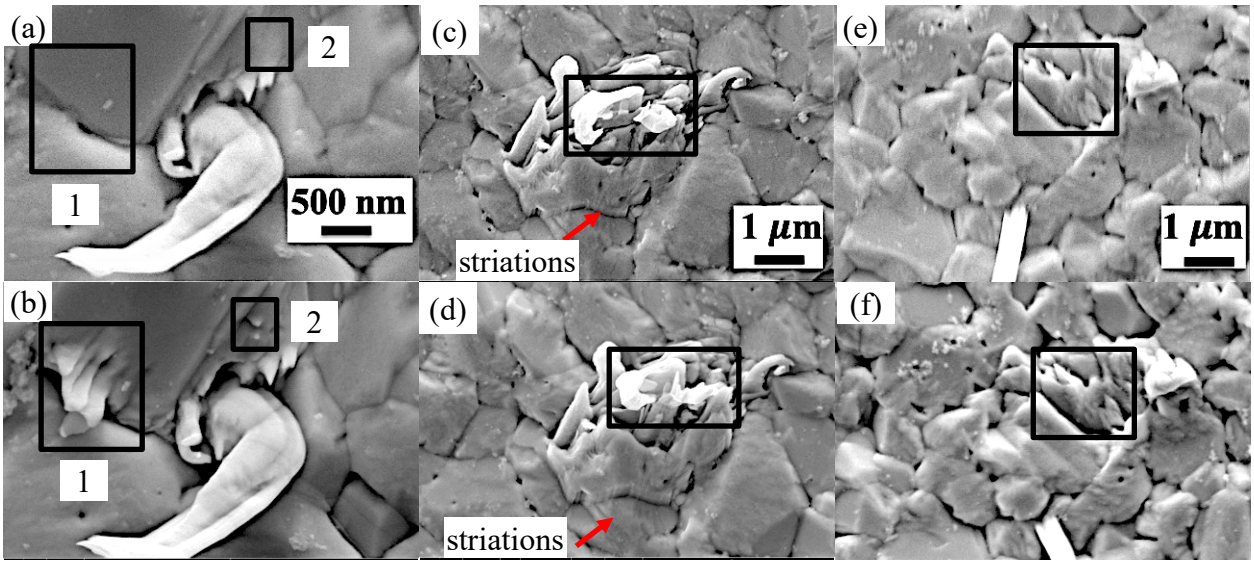


Figure 3.17. SEM images show evolution of IGB. (a), (c), (e) after 4M cycles; (b), (d), (f) the same area of fig. (a), (c), (e) after 5M cycles. The marked areas show the evolution of IGB extrusions.

The parallel hollow parts beneath IGB and the extrusions above the film surface shows open features from GB (Figure 3.18 (b)), which provides the underlying morphologies related to diffusion. It relates to the exfoliation from surface grains due to the initial material transport out of the film surface by climb motion of screw dislocations. The density of IGBs in a local area is much lower than that of NWs and micro-sized surface defects. IGBs are not major surface defect types compared to other defects during cyclic bending experiment at RT for the frequency range of about 400 Hz to 600 Hz that is studied in this research.

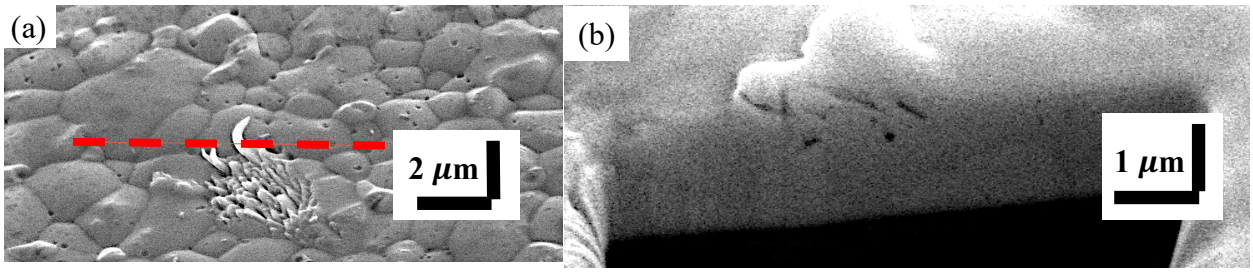


Figure 3.18. (a) SEM image shows the IGB surface morphology; (b) SEM image taken at 52° shows cross-section morphology of parallel hollow parts beneath IGB

### 3.3.2 **Quantitative Analysis of Defect Density on Tin Films**

To investigate the relationship between the strain distribution along the cantilever and the defect density for all the surface defects, a resonant frequency of 599.38 Hz was selected to vibrate the cantilever at first mode vibration for increasing number of cycles (Figure 3.19). The cantilever was vibrated in the interrupted mode with several intervals at 2.16M cycles, 3.24M cycles, etc. until the ultimate cyclic number of 14M cycles. To clarify, all the surface defects include micro-sized surface defects, NWs and IGBs. The surface defect density before cyclic bending is really low, and it is consistent with what has been observed in Figure 3.3 (a). After cyclic bending, large number of surface defects show up. The defect density always increases with increasing strain amplitude along the cantilever for fixed frequency and number of cycles, and the maximum defect density shows up at positions around the fixed end of the cantilever. It indicates that strain amplitude is the dominated factor to determine surface defect density for a designated frequency. Since strain rate is the product of strain amplitude and resonant frequency, the higher strain amplitude corresponds to higher strain rate for fixed resonant frequency. Thus, both higher strain amplitude and strain rate promote surface defect formation for fixed frequency.

The dramatic drop of surface defect density near the fixed end of cantilever is due to the geometry of the cantilever as shown in the inset of Figure 3.19. The arc-shaped shoulders at the fixed end can effectively avoid the stress concentration and is favored for the fabrication process. This design can cause the deviation from the perfect linear strain amplitude distribution along the cantilever for the first mode vibration even with minor differences of the shoulder shape.

As shown in Eq. 3-1, there is a relationship between resonant frequency and weight attachment at the free end of the cantilever for the first mode vibration. The heavier weight attachment leads to a lower resonant frequency and a larger tip displacement. This larger tip displacement corresponds to a strain distribution along the cantilever with larger maximum strain amplitude and slope as shown in Eq. 2-3. By converting the tip displacement into maximum strain amplitude (Eq. 2-3), the relationship between maximum strain amplitude at the fixed end and resonant frequencies can be obtained. To extract this relationship, four sets of tip displacement and corresponding resonant frequencies were measured directly from LDV system with various mass attached to the free end of the cantilever, as shown in Figure 3.20. It shows a linear relationship as predicted by Eq. 3-1 and Eq. 2-3. It can also be regarded as a prediction for cantilever vibration at other frequencies besides the four frequencies shown here. The comparison between the measured

displacement and the displacement speculated from Figure 3.20 can help double check the reliability of the experiment results.

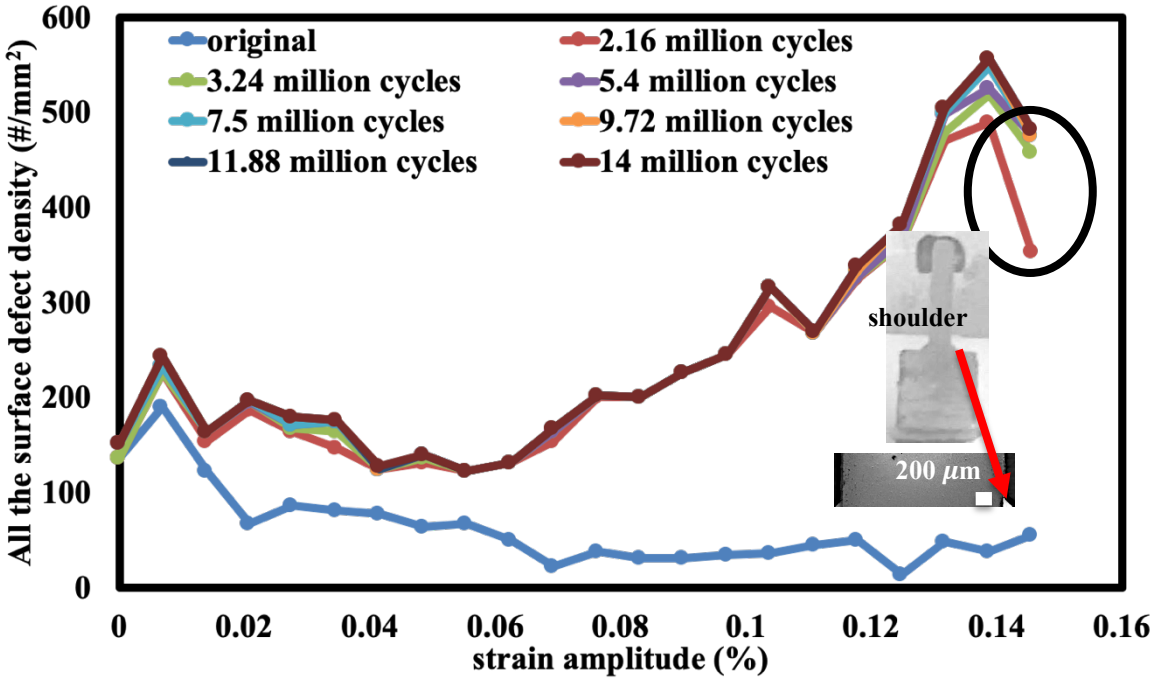


Figure 3.19. The density for all the surface defects along the cantilever at frequency of 599.38 Hz. The inset image shows the shoulder structure approaching the fixed end of the cantilever.

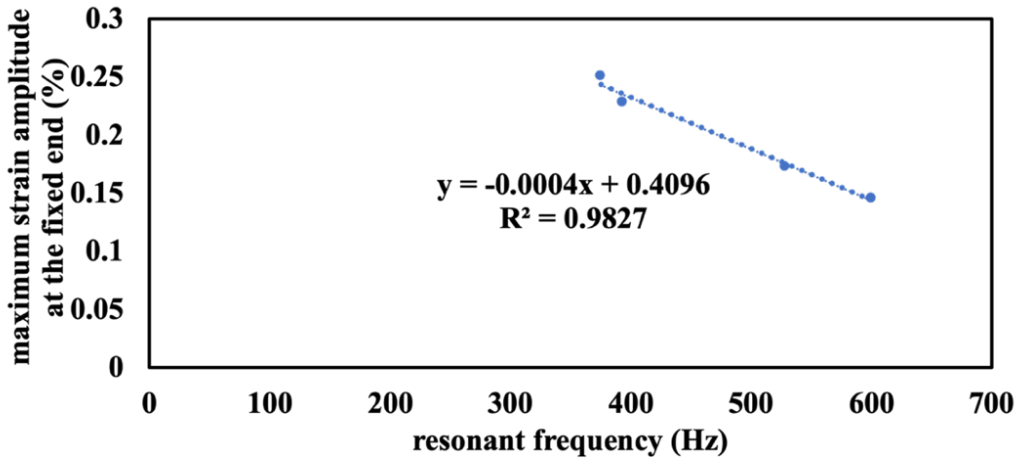


Figure 3.20. Plot shows linear relationship between the calculated maximum strain amplitude at the fixed end of the cantilever and the measured resonant frequency

To distinguish the influence of strain amplitude and strain rate on surface defect formation for different frequencies, another set of data were obtained with the interruptions at the same number of cycles for a frequency of 392.5 Hz in additional to 599.38 Hz. During cyclic bending, the difference between the slope of strain amplitude for these two frequencies is significantly large while the two frequencies exhibit similar strain rate distribution, as shown in Figure 3.21 (a) and (b) respectively. Strain rate is the product of strain amplitude and resonant frequency, thus the larger strain amplitude and corresponding smaller frequency (Figure 3.19) makes up for each other, and the comprehensive effects of these two factors lead to the similar slope of strain rate for these two frequencies.

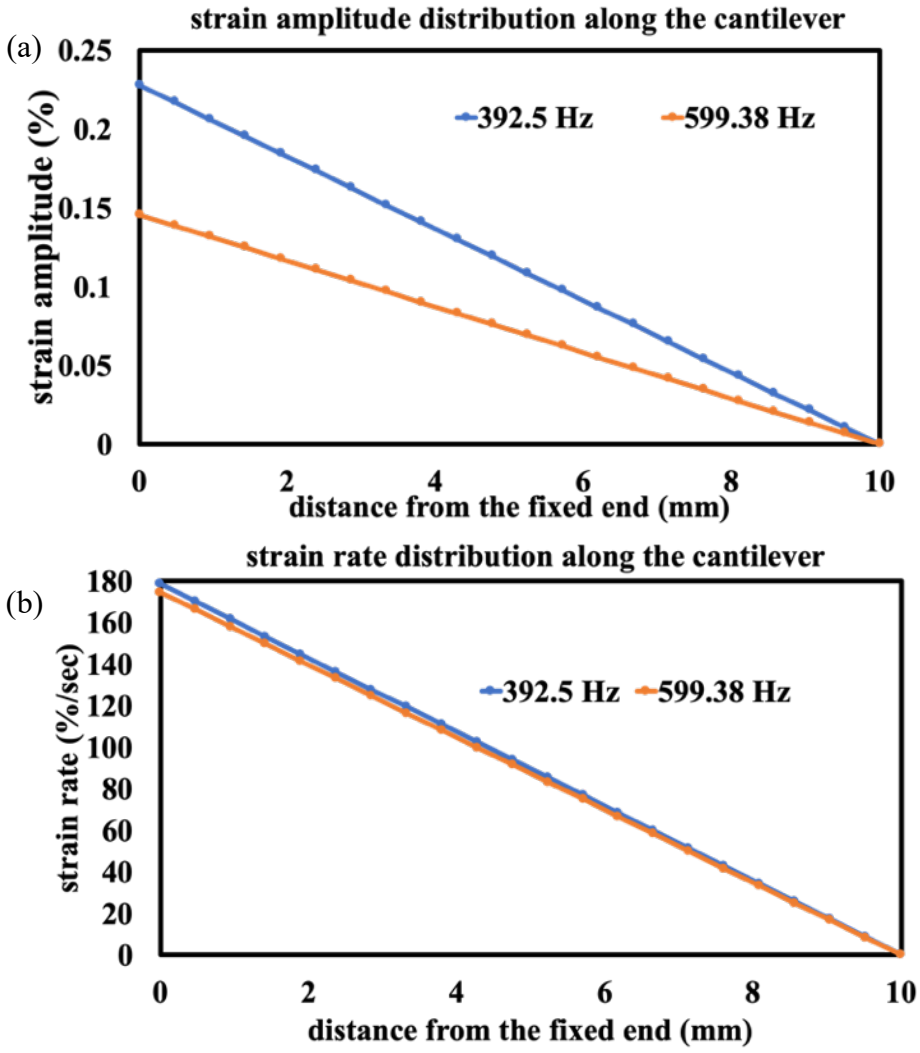


Figure 3.21. Strain amplitude (a) and strain rate (b) distribution along the cantilever for two different frequencies of 392.5 Hz and 599.38 Hz

Figure 3.22 shows all the defect density for these two frequencies at the same intervals, namely, 2.16M cycles, 3.24 M cycles and 5.4M cycles. The increasing defect density with increasing strain amplitude for 392.5 Hz is in consistent with that for 599.38 Hz (Figure 3.19). For the same strain amplitude distribution along the cantilever (Figure 3.22 (a)), there are always more surface defects for higher resonant frequency. Higher frequency corresponds to higher strain rate for the same strain amplitude, thus higher strain rate also promotes defect formation.

The same set of data was used with strain rate as the parameters on x axis shown in Figure 3.22 (b). For fixed strain rate, higher frequency corresponds to lower strain amplitude. Thus, the defect density is still larger for higher frequency with lower strain amplitude for fixed strain rate along the cantilever. It indicates that no matter how the slope of strain amplitude/rate varies along the cantilever, the resonant frequency is always the determining factor that influences the defect density. The density difference between these two frequencies becomes larger towards the fixed end of the cantilever, indicating the effect of resonant frequency on defect formation becomes more significant with larger strain amplitude/rate.

Figure 3.23 (a) and (b) shows the density for NWs as a function of strain amplitude and strain rate, respectively. The tendency is similar as that for all the surface defects with more deviations along the cantilever. The deviations correspond to the fact that the origin of NWs is a local response to stress greatly influenced by local grain orientation due to limited nucleation area. The uncertainty of the local grain orientation contributes to the response of NW density deviating from the perfect linear relationship with strain amplitude. NW density increases with larger strain amplitude approaching the fixed end for a particular resonant frequency, and the density is also frequency dependent for cyclic bending at different frequencies.

With a closer examination for the density increase after the initial interruption for both all the surface defects and NWs (Figure 3.21 and Figure 3.22), it can be concluded that the interrupted cyclic bending has a significant effect for the following evolution of defect density. The density increase is almost negligible no matter what the defect type is. To establish the hypothesis for this phenomenon with the consideration of fatigue accumulation and creep process, a similar set of experiment focusing on “continuous cyclic bending” to the same number of cycles for designated frequencies should be done. There is a critical strain amplitude for NW formation at lower frequency case that is not applicable for high frequency case. It indicates that the threshold for

nucleation of NWs is easier to achieve for higher frequencies. The density of IGBs for both frequencies is quite low, thus the quantitative analysis is not done for cyclic bending at RT.

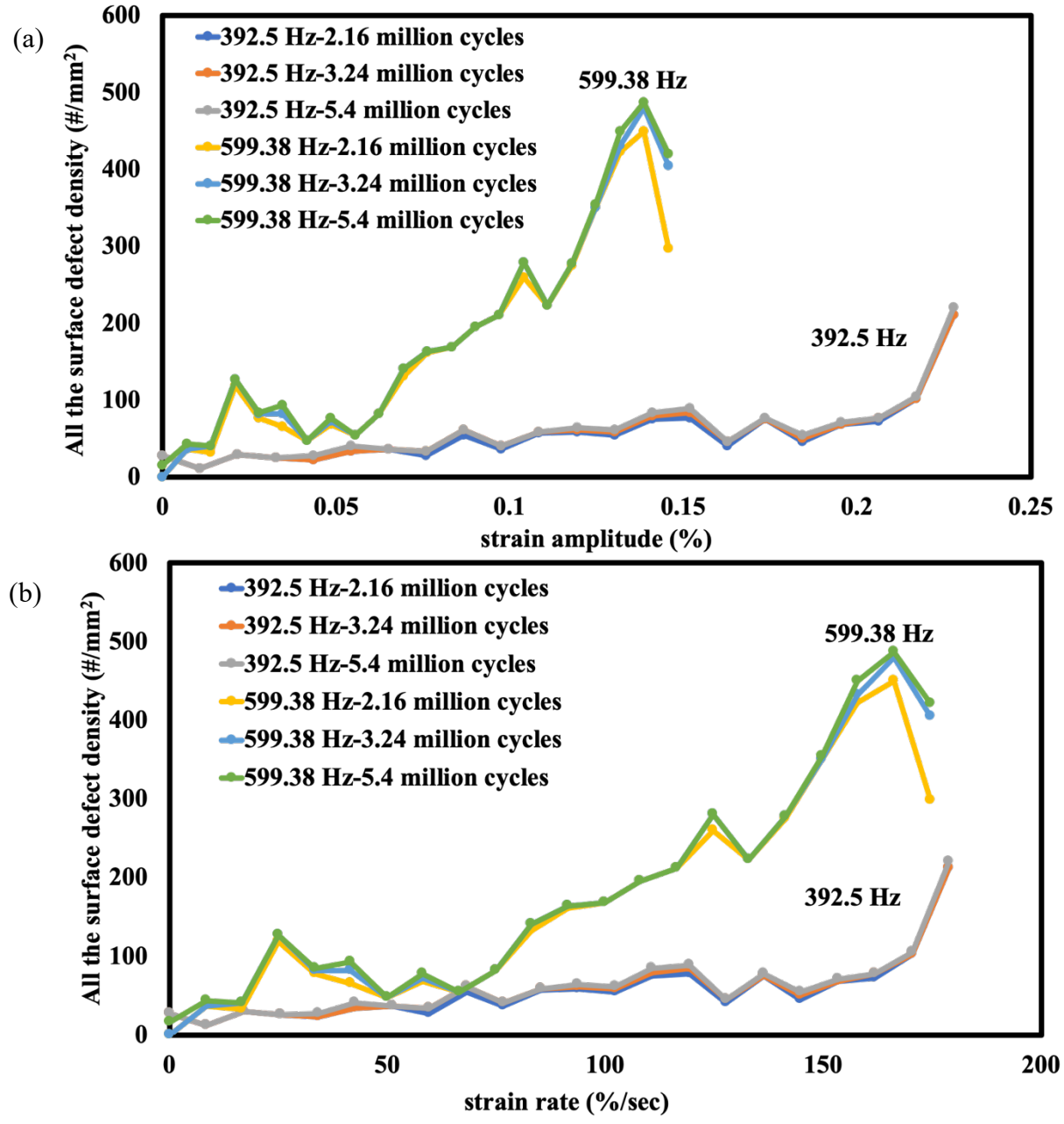


Figure 3.22. All the surface defect density along the cantilever (exhibited as variables of strain amplitude (a)/strain rate (b)) for two different resonant frequencies of 392.5 Hz and 599.38 Hz

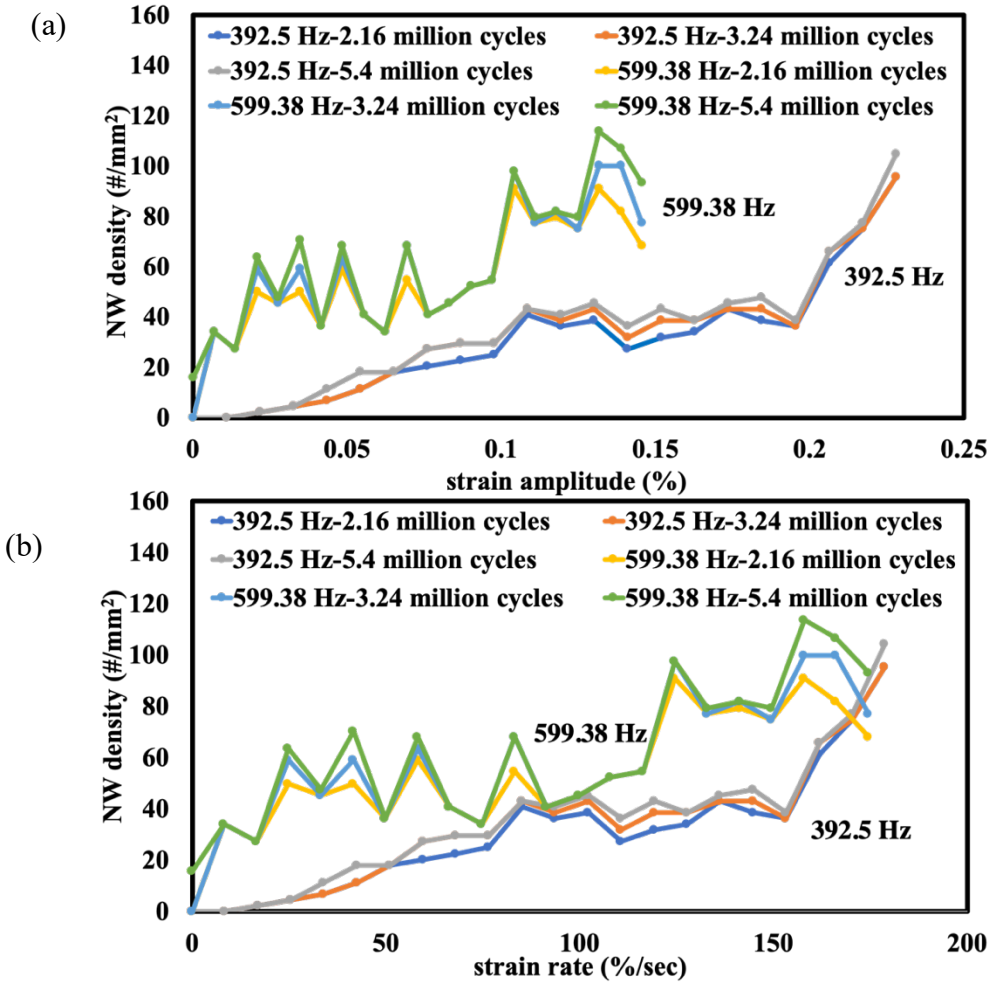


Figure 3.23. NW density along the cantilever (exhibited as variables of strain amplitude (a)/strain rate(b)) for two different resonant frequencies of 392.5 Hz and 599.38 Hz

To distinguish the evolution of different defect types with interruptions, the density of larger surface defects excluding NWs is shown clearly in Figure 3.24. This data is obtained by deduction of NW density (Figure 3.23) from all the defect density (Figure 3.22). The density remains unchangeable or shows minor changes after the first interruption, and this tendency is more obvious for the low frequency case of 392.5 Hz. The formation of NWs is the main stress relaxation mechanism for additional cycles during interrupted cyclic bending. The different size and nucleation site for NWs and micro-sized surface defects pose effect on the critical driving force for defect formation and diffusion process during the quick shift between tension and compression stress during cyclic bending. The detailed analysis will be talked about in the discussion part.

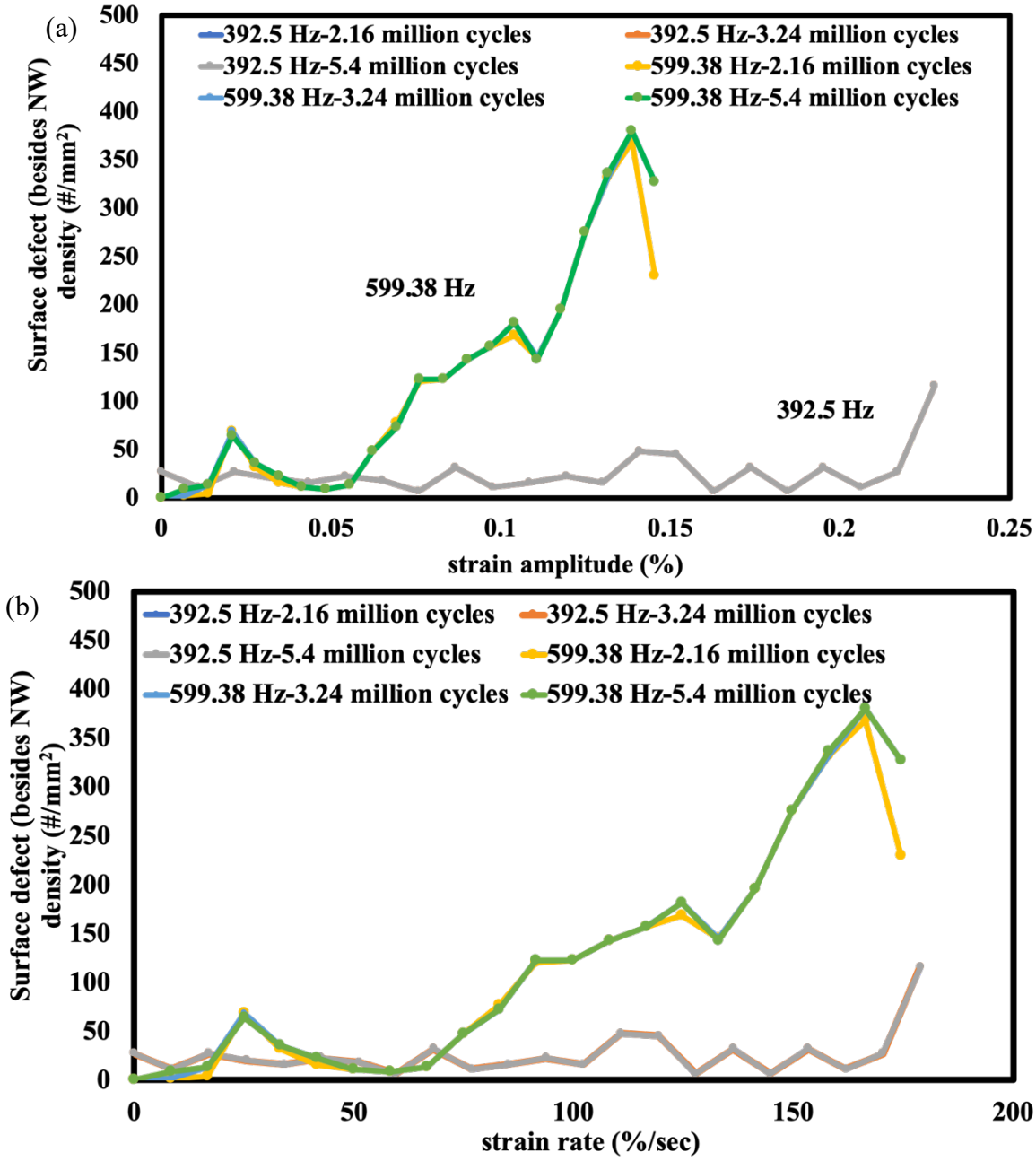


Figure 3.24. Density of larger surface defects excluding NWs along the cantilever (exhibited as variables of strain amplitude (a)/strain rate(b)) for two different resonant frequencies of 392.5 Hz and 599.38 Hz

Though the defect density/area for these two frequencies is smaller compared to that for cyclic bending of AFM cantilevers (Figure 2.11), the defect density/1,000 grains for defects in $\mu$m range is calculated about 4.5/1,000 grains and 2/1,000 grains for 599.38 Hz and 392.5 Hz, respectively as shown in Figure 3.24. It is higher or the almost the same compared to that even for

first mode cyclic bending of AFM cantilever with a value of 2.2/1000 grains. Given that the growth length and basal area of the surface defects evolved for cyclic bending of large cantilevers is larger than that for AFM cantilevers, the total volume of surface defects should be larger than that for cyclic bending of AFM cantilevers. It leads to obvious decrease of film thickness after the cyclic bending experiment, indicating significant mass transport and diffusion to sustain defect formation and growth. It is contrast to the results obtained for cyclic bending of AFM cantilevers with only a few nucleations of defects and corresponding limited diffusion.

### 3.3.3 **Discussion**

Cyclic bending experiment is a high-throughput technology including the rapid switch between tension and compression stress. This adds additional source of compressive stress by mechanical force compared to tin films during room aging [9,12–14], and it also significantly enhances the frequency of the tension-compression switch as compared to that for previous thermal cycling experiment [23,35]. It leads to the accelerating and magnifying of all the factors that contribute to the formation of micro-sized surface defects, the most common defect morphologies under other conditions. It also evokes new mechanisms or coupling between different mechanisms that lead to the formation of new features, shown as NWs and IGBs in this research.

The failure of materials is resulted from both fatigue damage and creep rupture damage [67], and the critical condition for failure is the overall damage accumulation exceeds some material dependent value. Though the failure life of tin films is not the topic emphasized in this research, these two types of damage exist simultaneously that contribute to defect formation on tin films. Fatigue damage relates to the accumulation of stress both globally and locally acting as the driving force for defect formation, while the creep process helps explain the limited nucleation of new surface defects after the initial interruption that will be talked about in Chapter 4.

Defect growth is a result from coupling between creep and dislocation glide [12] with simultaneous occurrence of stress generation and stress relaxation [24]. Therefore, two kinetic processes of stress generation and stress relaxation and their coupling by irreversible processes should be taken into consideration in explaining the mechanism for surface defect formation. The origins of the compressive stress acting as the driving force in the cyclic bending experiment of this research are mainly in three categories. One is the plating stress that cannot be recovered once being relaxed, one is the finite mechanical force generated in each cycle, and the third is originated

from IMC formation at the interface between Cu layer and tin films. Defect growth occurs by the removal of atomic layers of Sn normal to the stress direction, and these Sn atoms can diffuse along GBs to the root of a stress-free whisker to sustain its growth. This is achieved by mass diffusion from tin films into the defect region. The final stress accumulation is the coupling between stress accumulation and relaxation. Defect growth is just one approach of stress relaxation mechanisms, other responses like GB sliding and cracking can also happen simultaneously during cyclic bending. Both the multiple stress relaxation responses of tin films as well as the various factors that influence the defect formation, including but not limited to global and local grain orientations and GB geometry, increase the difficulty to predict the locations and probability for each type of surface defects. Combined with effect EBSD data and multiple cross-section analysis for surface grains, the above quantitative analysis can shed some light on the stress situation that application of tin films should be avoided.

One hypothesis for the unique morphologies of NWs and IGBs only shown for cyclic bending of tin films compared to cyclic bending of other materials systems is due to the high homologous temperature effect of Sn at RT compared to other materials. Table 3.1 summarizes the homologous temperatures for Cu, Al, Ag and Sn at RT with an assumption of RT to be 298 K. The homologous temperature for Sn is much higher than that for the other three metals. It even exceeds the ratio of maximum operating temperature to melting temperature for Cu, and it indicates that there is no overlapping homologous temperature range that can achieve both Cu and Sn in proper operation. The average value of homologous temperatures for Cu, Al and Ag at RT is 0.26. If this value is taken to achieve a similar homologous temperature for Sn, the corresponding temperature is about 131 K. It is far below RT with a ratio of 0.45 over RT. The high homologous temperature of tin at RT favors diffusion along GB [8,21], and it leads to the obvious Coble creep behavior of Sn as stress relaxation mechanisms at RT. The Coble creep of Sn is postulated to distinguish the behavior of Sn from other three metals during cyclic bending.

Another consideration distinguishing Sn from other materials systems is the crystal structure difference. Compared to only 12 dominated slip systems for FCC structure (Cu, Al and Ag), the corresponding 32 slip systems for BCT structure of Sn [6] lead to more complicated elasticity and plasticity anisotropy during the cyclic bending. This is also hypothesized to play a role in determining the defect type of tin films.

Table 3.1. Homologous temperatures for different materials systems at RT (RT~298K)

| Materials | Melting temperature T1(K) | Homologous temperature | Maximum operating temperature T2(K) | T2/T1 |
|---|---|---|---|---|
| Cu | 1356 | 0.22 | 533 | 0.39 |
| Al | 932 | 0.32 | 733 | 0.79 |
| Ag | 1224 | 0.24 | / | / |
| Sn | 505 | 0.58 | / | / |

Inhomogeneous deformation caused by stress generation in cyclic bending leads to the multiplication and conservative motion of dislocations through the whole surface [68]. Surface defect formation is a stress relaxation mechanism that facilitates the release of strain energy caused by dislocation pile-up approaching GBs. The dislocations concentrating localized around the ends of slip bands at GBs consist of both screw and edge dislocations due to the various directions of slip bands. The motion of screw dislocations promotes trapping of Sn atoms and their aggregates migrating on Sn surface, and it acts as a preferred nucleation site for defects. The nucleation for defects is achieved by cracking of the oxide layer on the film surface. Once concentrated stress exceeds some critical value, defects pop-up through "weak spots" in the oxide layer requiring smaller compressive stress as driving force compared to other sites on the film surface. The diameter and morphology of defects is confined by the size and stress distribution of these "weak spots" [21]. The pipe diffusion of Sn atoms along edge dislocations facilitates the mass transport from bulk Sn into all the surface defects to sustain defect growth.

The mechanism that leads to NW formation by cyclic bending is related to the nucleation of new grains since it has a diameter in nanometer range that is much smaller than that of the in-plane pre-existing grains of the film with a grain size from 2-5 $\mu$m. This distinguishes from micro-sized surface defect formation due to IMC that originating both from pre-existing in-plane grains and nucleated new grains through recrystallization for room aging [17,69]. IMC-induced surface defects grow via Coble creep to inclined GBs at the base of defect surface grain with the overall rise of the whole in-plane grain [12,13,19,34]. The nucleation of NWs requires less energy and experiences smaller barrier compared to that for normal micro-sized surface defects, and it relates to their smaller volume and nucleation site.

Nucleation of NWs relates to local dislocation accumulation approaching GBs or extrusion parts of IGBs, and it is similar to the dislocation accumulation mechanism happening at the specific

inclined GB mentioned for micro-sized defects [68]. The GB is defined as the boundary with greater than 15 degrees of misorientation between two neighboring grains, and there also exists misorientation issue for IGBs due to its complicated morphology. Disordered atoms with multiple pre-existing dislocations are present approaching GBs and IGBs due to the lattice transition and coordination, and it is a preferred site for NW nucleation with this dislocation concentration. The locations of NWs are determined by the local GB geometry between two neighboring grains or the coupling between extrusion and intrusion parts of IGBs. It is assumed that there is small curvature at the GB where NW nucleates, as shown in Figure 3.25. To verify this geometry approaching the root of NW, cross-section analysis needs to be done. The geometry is not revealed in Figure 3.15 (b) due to the infinite limited area approaching the NW root and the lack of high magnification SEM image at the root with more precise FIB cut.

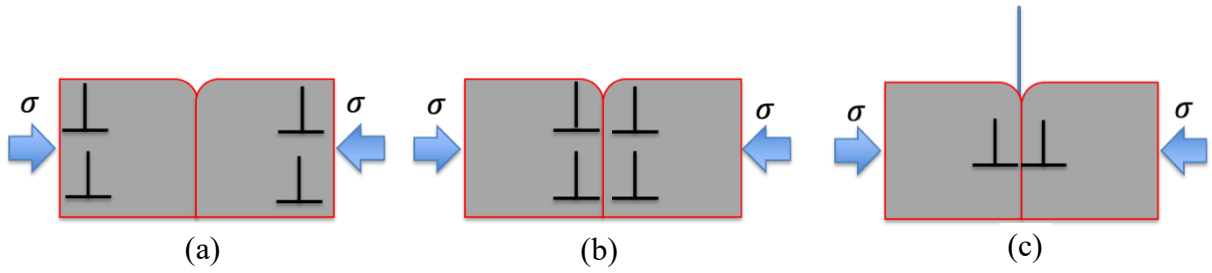


Figure 3.25. A series of schematics show NW formation due to the compressive stress during cyclic bending. (a) dislocation generation (the arrow indicates the stress direction); (b) movement of dislocations approaching the GB; (c) NW formation as a stress relaxation mechanism

The compressive stress acting as the driving force for surface defect formation is generated and accumulated during the compressive half cycle of the cyclic bending. Dislocation motion and multiplication through the deformation of tin films is driven by the compressive stress. Since the time for the presence of compressive stress in each cycle is very short due to the high frequency, the dislocations cannot “travel” far enough to the preferred oblique GB for micro-sized surface defects, and their activities are more localized at random GBs between two neighboring grains. Some of the micro-sized surface defect formation favored by long-range diffusion is substituted by NW formation favored by short-range diffusion for the present cyclic bending research. The short-range diffusion for NWs can be verified through the cross-section images of micro-sized surface defects and NWs (Figure 3.15). The IMC particles at the GBs can enhance the long-range diffusion of Sn atoms by applying compressive stress to the grains on both sides of the GB due to

the IMC growth [61]. Thus, it can be inferred that short-range diffusion is favorable for NW nucleation due to lack of IMC accumulation at the GBs beneath NWs. Since IMC formation is achieved by diffusion along GBs which can be facilitated by open area for IMC dwell caused by misorientation between neighboring grains [70], it can be concluded that the GB misorientation angle beneath micro-sized surface defects is larger than that beneath NWs due to the different IMC distribution for these two defects.

For IGB formation, it is hypothesized that several instead of one slip system activated due to the cyclic stress in the experiment. The prerequisite of oxide layer crack for defect formation is heavily influenced by the local grain orientation and stress state. It is almost impossible to develop and maintain one slip over continuously. Several slips happening in sequence due to the cyclic bending lead to the complex morphology of IGBs. As mentioned in Chapter 2, PSB with high localized cyclic slip activity can develop during cyclic bending. The formation of extrusions and intrusions are a result from dislocation motion through the encounter of PSB and film surface during coarse slip process [71,72], and this also facilitates the formation of IGBs.

As mention earlier, defect formation is always believed to be driven by diffusion [26,73] through mass transport. Based on the fact that diffusion rate is proportional to the concentration gradient driven by cyclic stress, larger strain amplitude promotes surface defect formation. The increasing density of dislocations is achieved by rapid multiplication due to higher strain rate. This leads to higher flow stress by promoting work hardening. With constant temperature, the relationship between flow stress $\sigma$ and strain rate $\dot{\varepsilon}$ is: $\sigma = C\dot{\varepsilon}^{m}$, where m is strain-rate sensitivity [74]. The value of m can be positive or negative depending on the material type. Though the exact value of m for Sn is unknown, it is expected to be positive with the tendency of higher surface defect density for higher strain rate at a designated frequency. Viscoplasticity is the mechanism supporting this positive value of m, and it is dominant at temperature greater than approximately one third of the absolute melting temperature. Since RT is about 0.58 of Sn melting temperature, viscoplasticity is the overwhelming behavior of tin films at RT that generate higher shear stress [75]. The higher strain amplitude also increases the plateau value of stress for typical stress-strain curves. It helps explain the phenomenon that there are more surface defects when approaching the fixed end of cantilever for a specific frequency.

The growth process for defect formation shown in Figure 3.26 can be used to help explain the frequency effect on defect formation for different frequencies. Before cyclic bending, a layer

of oxide layer present on the film surface, as shown clearly in Figure 3.26 (a) with the preferred shallow grain for defect nucleation. Surface defects grow during the compressive half cycle with the crack of oxide layer on film surface and the oxide layer is also formed quickly on defect surface once it nucleates (Figure 3.26 (b)). The oxide is a poor source and sink for vacancies, and the oxide ties down the lattice plane in Sn and prevent them from moving. During the tensile half cycle, the oxide layer is formed again on the surface and defects have the tendency to retract by breaking the oxide layer on its surface (Figure 3.26 (c)). Surface defects can grow again during the next compressive half cycle and repeated the above-mentioned "grow and retract" process for additional cycles (Figure 3.26 (d)). At higher frequencies, there is less time for the oxide to grow and rebuild on film surface as well as for newly formed whisker to overcome the oxide layer on its surface acting as a shell during the tensile half cycle. Thus, the thinner oxide layer that is easier to crack and increasing difficulty for defect retraction due to the oxide layer on defect surface promote the formation of all the surface defects.

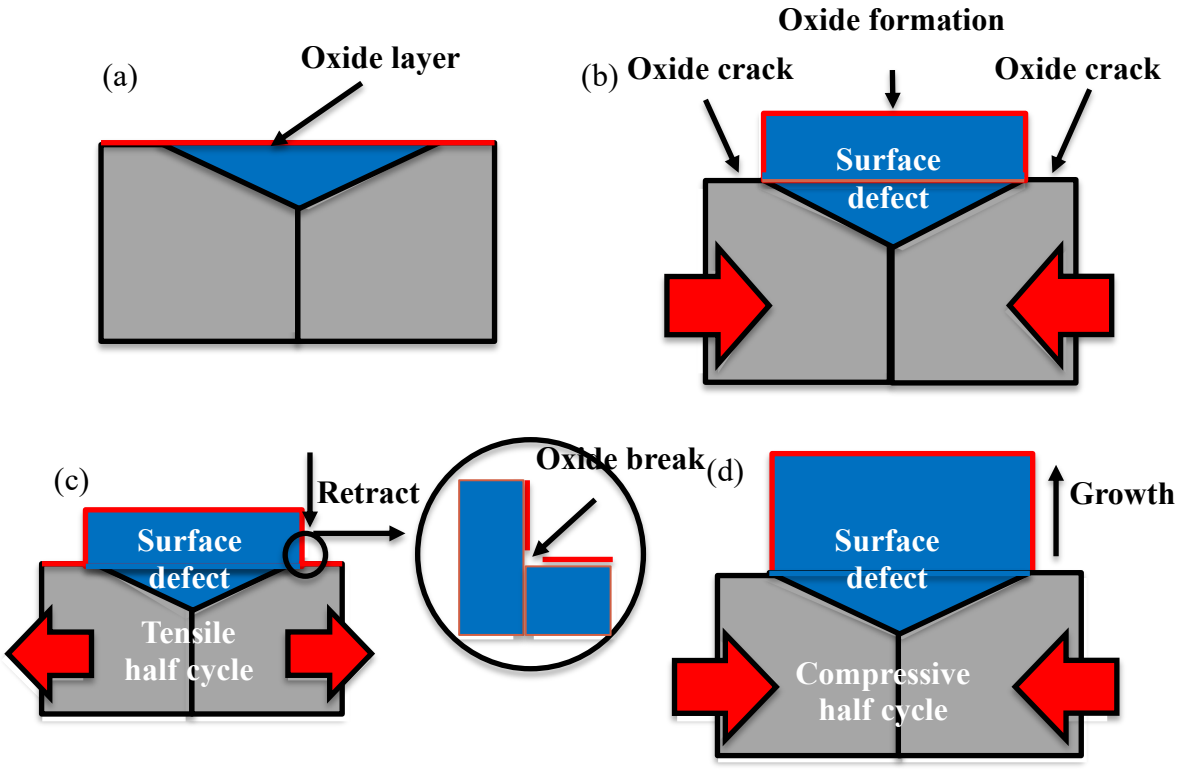


Figure 3.26. A series of schematics shows surface defect formation during cyclic bending. (a) film surface before cycling with oxide layer; (b) whisker growth during compressive half cycle (stress is shown by the red arrows); (c) defect retraction and oxide formation on film surface during tensile half cycle; (d) further whisker growth during the subsequent compressive half cycle

The experiment is done with several intervals during the cyclic bending process, and the major density increase is achieved at the first interruption. Defect density increase for additional cycles is negligible, and the majority of defects contribute to this limited density increase is NWs. For the evolution of surface defects before the first intermittent, though stress relaxation happens during the tensile half cycle, enough stress is generated from IMC growth and plating stress as well as the compressive half cycle. As a consequence, both long-range and short-range diffusion can happen simultaneously to promote the formation of all kinds of surface defects before the initial interruption. During the time interval between each interrupted cyclic bending, the stress can be fully relaxed. The compressive stress for the additional cyclic bending is only generated during compressive half cycles. The accumulated compressive stress is smaller than that before the first intervals, and it increases the difficulty to maintain long-range diffusion that is favored to sustain micro-sized surface defect formation. Short-range diffusion dominates, and it leads to more NW formation.

## 3.4 **Summary**

The behavior of tin films on large cantilevers in mm range during the interrupted cyclic bending was analyzed in detail in this chapter. Three kinds of defects show up from the film during cyclic bending, and the density and ratio of these surface defects are resulted from the coupling and competition between various mechanisms influenced by strain amplitude/rate, resonant frequency as well as number of cycles. The morphology evolution for different surface defects were followed by tracking the same area on the film surface with increasing number of cycles for several interruptions. GB geometry, local grain orientation and strrain gradient as well as mass transport all contribute to this morphology evolution. The hypothesis for all the tendencies as well as the mechanisms for defect formation were discussed with reference to the reported surface defect growth models. The major conclusions are as follows:

(1) Three kinds of surface defects show up for the cyclic bending of large cantilevers: nanowhiskers (NWs), intragranular breakup (IGB) and normal micro-sized surface defects. NWs with diameter in nm range and originating from GBs or extrusions of IGBs and micro-sized surface defects are the major defect types in this interrupted cyclic bending. There are also a few IGBs with complicated open morphologies including intrusions and extrusions. The morphology of NWs and IGBs are unique compared to

tin films using other conditions while NWs are even not observed for cyclic bending of other materials systems.

(2) For a particular frequency, the density for all the surface defects, NWs as well as larger surface defects excluding NWs increases with increasing strain amplitude/rate as well as number of cycles. The more deviations for NW distribution along the cantilever with strain amplitude is resulted from the random local grain orientations. The change of defect density after initial cycles is almost negligible for all kinds of defects no matter how many additional cycles are performed.

(3) After the initial interruptions, NWs contribute most in the following defect density increase for additional number of cycles with several interruptions due to the smaller energy barrier and nucleation site for NWs. The competition and coupling between short-range and long-range diffusion with stress accumulation process only happens during cycling while stress relaxation can happen even when the film is static helps explain the contribution of different surface defects for different stages.

(4) For cyclic bending at different frequencies, the surface defect formation is always frequency dependent. It indicates that there are always more surface defects at higher frequencies with the same strain amplitude/rate corresponding to different positions along the cantilever. It can be explained by the repeated break and formation of oxide layer on tin film surface as well as growth and recombination of surface defects during the compressive and tensile half cycle of the cyclic bending experiment, respectively.

# 4. CYCLIC BENDING OF LARGE CANTILEVERS IN MM RANGE FOR CONTINUOUS CYCLING

## 4.1 Motivation

Cyclic bending of large cantilevers for interrupted cyclic bending was done systematically in Chapter 3. The several interruptions make it possible to track the evolution of the same surface defect during the cyclic bending. The morphology and volume changes of the surface defects help greatly explain the mechanism for surface defect formation. The accompanying phenomenon with this method is the negligible surface defect formation after the initial interruption. Besides, there exists two obvious different stages for this interrupted cyclic bending: formation of all kinds of surface defects for the initial interruption with NW domination for the following several interruptions. It indicates that the interruption plays an important role in surface defect formation.

One effective way to verify the mechanisms that activate during the interrupted cyclic bending especially during the rest period between the interruptions is through the comparison between interrupted and continuous cyclic bending. To achieve this, two sets of experiment is done at the same resonant frequency. One sample is interrupted several times similar as described in Chapter 3 to the designated number of cycles, the other sample is cycled continuously for the same number of cycles. The quantitative results got for different kinds of defect density can shed some light on explaining the function of the interrupted cyclic bending.

## 4.2 Procedures

The fabrication and cyclic bending experiment are the same as described in detail for the interrupted cyclic bending in Chapter 3. Two samples with similar film surface morphology were used to do the cyclic bending with a fixed resonant frequency of about 600 Hz. One sample was interrupted several times to about 14M cycles while the other sample was just interrupted once at 7.5M cycles. The details about the cyclic bending of these two samples were shown in Table 4.1.

The same quantitative analysis method was used as mentioned in Chapter 3 with the SEM (Quanta 650, FEI). The number of all the surface defects, NWs as well as larger surface defects excluding NWs between interrupted and continuous cyclic bending was analyzed to reveal the mechanisms.

Table 4.1. Details for experiment between interrupted and continuous cyclic bending at 600 Hz

| Types of cyclic bending | Cyclic numbers for interruption |
|---|---|
| Interrupted | 2.16→3.24→5.4→7.5→9.8→11.9→14M cycles |
| Continuous | 7.5→14M |

## 4.3 Quantitative Analysis between Interrupted and Continuous Cyclic Bending

The defect morphologies are similar for the interrupted and continuous cyclic bending, and the evolution of defects also follow the same tendency as mention in Chapter 3. It is reasonable since the only variable is the period and numbers of interruptions.

The density of all the surface defects increases significantly for continuous cyclic bending as compared to that for corresponding interrupted cyclic bending at the same number of 7.5M cycles, as shown clearly in Figure 4.1. The ratio of the maximum defect density for these two situations is about 3, with the maximum defect density of 1200/mm$^2$ for continuous cyclic bending and 400/mm$^2$ for interrupted cyclic bending. This is almost the same as the ratio of the initial cycles, 7.5M/2.16M $\approx$ 3. It indicates that there is a linear relationship between all the surface defect density and number of cycles for continuous cyclic bending without interruptions. The defect density difference between 7.5M and 14M cycles for continuous cyclic bending is still limited even with another 6.5M cycles difference. This is almost 46.4 % of the total number of cycles (14M cycles), and it is many more than the number of cycles between interruptions selected in Chapter 3. This demonstrates that once the experiment is interrupted and the sample rests for some period of time, the surface defect density increase is negligible no matter how many additional cycles will be conducted on the samples.

There is no clear difference for NW density between interrupted and continuous cyclic bending with the quantitative analysis shown in Figure 4.2. It shows that the initial NW density after cyclic bending of 7.5M cycles for these two situations is similar with the maximum density of 140/mm$^2$. The final NW density for continuous cyclic bending at 14M cycles (about 170/mm$^2$) is a little higher than that for interrupted cyclic bending (about 150/mm$^2$) with several interruptions. It does not follow the same rule for all the surface defects that the density ratio is determined by the ratio of cyclic numbers. This indicates that the NW density is not much influenced or determined by how the experiment is carried out. The interruption does not play a dominated role in NW formation process.

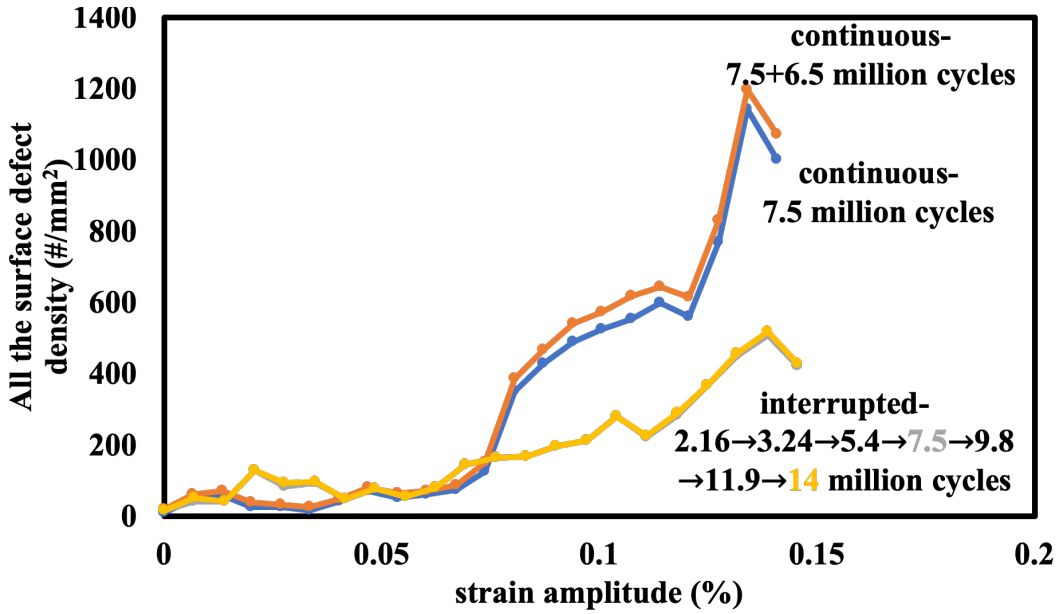


Figure 4.1. All the surface defect density along the cantilever (exhibited as strain amplitude) for interrupted and continuous cyclic bending at cyclic numbers of 7.5M and 14M cycles

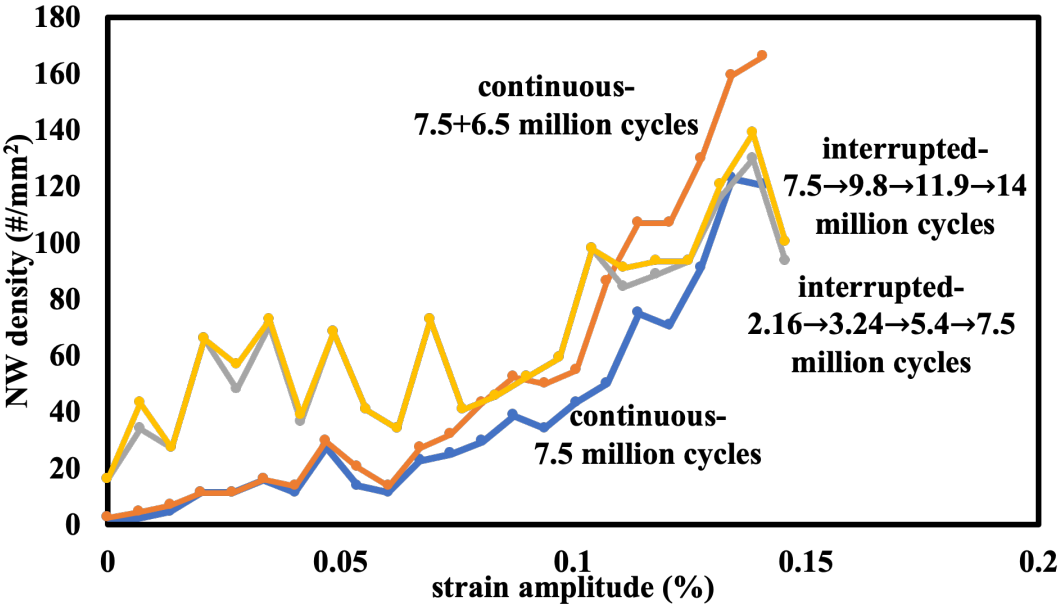


Figure 4.2. NW density along the cantilever (exhibited as strain amplitude) for interrupted and continuous cyclic bending at cyclic numbers of 7.5M and 14M cycles

Since the density of all the surface defects shows linear relationship with the initial number of cycles (Figure 4.1) and the density of NWs is independent of the number of cycles and the interruption process for cyclic bending (Figure 4.2), it is expected that the interruption has a great

effect on density of larger defects excluding NWs. This is verified with the quantitative analysis of defects besides NWs shown in Figure 4.3. The ratio of the maximum density of larger surface defects excluding NWs for the ultimate number of cycles (1080/380) is about the same for the ratio of initial cycles (7.5/2.16) between continuous and interrupted cyclic bending. The continuous cyclic bending greatly promotes micro-sized surface defect formation. The stress generated in each cycle and the stress accumulation during the whole process even with continuous stress relaxation determines the density of micro-sized surface defects.

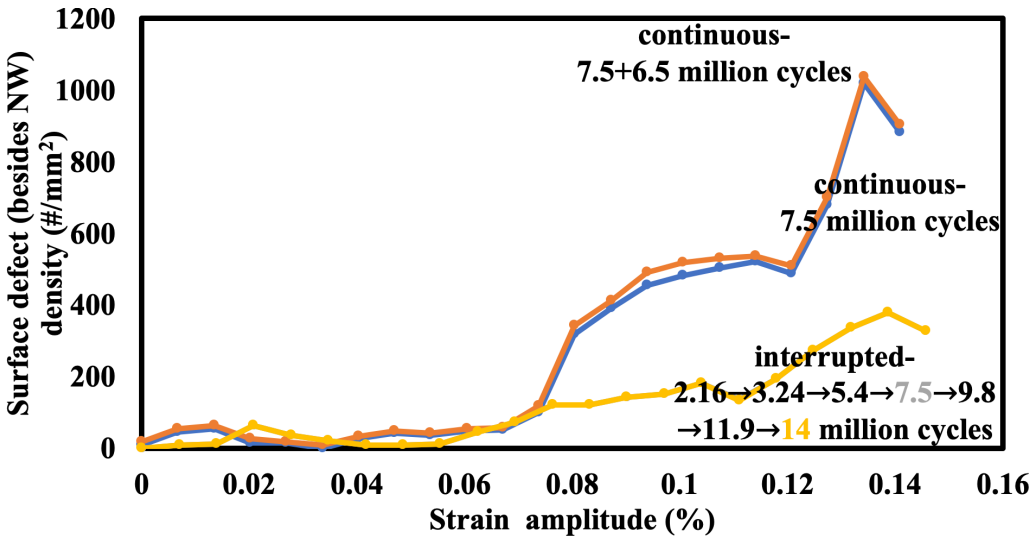


Figure 4.3. Density of larger surface defects excluding NWs along the cantilever (exhibited as strain amplitude) for interrupted and continuous cyclic bending at 7.5M and 14M cycles

There are similar tendencies for all kinds of surface defects along the cantilevers for both continuous and interrupted cyclic bending (Figure 3.22-Figure 3.24). The defect density increases from the free end to the fixed end of the cantilever with the maximum strain amplitude/rate for a particular frequency. The continuous cyclic bending does not change the influence of strain amplitude/rate on defect density during cyclic bending.

## 4.4 **Discussion**

The question needs to be answered now is why the interruptions greatly pose negative effect on micro-sized surface defect formation and does not influence NW formation in the same way for additional number of cycles.

Coble creep by GB diffusion and Nabarro-Herring creep by bulk diffusion are the major mechanisms of creep deformations that can happen in tin films during cyclic bending. The creep processes involve various dislocation interactions, including glide, climb and cross-slip, and the role of the dislocations in defect formation have been analyzed in detail in Chapter 3. Coble creep dominates for the cyclic bending due to the relative smaller barrier compared to that for Nabarro-Herring creep, and the typical creep curve of strain vs. time is usually divided into three stages. The strain rate increases rapidly for the primary and tertiary stages while it maintains a small strain rate for the secondary stage (as shown in Figure 4.4).

A previous research on the creep test of a sandwich structure composed of Fiber-Reinforced Plastic (FRP) faces and a Polyvinyl Chloride (PVC) foam core showed that the steady creep dominates the creep response [76]. Applying this hypothesis to the cyclic bending of tin films with the dominate Coble creep behavior of tin films mainly activating at the secondary stage with small steady strain rate helps build up a simple model to explain the few nucleation of surface defects for the interrupted cyclic bending.

When the film is under compressive stress, it breaks some spots of oxide layer on the top which act as "weak spots" to facilitate the nucleation of surface defects including micro-sized surface defects and NWs [32]. The nucleation is accompanied by the forward creep behavior through the primary and secondary stages (Figure 4.4 (a)) as a stress relaxation mechanism. The oxide layer can be formed again during the tensile half cycle with tensile stress and the rest period when the film is static between interruptions during cyclic bending. This corresponds to the reverse creep behavior in the secondary stage (Figure 4.4 (b)). The oxide layer can be very thick due to the sufficient time for oxide formation, and the stress accumulated during cyclic bending before the first interruption and IMC formation as well as plating process can also be greatly relaxed as mentioned in Chapter 3. This restricts the following creep in the secondary stage that prohibits the nucleation of more surface defects (Figure 4.4 (c)). It leads to the limited nucleation of new surface defects after initial cycles, which contributes to the overall non-continuous nucleation of surface defects for interrupted cyclic bending with small stress accumulation.

For NWs, their formation is more localized compared to larger surface defects excluding NWs. The local stress state is greatly influenced by the specific local GB orientations and geometry. It causes stress fluctuations, and very small stress accumulation can lead to the formation of NWs. This creep model is not applied well to the formation of NWs, and it helps explain the no obvious

NW density difference between interrupted and continuous cyclic bending. It also indicates that though strain amplitude is very critical for NW formation, it can deviate from the perfect positive relationship between strain amplitude and NW density as shown clearly in Figure 3.23.

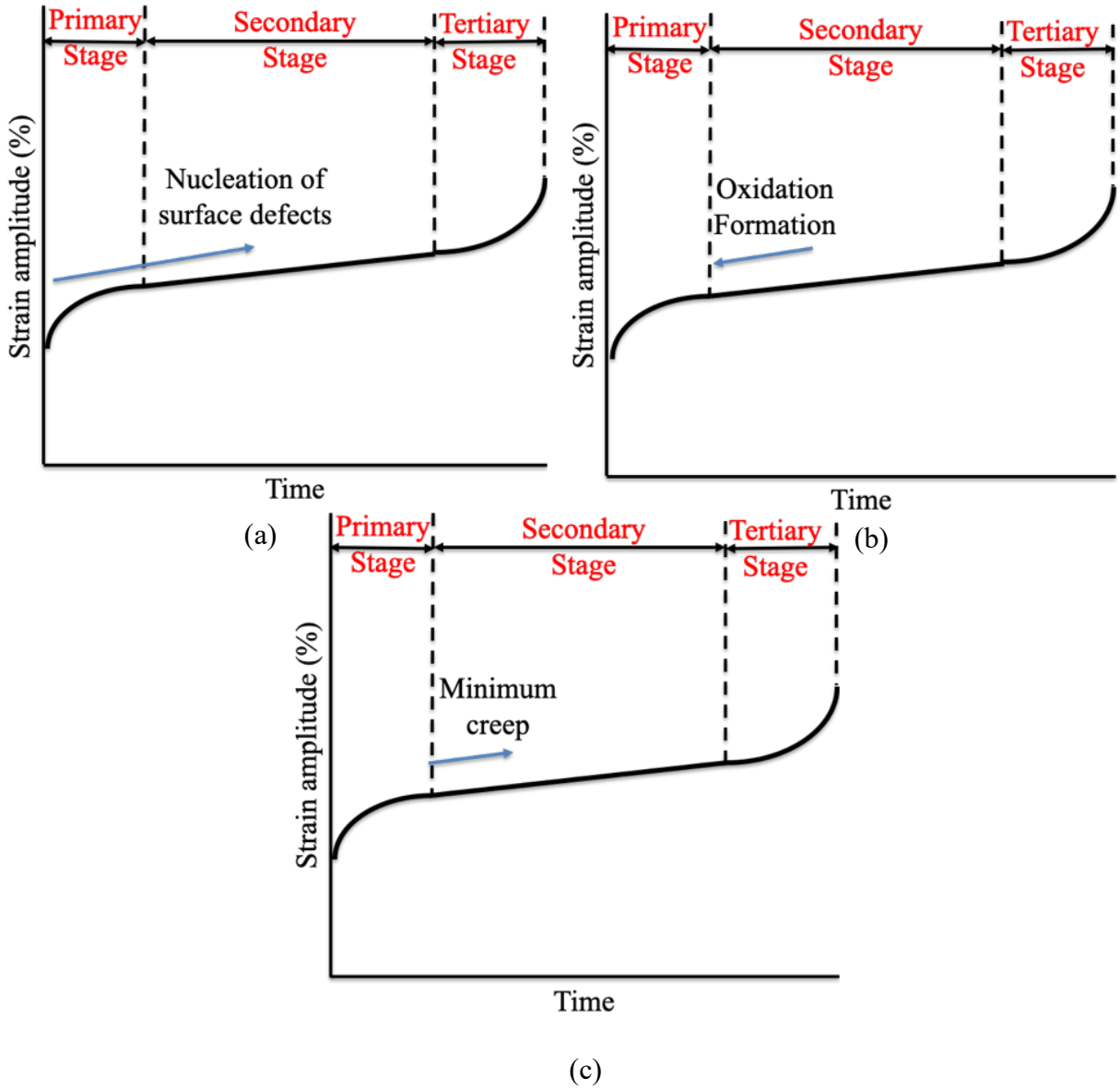


Figure 4.4. A series of schematics show creep behavior of tin films during cyclic bending process. (a) surface defect formation through the Primary and Secondary Stage upon compressive stress; (b) oxidation formation on film surface during tensile half cycle and the rest period between interruptions; (c) the minimum creep restricted in the Secondary Stage prohibits new defect nucleation for the following compressive half cycle.

The defect density for continuous cyclic bending after 7.5M cycles is about 1200/mm$^2$. It is higher than the value of 100/mm$^2$ for 5.8 $\mu$m electroplated tin films with a grain size of 3.22 $\mu$m after room aging for 150 h [50] and the value of 450/mm$^2$ for 5 $\mu$m electroplated tin films with a grain size of 3.5-4 $\mu$m after room aging for 21 days [35]. It indicates that the cyclic bending experiment without interruptions greatly promotes defect formation compared to that at RT. Though it is smaller than the defect density of 2000/mm$^2$ for 5 $\mu$m electroplated tin films with a grain size of 3.5-4 $\mu$m after 20 cycles of RTC between -40 $^o$C to 85 $^o$C [35], the time to achieve cyclic bending and thermal cycling is different. For thermal cycling, 20 cycles can be achieved in 7 h, and 7.5 M cycles with a frequency of about 600 Hz can be achieved in only 3.5 h. It is inferred that continuous cyclic bending to about 7 h may achieve defect density of over 2000/mm$^2$. Thus, continuous cyclic bending can accelerate defect formation compared to that for room aging and thermal cycling due to the extreme fast transition between compressive and tensile stress.

## 4.5 **Summary**

The comparison between interrupted and continuous cyclic bending was present in this chapter. The types of surface defects are similar for these two conditions with only defect density difference. The major conclusions are as follows:

(1) The ratio of all the surface defect density and density of larger surface defects excluding NWs is about the same as the ratio of the initial cyclic numbers for interrupted and continuous cyclic bending, respectively. The stress accumulation during each cycle and cycle numbers have great effect on the formation of larger surface defects.

(2) NW density is similar for interrupted and continuous cyclic bending. The formation of NWs is more influenced by the local stress state. The different requirement for diffusion and mass transport distinguishes the response of NWs from other surface defects.

(3) The difference between interrupted and continuous cyclic bending is resulted from the creep behavior and the break of oxide layer on the film surface as the prerequisite for defect formation.

# 5. THE INFLUENCE OF TEMPERATURE ON CYCLIC BENDING OF LARGE CANTILEVERS IN MM RANGE

## 5.1 Motivation

As discussed in Chapter 3, temperature has a significant effect on cyclic bending of tin films with a relative low melting temperature compared to cyclic bending of other materials systems. The homologous temperature of Sn is much higher than that of other materials systems at RT. The corresponding thermal effect leads to the creep behavior of tin films. Thus, the self-diffusion of Sn along Sn GBs is fast and facilitates the diffusive mass transport for defect formation. Coble creep in tin is postulated to distinguish the behavior of tin films from the other studied metals during cyclic bending.

The aim of this chapter is to emphasize the effect of temperature on cyclic bending experiment. If the cyclic bending experiment is done at relative low temperature (T), the creep behavior slows down due to the decreasing diffusion coefficient of Sn atoms. The ideal situation is when the temperature can reach as low as 131 K as discussed in section 3.3.3, the response of tin films is assumed to be similar as that of Cu and Al films due to the similar homologous temperature. The dominated surface defects are larger defects, and the density of NWs is greatly reduced by this temperature effect. To verify this hypothesis, samples vibrated at the same resonant frequency and interrupted for the same number of cycles should be done both at RT and low T. For the low T experiment, a flow of nitrogen ($N_2$) gas cooled using liquid nitrogen ($LN_2$) was used.

## 5.2 Procedures

The fabrication of the cantilever is similar as mentioned in Chapter 3 and 4. The cyclic bending experiment is also done with the LDV system. To achieve the low temperature environment for cyclic bending, a dewar and a gas line that is connected between the pure $N_2$ gas and the sample area were used in this research. The function of the dewar is to install $LN_2$, and the gas line was used to facilitate the transport of the $N_2$ gas from RT to low T with the aid of $LN_2$. The gas flow of $N_2$ was controlled by the flowmeter. There was not precise gas flow in this research. The gas flow was adjusted during the research to guarantee both the steady low T and minimizing the influence of gas flow that can cause additional vibration during cyclic bending experiment.

Several rings of hollow Cu coils were immersed in $LN_2$ during the cyclic bending process of low T, and they are fixed to the cap of the dewar. This guarantees the sufficient time scale that achieves the transit from RT $N_2$ to low T $N_2$ successfully. When the experiment was in process, a continuous sufficient supply of $LN_2$ is needed to guarantee the steady temperature with occasional refills dependent on the monitored real-time temperature. To achieve this, there is a funnel fixed to the cap of the dewar for the pour of $LN_2$ at any time. Some tin foil was used to seal the outlet of the funnel when the experiment was in progress and did not need refill to decrease the volatilization of $LN_2$. A simplified schematic showing the whole system of low T cyclic bending set up is exhibited in Figure 5.1.

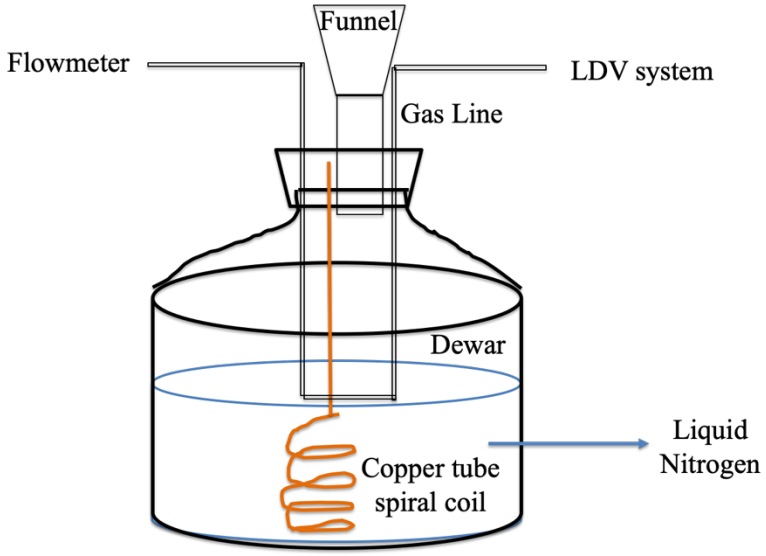


Figure 5.1. A simplified schematic showing the set-up of cyclic bending experiment at low T

The temperature during the low T cyclic bending was monitored by thermocouple. The temperature was stabilized at 223 K with the adjustment of the nitrogen flow. To investigate the temperature influence, samples vibrated at the same resonant frequency were done both at RT and 223 K. The types and density of different defects as well as the density ratio between different defects for these two temperatures help distinguish the role of creep behavior and related mass transport. The influence of strain amplitude/ rate, number of cycles, resonant frequency as well as interruptions was also analyzed for the low T experiment. The systematic research was similar as depicted in Chapter 3. Surface defects on tin films were examined using SEM (Quanta 650, FEI). With increasing number of cycles, the same position on the cantilevers was followed to reveal the

morphology evolution. The surface defect density per area (#/mm$^2$) was measured as a function of position along the cantilever (or strain amplitude/rate). Defects were cross-sectioned using FIB milling and imaged by both secondary electrons (SEs) and ion beam (Quanta 3d, FEI).

## 5.3 Results and Discussion

### 5.3.1 Evolution of Tin Films Morphologies

The defect types after cyclic bending at low T are quite similar to those observed at RT. There are still three types of defects: micro-sized surface defects, IGBs and NWs. An example showing the evolution of the same area for cyclic frequency at 223 K is exhibited in Figure 5.2. The SEM images are taken at 3.24M, 5.4M and 7.5M cycles respectively from Figure 5.2 (a) to (c).

All types of surface defects evolve with additional number of cycles. The micro-sized surface defect in the center of the area remains the same through 5.4M cycles with appearance of additional IGBs (Figure 5.2 (b)) in the neighboring area of initial IGB shown at 3.24M cycles (Figure 5.2 (a)). The micro-sized defect shows in-plane expansion after cyclic bending for 7.5M cycles and a NW also shows up through the right lower corner of the SEM image (Figure 5.2 (c)). The overall tendency is that the damage of the film surface at low T is more severe with increasing number of cycles compared to that at RT, and it is present through the increase in density of all the surface defects. As the morphology of IGB is more complicated with more extrusions per IGB in multiple directions and the larger basal area including more in-plane grains for each individual IGB, the IGB formation also becomes more severe compared to that for cyclic bending at RT (Figure 3.4).

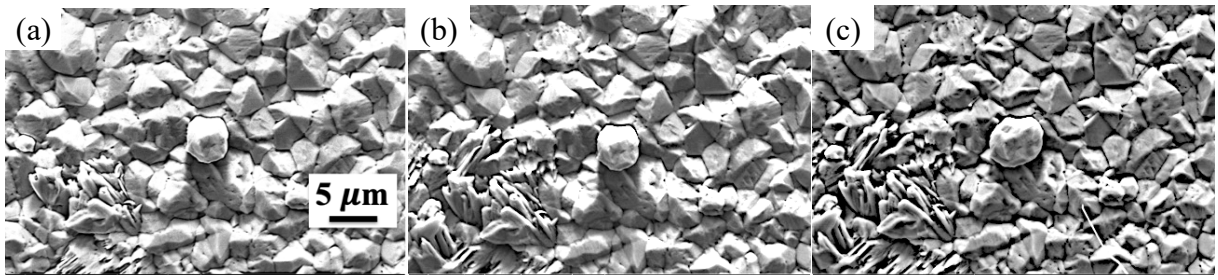


Figure 5.2. SEM images of the same area on film surface during cyclic bending at low T of 223 K. (a) after 3.24M cycles; (b) after 5.4M cycles; (c) after 7.5M cycles

Some of the micro-sized surface defects remain the same morphology after nucleation and initial growth at low T, as shown in Figure 5.3. Clear evidence of horizontal and vertical striation steps is shown at the bottom of the defects, which are also observed for micro-sized surface defects for cyclic bending at RT (Figure 3.6 and Figure 3.7). The vertical lines relate to the original GB morphologies while the horizontal lines correspond to the cyclic bending process. The progression of GB positions between the defect and its neighboring grains can also been observed with the change of both diameter and growth geometry(Figure 5.3 (b)), which has also been shown for the surface defect on similar electroplated tin films [34]. The grain size of the original in-plane grain where the defect nucleates is smaller than the final constant area that the defect grows out of the film. The growth rate varies through the whole grain initially, and it contributes to the asymmetrical growth profile as shown on the defect surface. When the growth rate becomes constant and steady, the diameter of the defect is fixed without migration, corresponds to the striation bottom. Some white dots are attached on the surface of the defect (Figure 5.3 (f)), and it is hypothesized to be an artifact or contamination due to the SEM imaging process.

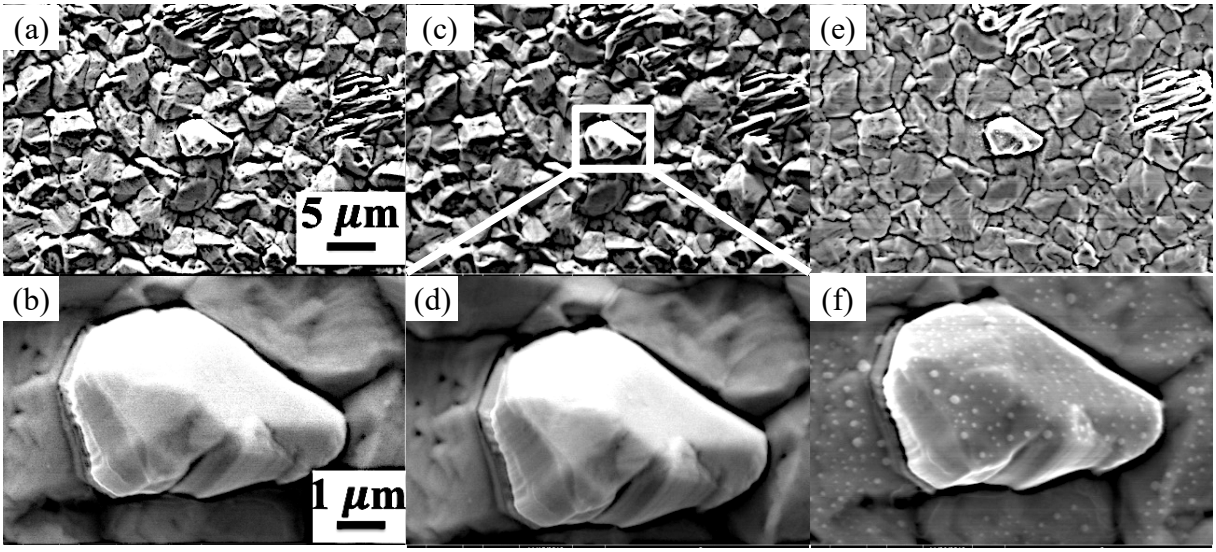


Figure 5.3. SEM images show no obvious evolution for a micro-sized defect during cyclic bending at low T; (a), (b) after 3.24M cycles; (c), (d) after 5.4M cycles; (e), (f) after 7.5M cycles. (b), (d) and (f) are the enlarged SEM image of the surface defect in fig. (a), (c) and (e), respectively.

Some micro-sized surface defects evolve into IGBs with increasing stress accumulation for cyclic bending at low T, as shown in Figure 5.4. Part of the grain approaching GBs evolves into extrusions after vibrating for 7.5M cycles (Figure 5.4 (b)). Extrusions grow out of the surface and

intrusions grow inside the surface grain corresponding to the traces of the wrinkles acting as preferred sites for damage due to the high local stress state. The extrusions and intrusions can evolve into more complicated morphologies resulting from more wrinkles forming on the film surface with increasing number of cycles (Figure 5.4 (d) and (f)). The progression along GBs is greatly influenced by misorientation and coupling between IGB and neighboring grains.

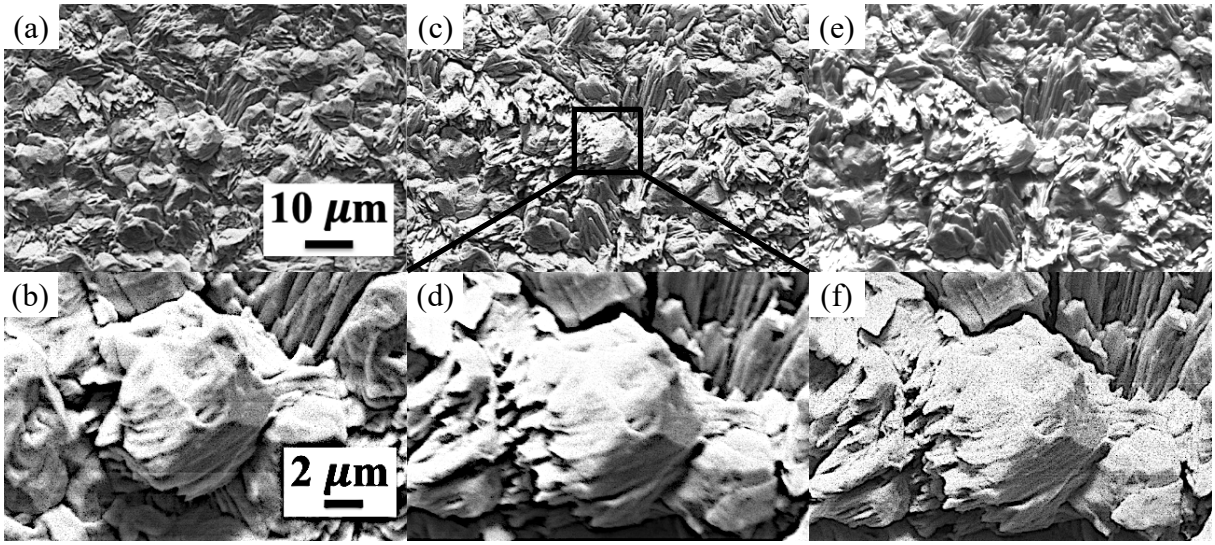


Figure 5.4. SEM images show transition from a micro-sized defect to an IGB during cyclic bending at low T. (a), (b) after 7.5M cycles; (c), (d) after 14M cycles; (e), (f) after 20M cycles. (b), (d) and (f) are the enlarged SEM image of the defect in fig. (a), (c) and (e), respectively

In additional to evolve into IGBs, the evolution of some micro-sized defects during cyclic bending at low T (Figure 5.5) is similar to that for tin films in other conditions. A new micro-sized surface defect nucleates from an in-plane grain ("marked area" in Figure 5.5 (a) and (b)) and the pre-existing defect shows changes in length and growth direction. The co-existing of all three kinds of surface defects (Figure 5.5 (e) and (f)) or only two kinds of defects (Figure 5.5 (a)-(d)) in a local area is highly dependent on the strain gradients that arise from variations in local strain due to elastic anisotropy and to the ability of the local microstructure in response to the stresses.

The evolution of NW is similar to that for cyclic bending at RT (Figure 3.8 and 3.9). The root of NW is either from a GB or the extrusion of an IGB (Figure 5.6). Some NWs do not evolve any more after its initial appearance while some only exhibit the same growth direction with constant diameter for additional cyclic bending ("marked area" in Figure 5.6 (a) and (c)). A new NW also extends out from one extrusion of the IGB ("marked area" in Figure 5.6 (b) and (d)). One

hypothesis for the preferred NW nucleation at IGB extrusions is due to the previous breakup of the oxide layer to achieve IGB formation. This leads to a "weak spot" to facilitate the subsequent NW nucleation, similar as that created by previous NW shown in Figure 3.11. The nucleation site of a NW is usually surrounded by several IGBs at low T and there is no gathering of several NWs as shown at RT (Figure 3.12), and it reflects a different surface morphology for NW nucleation and lower NW density compared to that at RT.

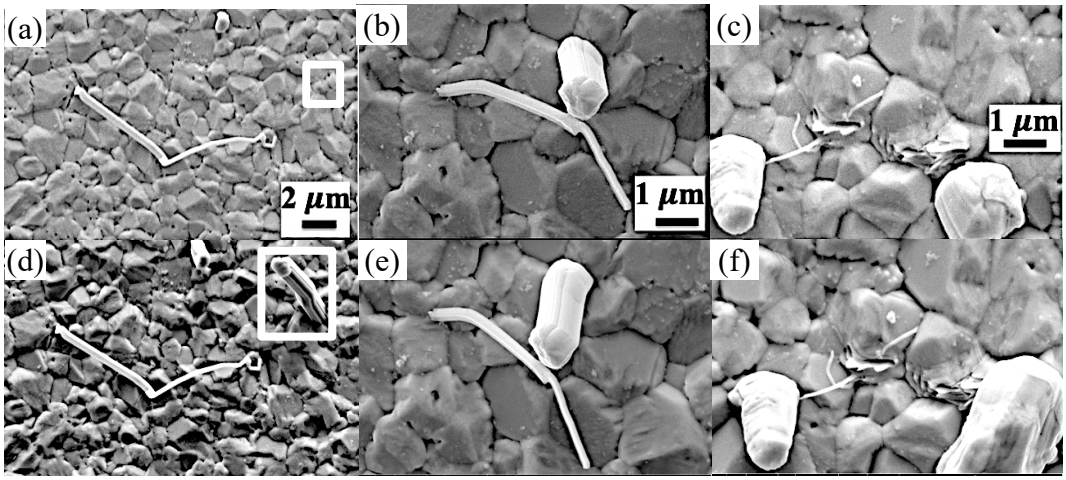


Figure 5.5. SEM images show nucleation and growth of micro-sized defects during cyclic bending at low T; (a), (b), (c) after 3.24M cycles; (d), (e), (f) the same area of fig. (a), (b), (c) respectively after 5.4M cycles. The marked area in fig. (a) and (d) indicates the formation of a new defect.

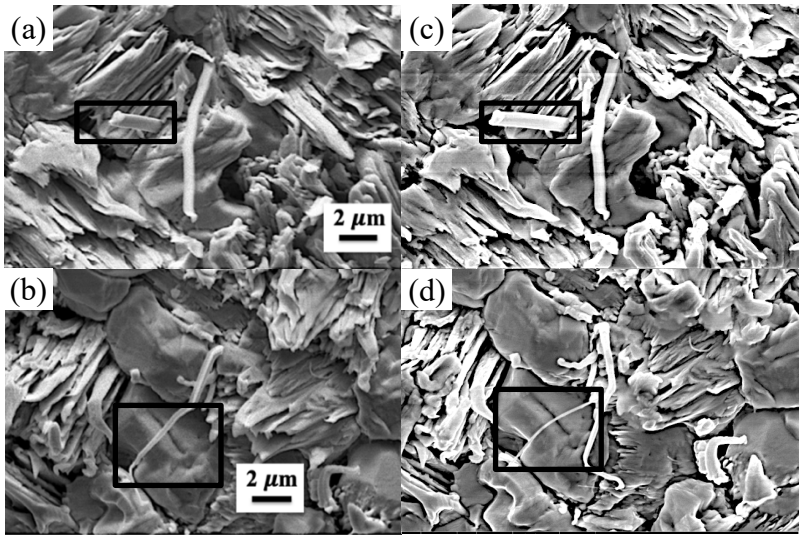


Figure 5.6. SEM images show evolution of NWs during cyclic bending at low T. (a), (b) after 7.5M cycles; (c), (d) after 14M cycles. The marked area in fig. (a) and (b), fig. (c) and (d), respectively indicates the same NW.

The growth direction of NW can also evolve during the cyclic bending at low T (Figure 5.7). There is a kink on the NW to distinguish the two stages of initial growth and the further growth of the same NW for additional cyclic bending ("marked area" in Figure 5.7 (d)), indicating dynamic change of NW growth direction over time. For other NWs (Figure 5.7 (e) and (f)), the growth axis just changes directly from one direction to another. It verifies the NW grows from the root to the top, and this is similar to the mechanism for micro-sized surface defect formation under other conditions [60]. The interruption makes it possible to achieve the rearrangement of Sn atoms and redistribution of local strain energy, thus contributes to the growth direction evolution of NW and the formation of new NWs (Figure 5.6).

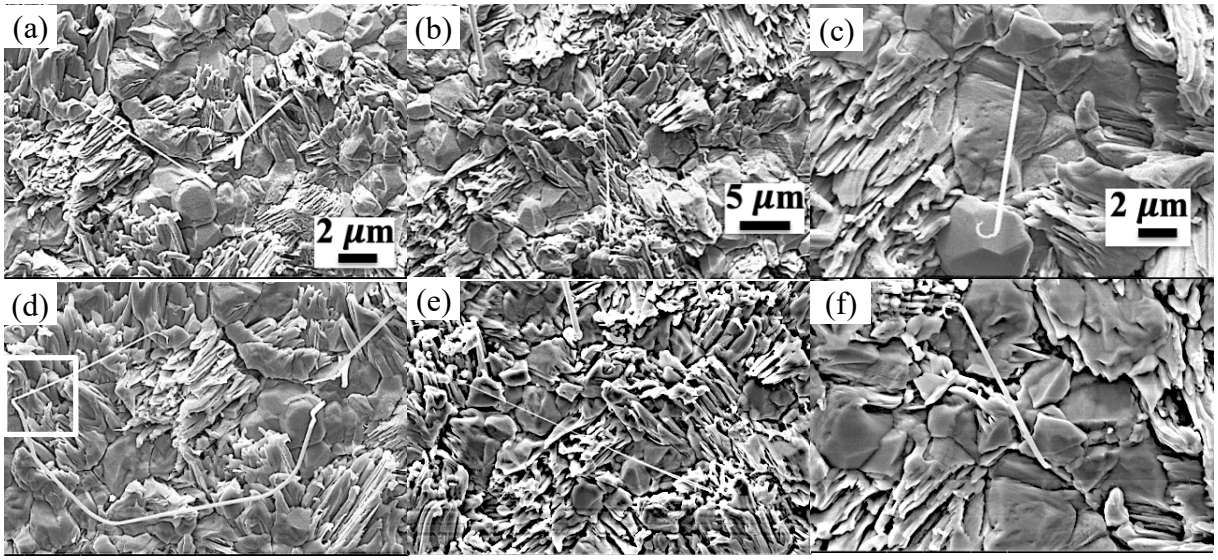


Figure 5.7. SEM images show growth direction change of NWs during cyclic bending at low T. (a), (b), (c) after 7.5M cycles; (d), (e), (f) same area of (a), (b), (c) respectively after 14M cycles. The marked area in fig. (d) indicates the kink during NW evolution.

For cyclic bending at low T, the damage of the surface morphology is dominated by IGBs with fewer micro-sized surface defects and NWs (Figure 5.8). The area marked as "1" in Figure 5.8 (a)-(c) and (d)-(f), respectively shows the evolution of IGB from in-plane grains. The evolution of IGBs usually originate from 4~5 in-plane neighboring grains, and the basal area is much larger than that of IGBs formed at RT, usually only 1~2 grains (Figure 3.4). The number and length of extrusions per IGB is also larger than that for cyclic bending at RT. It is hypothesized that low T promotes the formation of IGBs and causes more damage on the film surface. The area marked as

"2" in Figure 5.8 (a)-(c) and (d)-(f), respectively corresponds to the formation of NWs in the presence of micro-sized surface defects and IGBs. The lifting of the whole or part of the in-plane grain can also be observed, and it is assumed to be the initial stage of IGB formation.

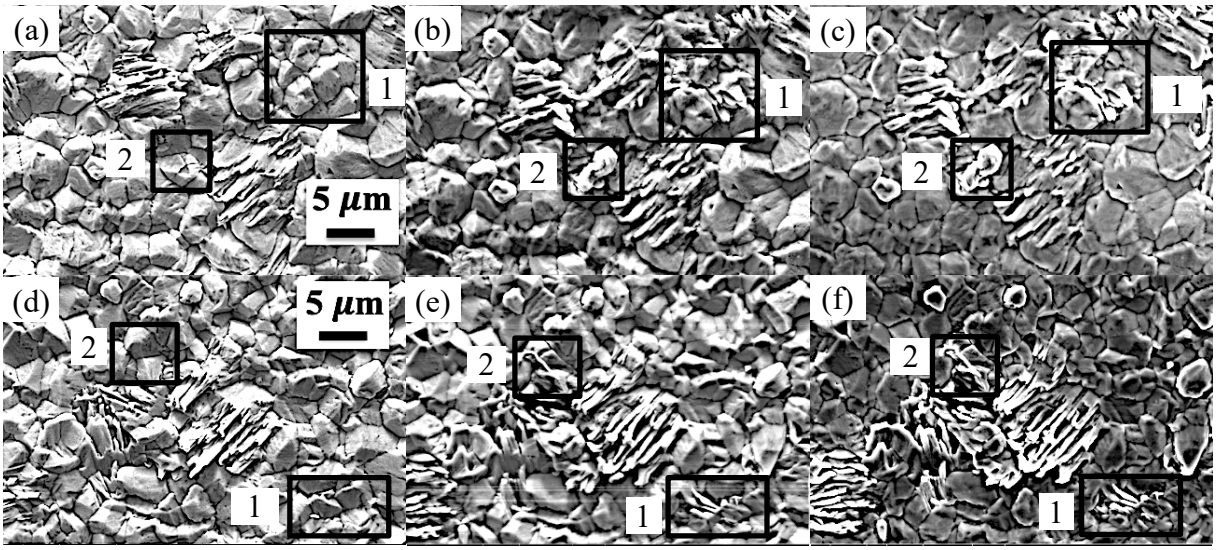


Figure 5.8. SEM images show evolution of IGBs in the same local area during cyclic bending at low T. (a), (d) after 7.5M cycles; (b), (e) after 14M cycles; (c), (f) after 20M cycles. Some of the morphology changes have been marked in squares.

In additional to be originated from micro-sized surface defects (Figure 5.4), IGBs can also develop from in-plane grains (Figure 5.9). Figure 5.9 (a)-(c) and Figure 5.9 (d)-(f) show the evolution of two representative IGBs. The initial morphology is uneven surface with traces of folds (Figure 5.9 (a) and (d)). IGB develops with lift-up of part or the whole grain corresponding to the initial wrinkles on the surface (Figure 5.9 (b) and (e)). The lack of obvious evolution for IGBs with additional cyclic bending to 20M cycles (Figure 5.9 (c) and (f)) is due to the continuous stress relaxation especially when the film is static during the examination of the morphology evolution as mentioned in the experimental procedures. This is not observed for cyclic bending at RT with other parameters keeping constant. It is hypothesized that low T promote the transition from micro-sized surface defect into IGBs.

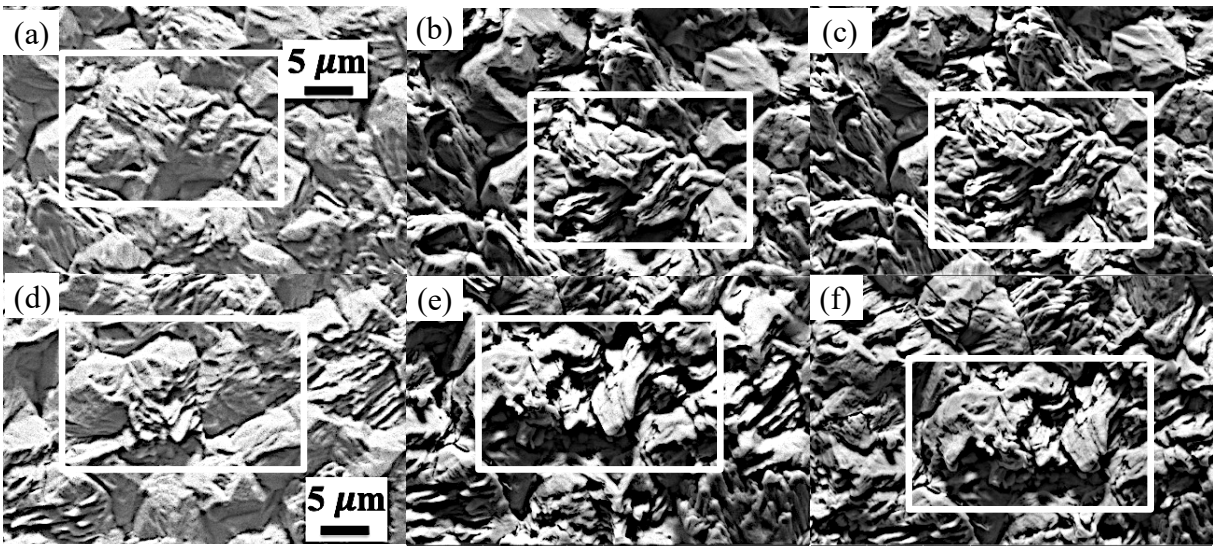


Figure 5.9. SEM images of IGB formation from in-plane surface grain during cyclic bending at low T. (a), (d) after 7.5M cycles; (b), (e) after 14M cycles; (c), (f) after 20M cycles. The morphology changes have been marked in squares.

As explained in Figure 3.14, the curvature of NW indicates accommodation of self-weight and driving force for NW growth balance. It can be inferred that when the driving force cannot overcome the weight increase of NWs with continuing growth during cyclic bending even with curvature of NWs (Figure 5.7), the NW will break due to the force imbalance. The severe surface damage also promotes break of NW at low T due to the coupling of several slip systems at the root of the NW. This phenomenon is not observed for cyclic bending at RT for the same cyclic numbers, and it is inferred that RT experiment needs additional cycles to achieve fall-off of NWs with the less damaged surface during cyclic bending. Figure 5.10 (b) and (d) shows the fall-off of the entire NW while Figure 5.10 (f) shows partial fall-off with remaining of NW root. In theory, the position where the NW fall-off is the highest stress during cycling, and it is usually approaching the root of the NW. For NW where only part breaks off, it is hypothesized that a flaw formed during NW growth. This is similar to the grooves formed during the previous thermal cyclic experiment based on the "pinch-off" model [35].

Low T can also change the surface morphology of the IGB compared to IGBs at RT (Figure 5.11). The magnified SEM images show that there is a transition from the initial normal surface morphology (Figure 5.11 (b)) to the large area of frostbite traces (Figure 5.11 (d)) on the extrusions of IGB with increasing number of cycles. It indicates further cracks and brittleness of IGBs as well as the peel-off of the surface layers on extrusions caused by low T. Figure 5.12 is an example

showing that IGBs (Figure 5.12 (b)) replace two NWs (Figure 5.12 (a)) in the same local area during cyclic bending at low T with the lack of the detailed process that needs to be revealed with more interruptions during cyclic bending.

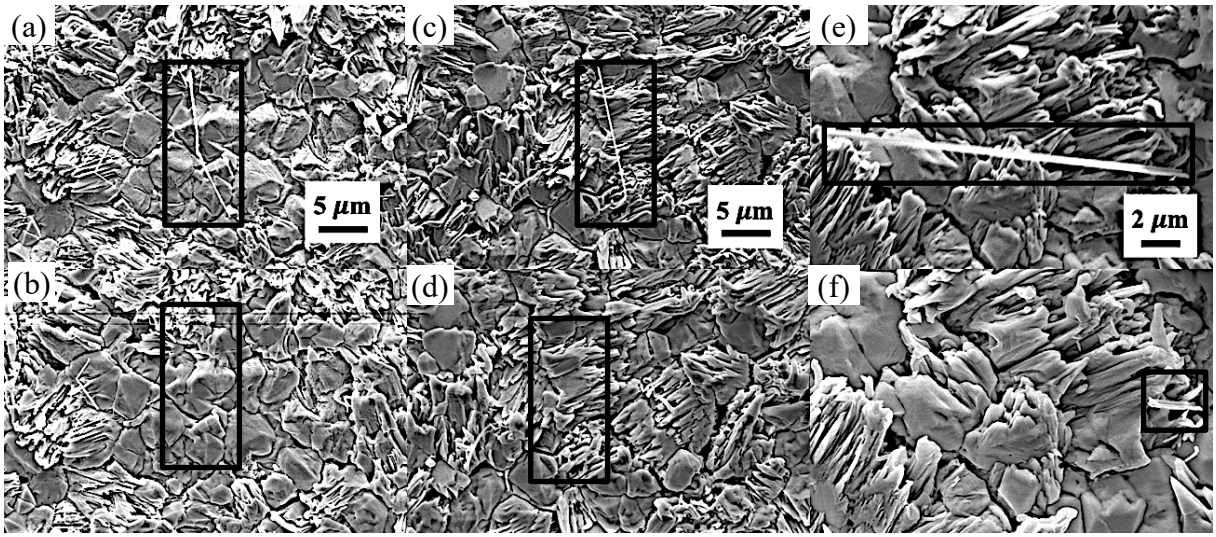


Figure 5.10. SEM images show fall-off of the entire or partial NW. (a), (c), (e) after 7.5M cycles; (b), (d), (f) the same region of fig. (a), (c), (e) after 14M cycles. The fall-off of the entire NW (fig. (a)-(d)) or partial NW (fig. (c) and (f)) can be seen in the square area.

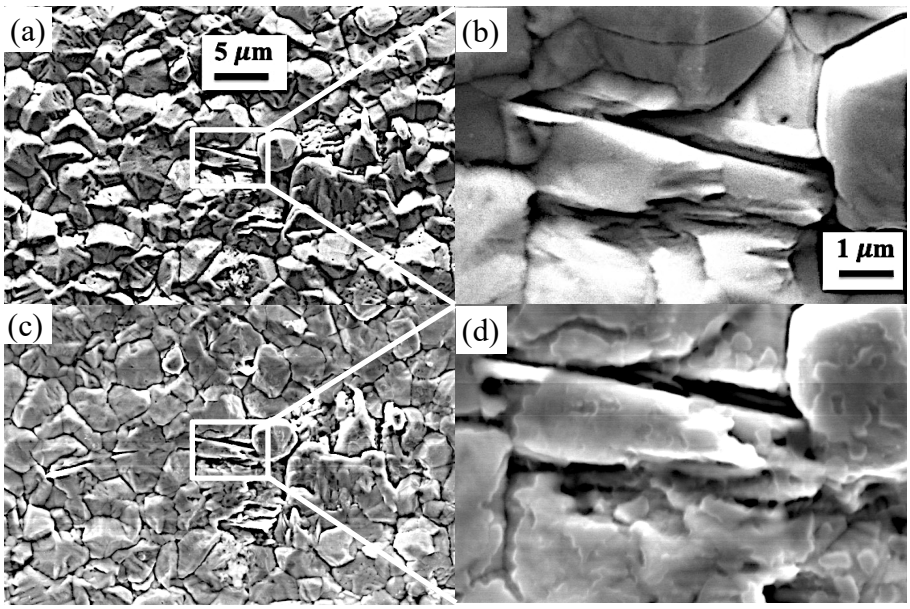


Figure 5.11. SEM images show frostbites and cracks on extrusions of IGB. (a), (b) after 7.5M cycles; (c), (d) the same area in fig. (a), (c) respectively after 14M cycles

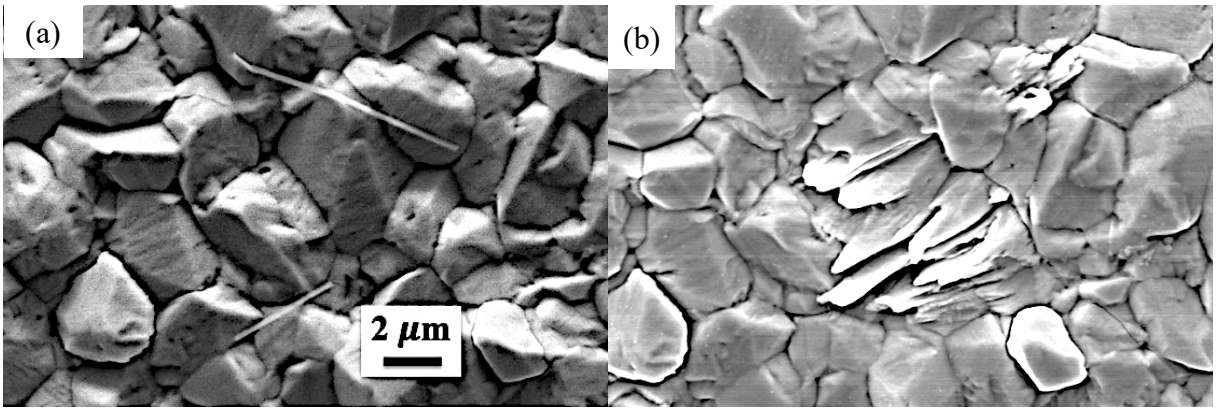


Figure 5.12. SEM images show transition from NWs to IGB in a local area during cyclic bending. (a) after 7.5M cycles; (b) after 14M cycles

The cross-section images of IGB show porous regions in a larger area (Figure 5.13) compared to that for IGB formed at RT (Figure 3.18). Some porous regions are approaching the surface of the IGB, and it relates to the in-plane morphology of IGB that shows a different perspective of the surface morphology from the top view. The porous regions inside tin films can only be observed by cross-section images. The FIB cut was done for the same IGB in sequence from position 1 to position 3 (Figure 5.13 (a)), and the position number is marked at the upper right corner of the image (Figure 5.13 (b)-(e)). The SE image is more favored for showing the structure or morphology due to the limited penetration distance by ions while the ion image helps distinguish different grains, GBs and phase compositions. The difference of IGB cross-section morphology with the cut position represents the evolution of intrusions. It also corresponds to the evolution of extrusions above the surface since IGB is the results of coupling between intrusions and extrusions. The ion image (Figure 5.13 (c) and (e)) shows that the porous regions in the film can be divided into three categories. One is at the GB between two grains beneath the IGB, one is extending into surface grain from the GB, and the third is extending from regions approaching the interface between the film and the substrate into the film. The porous regions also change with the cut position in consistent with the surface morphology. The almost unchangeable cross-section image between Figure 5.13 (d) and (f) indicates a similar IGB morphology from cut 2 to cut 3. This verifies the parallel hollow parts in Figure 3.18 which can be revealed by switching cut direction by 90$^{o}$ to do the FIB milling for this IGB. The overall more severe damage in the film corresponds to a more complicated morphology on the film surface compared to that at RT.

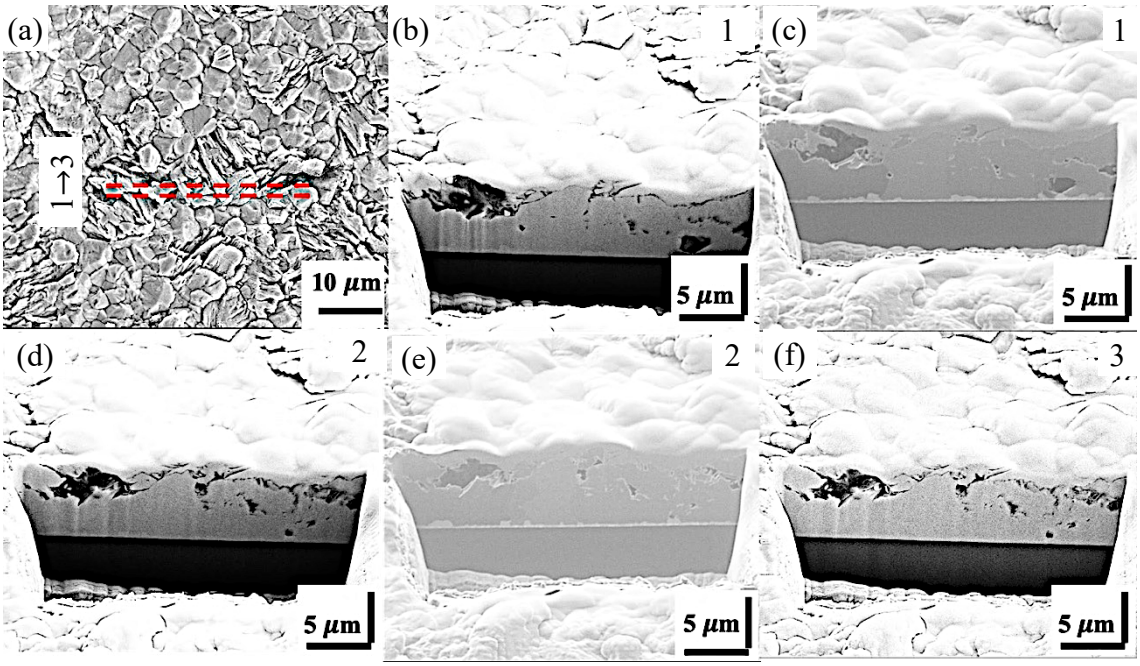


Figure 5.13. SEM images show complicated morphologies with hollow parts beneath IGBs formed at low T. (a) surface morphology of the IGB; (b), (d), (f) Second electron (SE) image shows the IGB surface morphology at different cut positions from 1 to 3 by FIB milling; (c), (e) ion image taken at 52° corresponding to fig. (b), (d), respectively

Figure 5.14 shows more IGB cross-section morphology with FIB cut from position 1 to position 4 for the same IGB. Porous regions always extend from the GB into the grain beneath the IGB, and it is different from the three positions of the porous regions as mentioned in Figure 5.13. It is hypothesized that the positions of the porous regions are highly dependent on the local location of the IGB, and it relates to the grain misorientation between IGB grain and its neighboring grain. IMC formed at the interface between the film and the substrate is uniform within the grain and shows the accumulation at the GBs beneath IGB (Figure 5.13 and Figure 5.14), this is similar to what has been observed for micro-sized surface defects (Figure 3.15 (d)). It is contrast to the situation for NW without IMC accumulation at the GB where NW nucleates (Figure 3.15 (e)), and it is inferred that IMC formation has different effect for defects with different dimensions. One common characteristic for IGBs formed at RT (Figure 3.18) and IGBs formed at low T (Figure 5.13 and Figure 5.14) is that there are no voids formation at the interface between tin film and Cu layer. This differs from the situations for cyclic bending of Cu film on different substrates below hillocks or extrusions with voids at the interface [42,43,59]. The reason for this different behavior at the interface with be hypothesized later in the discussion part.

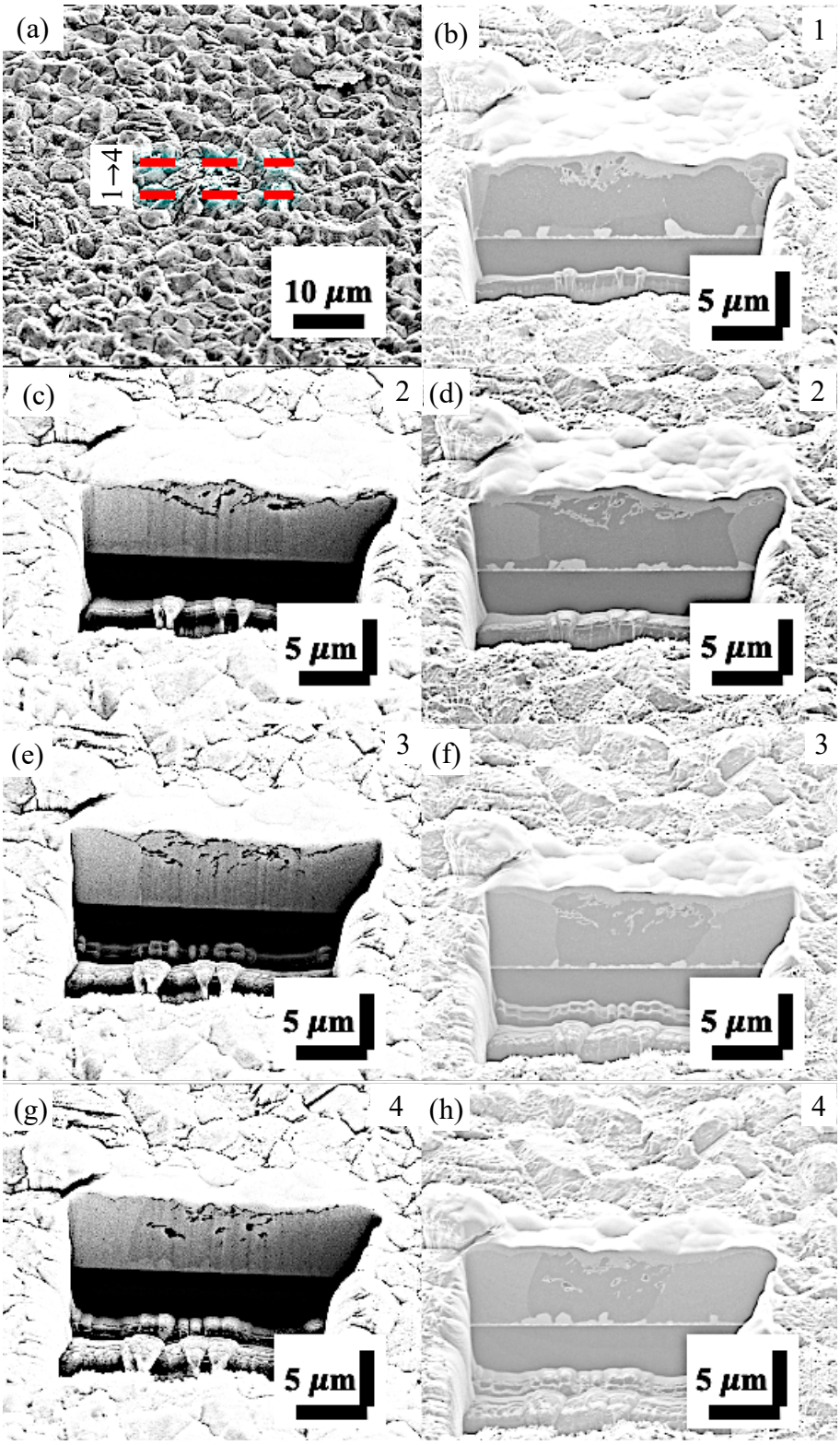


Figure 5.14. SEM images show another IGB formed at low T. (a) surface morphology of the IGB; (b), (d), (f), (h) ion image taken at 52° shows the cross-section morphology of IGB at different cut position from 1 to 4; (c), (e), (g) SE image corresponding to fig. (d), (f), (h) respectively

### 5.3.2 Quantitative Comparison of Defect Density for Cyclic Bending at RT and low T

To investigate the influence of temperature on cyclic bending, two samples were vibrated at the same frequency (226.3 Hz) and base displacement for 7.5M cycles at RT and 223K. The density for all the surface defects is shown in Figure 5.15. The defect density before cyclic bending is uniform along the whole cantilever (marked as "original" in Figure 5.15 (a)) and is similar for RT and low T experiment. The defect density is directly correlated with the strain amplitude along the cantilever for both RT and low T, and it is consistent with the conclusion got in Chapter 3. Low T exhibits a smaller defect density compared to that at RT, especially with higher strain amplitude (fixed end). The original defect density is deducted from all the surface defect density (Figure 5.15 (b)), and it shows the defect density caused only by cyclic bending. The density difference between cyclic bending at RT and low T is mainly in the high strain area, from 50 % of the cantilever length to the fixed end. The maximum density difference approaching the fixed end is about 250/mm$^2$, and the density at RT is about ~15% more than that at low T.

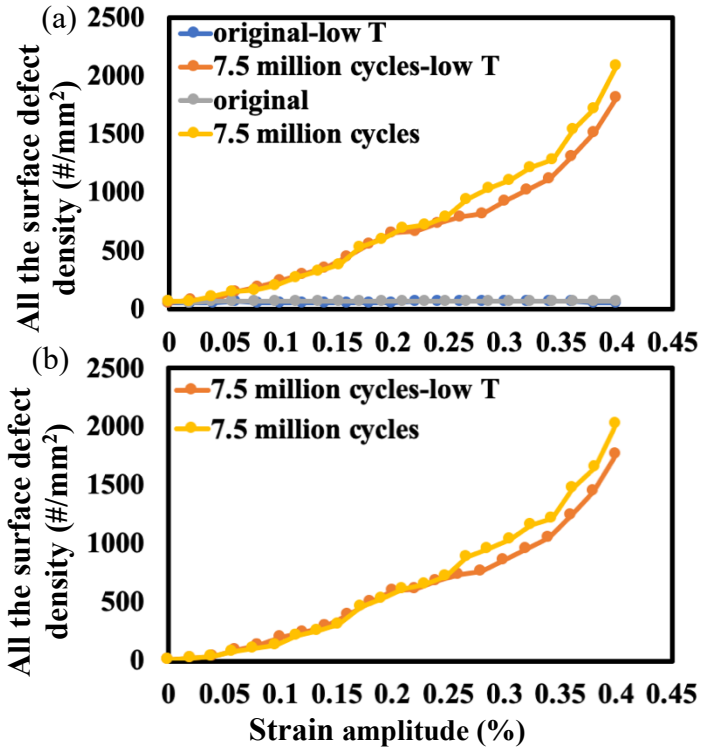


Figure 5.15. All the surface defect density along the cantilever (exhibited as strain amplitude) for cyclic bending at RT and low T after 7.5M cycles. (a) the total defect density and defect density before cyclic bending due to plating stress and IMC formation (marked as "original"); (b) defect density evolution only due to the cyclic bending process

To show the effect of low T on each type of surface defects, the defect density along the cantilever for micro-sized defects, NWs and IGBs both at RT and low T is exhibited in the same scale in Fig. 5.16. It can be seen that the dominated surface defects are IGBs, followed by micro-sized surface defects and finally NWs regardless of temperature effect. The fact that the density of IGBs is much higher than that of other defects indicate that both low frequency and low T promote IGB formation, and the detailed analysis will be discussed later.

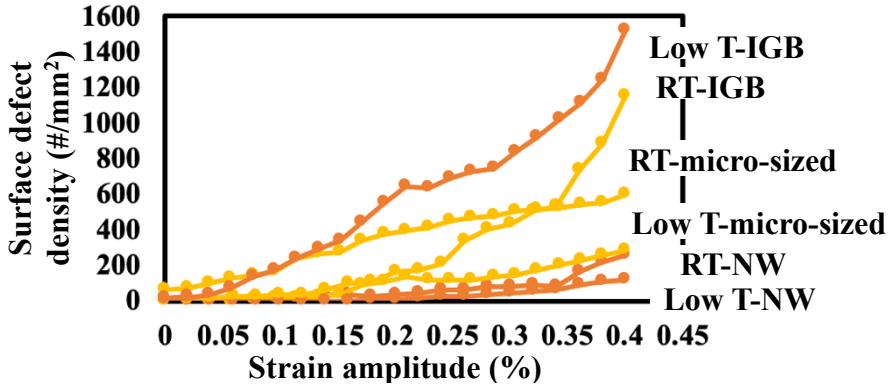


Figure 5.16. Plot shows density of micro-sized surface defects, NWs and IGB in the same scale along the cantilever (strain amplitude) for cyclic bending at RT and low T after 7.5M cycles

The defect density for micro-sized defects, NWs and IGBs exhibited in different scales to show the details is shown in Figure 5.17 (a), (b) and (c), respectively. The film surface of the low T experiment has fewer micro-sized surface defects (Figure 5.17 (a)) and NWs (Figure 5.17 (b)) compared to that of RT cycling, while the IGB density (Figure 5.16 (c)) is much higher at low T than at RT. There are no NWs with strain amplitude smaller than 0.15% at low T (Fig. 7(b)), indicating a critical strain amplitude for NW formation. There is also a similar critical strain amplitude for IGB formation at RT, and the IGB density increases significantly for strain amplitudes above 0.2 % at RT. The maximum defect density of micro-sized defects and NWs at RT is ~ 2.5 times of that at low T while the maximum defect density of IGB at RT is ~0.75 of that at low T. IGBs are the dominated defects for cyclic bending experiment for this low frequency and low T experiment followed by micro-sized defects and finally NWs. The total defect density excluding NWs (Figure 5.17 (d)) show that the density of IGBs and micro-sized surface defects are similar for these two temperatures, indicating that the temperature has no influence for the larger defects. Low T promotes the transition from micro-sized surface defects into IGBs but does

not affect their total defect density. The difference for the defect density at RT and low T is mainly due to the density difference of NWs.

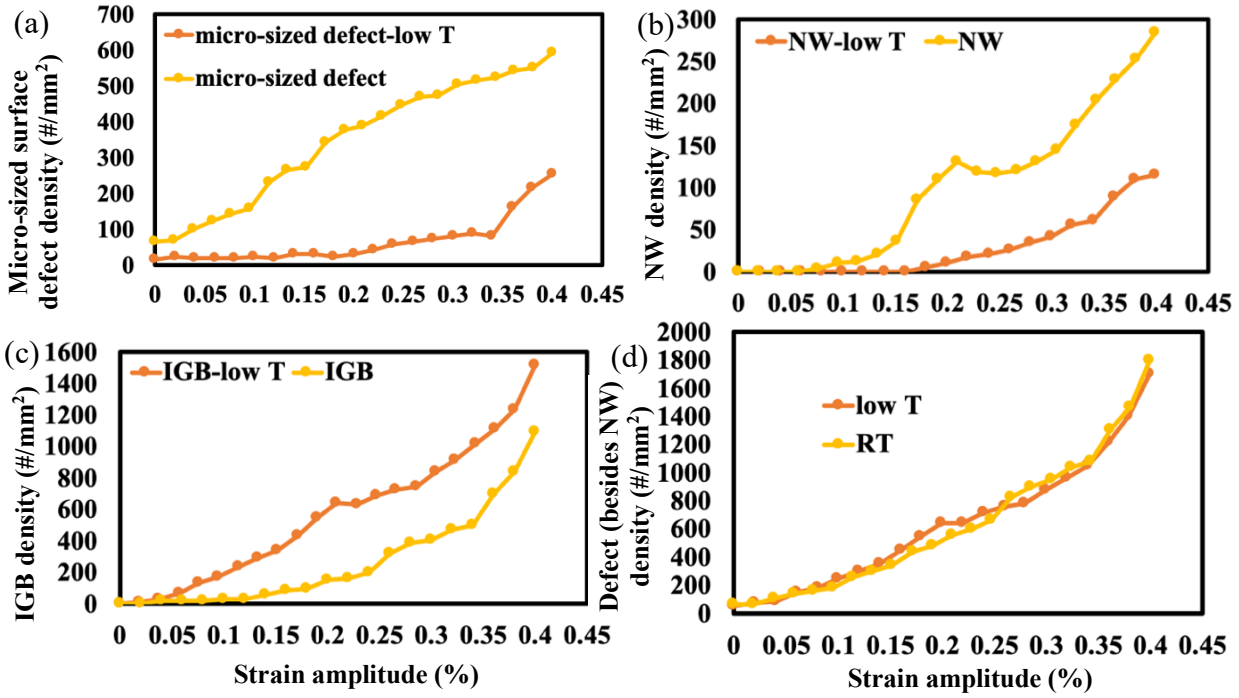


Figure 5.17. Micro-sized surface defect density (a), NW density (b), IGB density (c) and density of larger surface defects excluding NW (d) along the cantilever (exhibited as strain amplitude) for cyclic bending at RT and low T after 7.5M cycles

### 5.3.3 **Quantitative analysis of defect density on Tin films for interrupted cyclic bending**

As mentioned in Chapter 3, the interrupted cyclic bending has a great influence on defect formation for additional cycles due to the influence of continuous stress relaxation on creep behavior of Sn. It is also meaningful to investigate the effect of interruptions on defect formation at low T despite the inhibited creep process and slower diffusion. Since IGBs dominate for low T cyclic bending, the response of IGB density to the interrupted cyclic bending is also analyzed in this section besides the response of NW and micro-sized surface defect density as discussed in Chapter 4. The similarity or difference between interrupted cyclic bending at both RT and low T can shed some light on clarifying the effect of low T for interrupted cyclic bending experiment.

To investigate the influence of interrupted cyclic bending, two significant different frequencies are selected, 116.3 Hz and 1216.9 Hz. The strain amplitude distribution along the cantilever for these two frequencies shows distinct slopes. The maximum strain amplitude at the

fixed end for 116.3 Hz is about 0.8 % while that for 1216.9 Hz is only about 0.08 %, one tenth of that for 116.3 Hz (Figure 5.18 (a)). Despite the strain amplitude difference, the strain rate is similar for these two frequencies with a maximum value of ~ 180 %/sec at the fixed end (Figure 5.18 (b)).

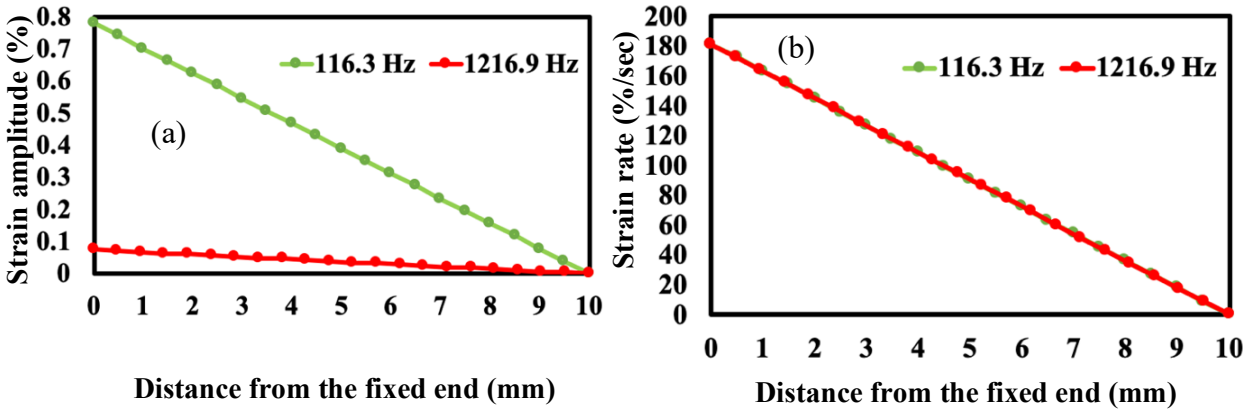


Figure 5.18. strain amplitude (a) and strain rate (b) distribution along the cantilever for two different frequencies of 116.3 Hz and 1216.9 Hz

The overall defect density for all kinds of defects is exhibited in Figure 5.19. The cyclic bending is interrupted once at 7.5M cycles for 116.3 Hz and then stopped at 14M cycles, while the cyclic bending for 1216.9 Hz interrupted at the same number of cycles for 116.3 Hz and continued to the ultimate 20M cycles with one additional interruption. The initial defect density is similar for these two frequencies, and it is also similar to that for cyclic bending at RT (Figure 3.19). Compared with the maximum defect density of fewer than 600/mm$^2$ for 599.38 Hz at RT (Figure 3.19), low T experiment greatly promotes the defect formation with maximum defect density of about 1300/mm$^2$ and 2600/mm$^2$ for 116.3 Hz and 1216.9 Hz, respectively.

The defect density increase due to cyclic bending is obtained by deduction of defect density before cyclic bending from the overall defect density (Figure 5.20). Figure 5.20 (b) and (c) shows the defect density evolution for each individual frequency, offsetting lack of detailed information due to the obvious strain amplitude distribution difference for these two frequencies (Figure 5.19 (a)). The defect density is always higher for high frequency case with fixed strain amplitude (Figure 5.20 (a)) or strain rate (Figure 5.20 (d)). The defect density is still frequency dependent for cyclic bending at low T and the increase of defect density is also negligible for additional cycles after the first interruption, consistent with the results at RT shown in Chapter 3 and 4. The increase of defect density only happens approaching the fixed end of the cantilever from 14M to 20M cycles,

while defect density difference shows up from 50 % of the length to the fixed end from 7.5M to 14M cycles with cyclic frequency of 1216.9 Hz (Figure 5.20 (c)). The defect density increase becomes more difficult to notice with increasing numbers of interruption. It is inferred that the defect density will show no changes along the cantilever after some critical number of cycles even with more additional cycles. The maximum density for all the surface defects cycled at 116.3 Hz is about 1200/mm$^2$, and it is similar to that for cyclic bending at RT with cyclic frequency of about 600 Hz (Figure 4.1). The similar defect density indicates that low frequency and low T has positive effect on defect formation during the cyclic bending.

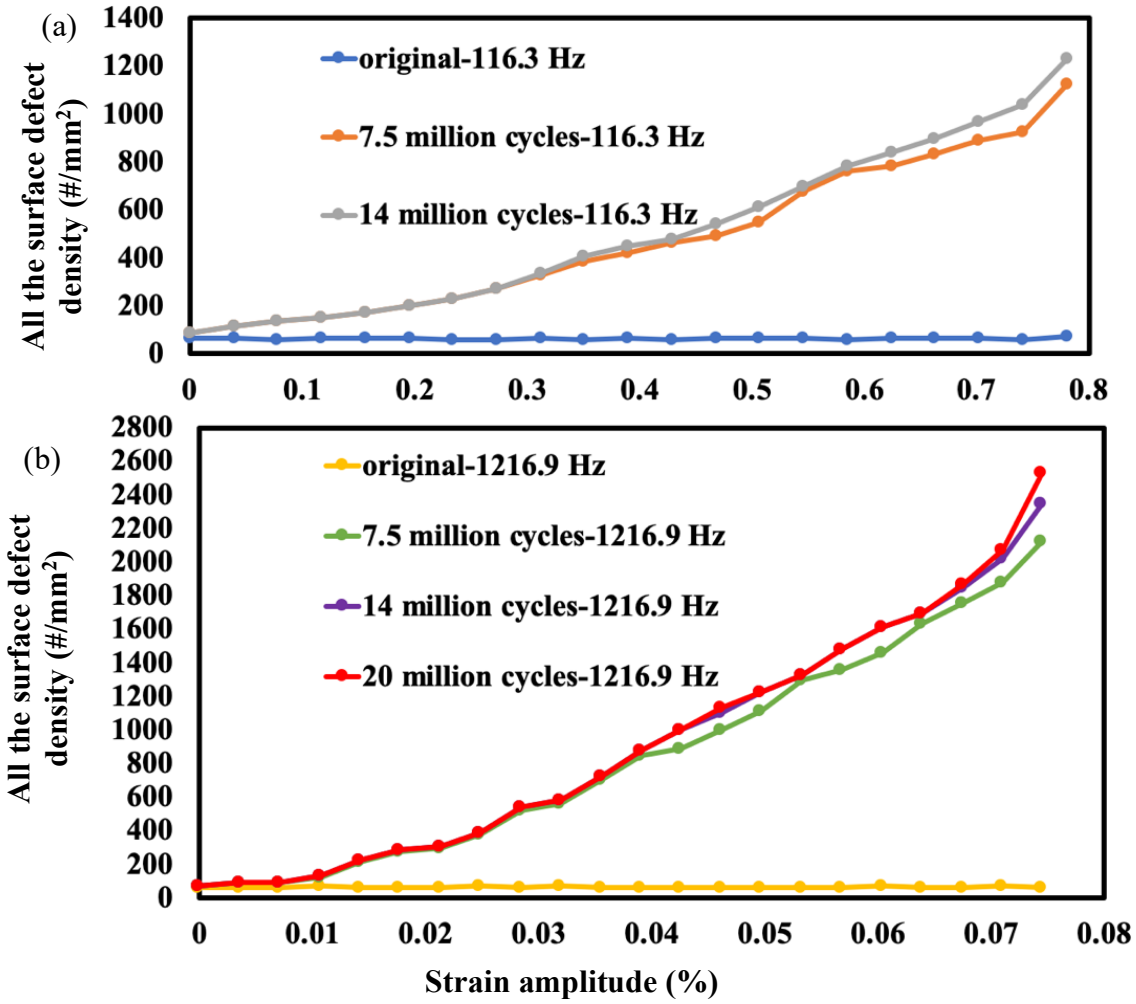


Figure 5.19. The density for all the surface defects along the cantilever (exhibited as strain amplitude) at frequency of 116.3 Hz (a) and 1216.9 Hz (b). The "original" corresponds to the initial defect density before cyclic bending.

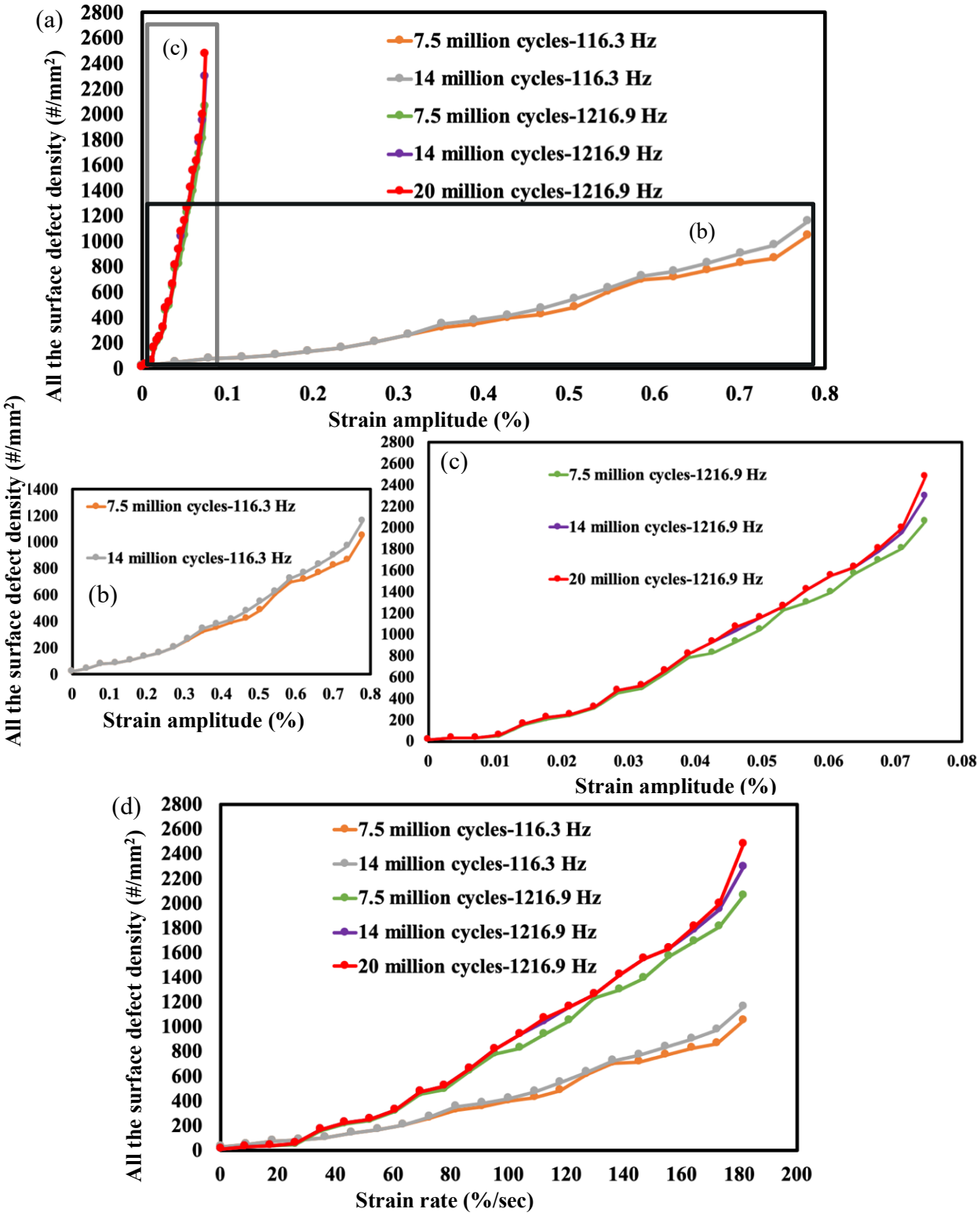


Figure 5.20. All the surface defect density along the cantilever (exhibited as strain amplitude (a)/strain rate(d)) for two different resonant frequencies of 116.3 Hz and 1216.9 Hz. (b) and (c) is the enlarged image showing defect density at 116.3 Hz and 1216.9 Hz, respectively.

The tendency of NW density with increasing number of cycles and strain distribution along the cantilever (Figure 5.21) is similar as that for all the surface defects. The ratio of maximum NW density for these two frequencies (~155/85) is similar to that of maximum all the defect density (~2700/1300) with a value of about 2. There exists a critical strain amplitude of 0.1 % and 0.03 % for NW formation with cyclic frequency of 116.3 Hz and 1216.9 Hz (Figure 5.21 (c) and (d)), respectively. It indicates that high frequency promotes NW formation by decreasing the threshold strain amplitude, consistent with what has been observed for RT experiment (Figure 3.23). The critical strain rate for obvious NW density increase is similar for these two frequencies (Figure 5.21 (b)), with a value of 80 %/sec. This is similar to what has been observed for all the surface defects with strain rate about 25 %/sec to exhibit significant defect formation. There is also similar frequency dependent mechanisms for NWs as shown at RT (Figure 3.23). The smaller value of critical strain rate for all the surface defects than that for NWs demonstrates that NW formation needs higher threshold stress even though the local stress accumulation for NW formation is smaller compared to that for larger surface defects.

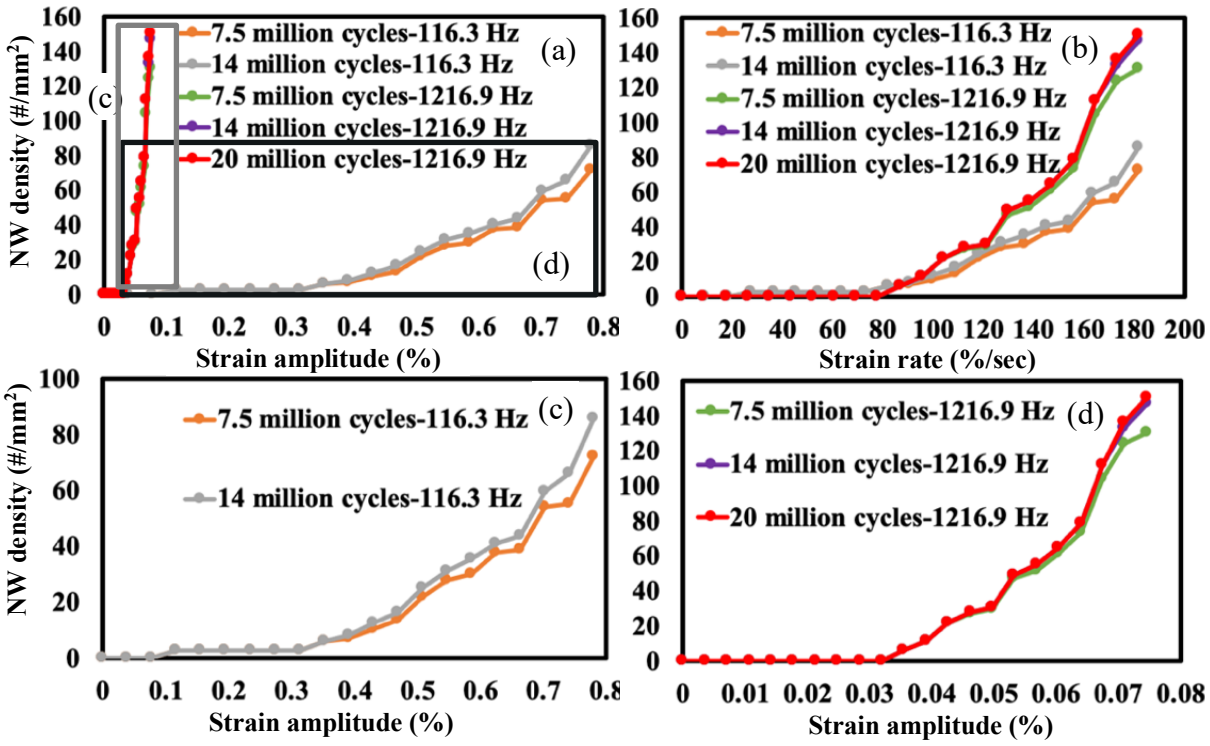


Figure 5.21. NW density along the cantilever (exhibited as strain amplitude (a)/strain rate (b)) for two different resonant frequencies of 116.3 Hz and 1216.9 Hz. (c) and (d) is the enlarged image showing NW density at 116.3 Hz and 1216.9 Hz, respectively.

The density for micro-sized surface defects (Figure 5.22) with the similar ratio of maximum defect density between these two frequencies as for all the surface defects and NWs. The maximum defect density is about 250/mm$^2$ and 450/mm$^2$ for 116.3 Hz and 1216.9 Hz respectively without a critical strain amplitude for defect formation (Figure 5.22 (c) and (d)). This value is an order of magnitude smaller than that for cyclic bending at RT (Figure 4.2), and it reflects the contribution of micro-sized surface defects decreases for low T experiment.

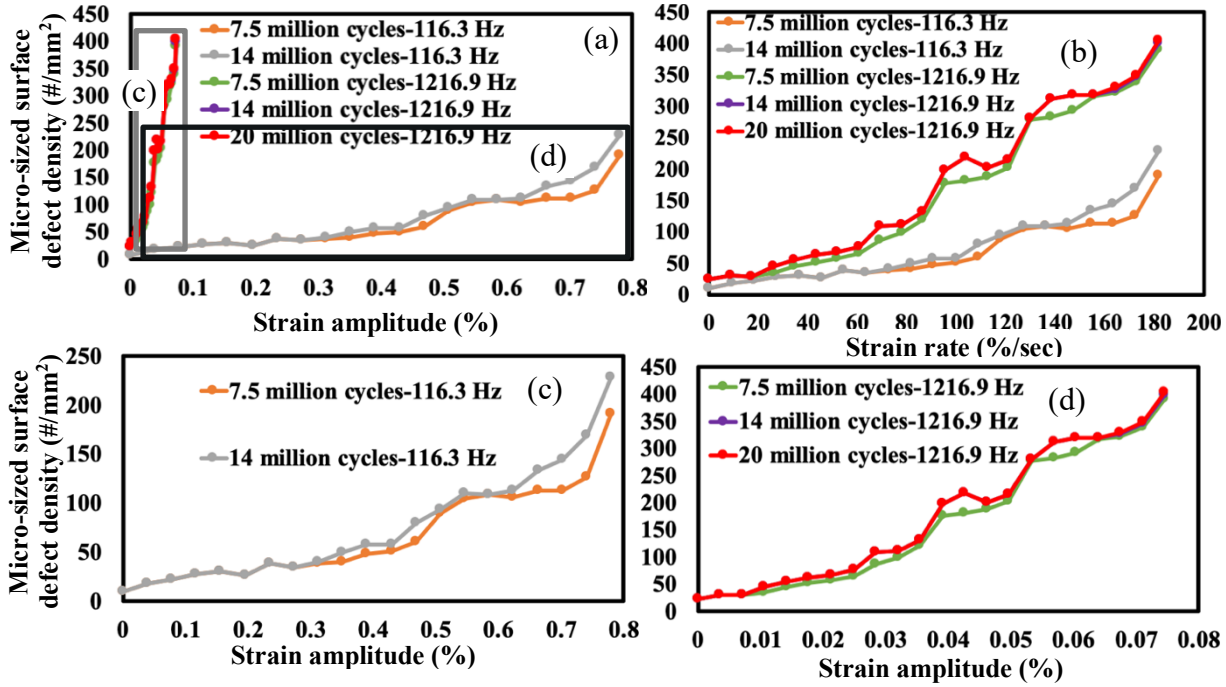


Figure 5.22. Micro-sized surface defect density along the cantilever (exhibited as strain amplitude (a)/strain rate (b)) for two different resonant frequencies of 116.3 Hz and 1216.9 Hz. (c) and (d) is the enlarged image showing micro-sized defect density at 116.3 Hz and 1216.9 Hz, respectively.

The defect density for IGBs is much higher than that for NWs and micro-sized surface defects, and it is the dominated defect morphology for cyclic bending at low T (Figure 5.23). IGBs distribute along the whole cantilever, and the significant IGB density increase happens at strain rate of about 25 %/sec for both frequencies (Figure 5.23 (b)). This is similar to the strain rate for all the surface defect density showing obvious increase (Figure 5.20 (d)). The ratio of the maximum IGB density for these two frequencies is the same as for other defects, and the IGB density is also frequency dependent with higher IGB density for 1216.9 Hz at fixed strain amplitude/rate (Figure 5.23 (c) and (d)). Thus, the resonant frequency is the critical effect for all

kinds of surface defect formation. Combined the analysis from Figure 5.21 to Figure 5.23, it can be concluded that when approaching the free end of the cantilever, there are micro-sized surface defects and IGBs with small strain amplitude/rate, similar to defect formation at RT or during thermal cycling. The nucleation of NWs needs higher strain amplitude/rate which corresponds to positions approaching the fixed end of the cantilever.

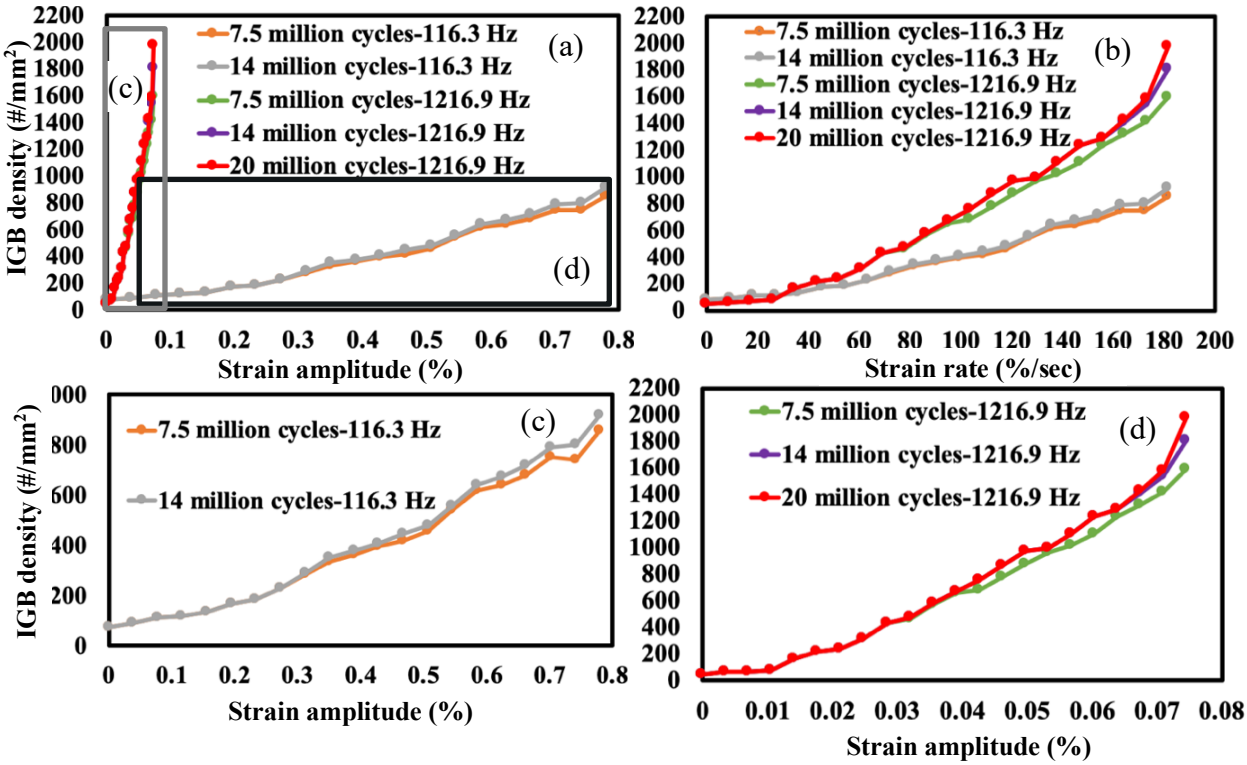


Figure 5.23. IGB density along the cantilever (exhibited as variables of strain amplitude (a)/strain rate (b)) for two different resonant frequencies of 116.3 Hz and 1216.9 Hz. (c) and (d) is the enlarged image showing IGB density at 116.3 Hz and 1216.9 Hz, respectively.

### 5.3.4 Quantitative Analysis of Defect Density on Tin Films for Different Frequencies

Section 5.3.3 talked about the defect distribution during the interrupted cyclic bending for two distinct frequencies, and it is hypothesized that all kinds of surface defects are frequency dependent during low T cyclic bending. To investigate the frequency effect more systematically, two other frequencies of 226.3 Hz and 272.5 Hz are added in this section. All the cantilevers vibrated at these different frequencies are cycled continuously until 7.5M cycles to guarantee the only changing parameter is the resonant frequency. These four frequencies exhibit four distinct

strain amplitude distribution along the cantilever with similar strain rate distribution (Figure 5.24). The maximum strain rate is almost the same for 116.3 Hz, 226.3 Hz and 1216.9 Hz, about 180 %/sec, with smaller value of 170 %/sec for 272.5 Hz. The strain rate distribution for various frequencies in this thesis is in a narrow range of 170-180 %/sec. It indicates that even there exists smaller maximum strain amplitude for higher frequency, the corresponding higher frequency compensates strain amplitude difference since strain rate is a multiple product of strain amplitude and resonant frequency. The coupling of these two factors leads to the similarity of the strain rate distribution no matter what the resonant frequency is.

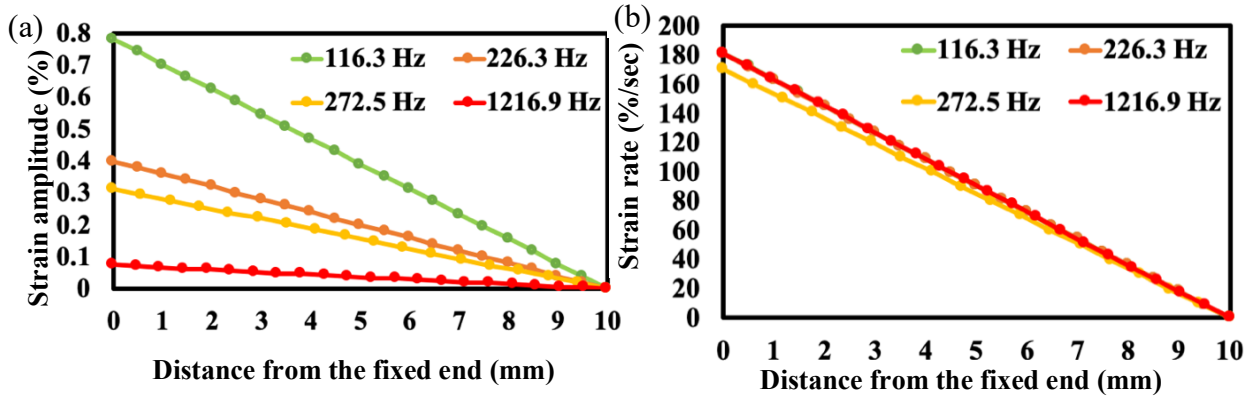


Figure 5.24. strain amplitude (a) and strain rate (b) distribution along the cantilever for four different resonant frequencies: 116.3 Hz, 226.3 Hz, 272.5 Hz and 1216.9 Hz

The surface defect density before and after cyclic bending is exhibited clearly in Figure 5.25. The initial defect density before cyclic bending is similar to guarantee the consistent surface morphology. All the defect density is increasing with larger strain amplitude approaching the fixed end of the cantilever, and the defect density is also frequency dependent at fixed strain rate except for the case of 272.5 Hz. Cyclic bending at 272.5 Hz exhibits similar defect density as that for 226.3 Hz and 1216.9 Hz with strain rate smaller than about 70 %/sec (corresponding to about 40 % of the cantilever from the free end). Then the defect density increase to the fixed end for 272.5 Hz case shows a much smaller slope than the other three frequencies with an ultimate defect density similar to that for cyclic bending at 116.3 Hz.

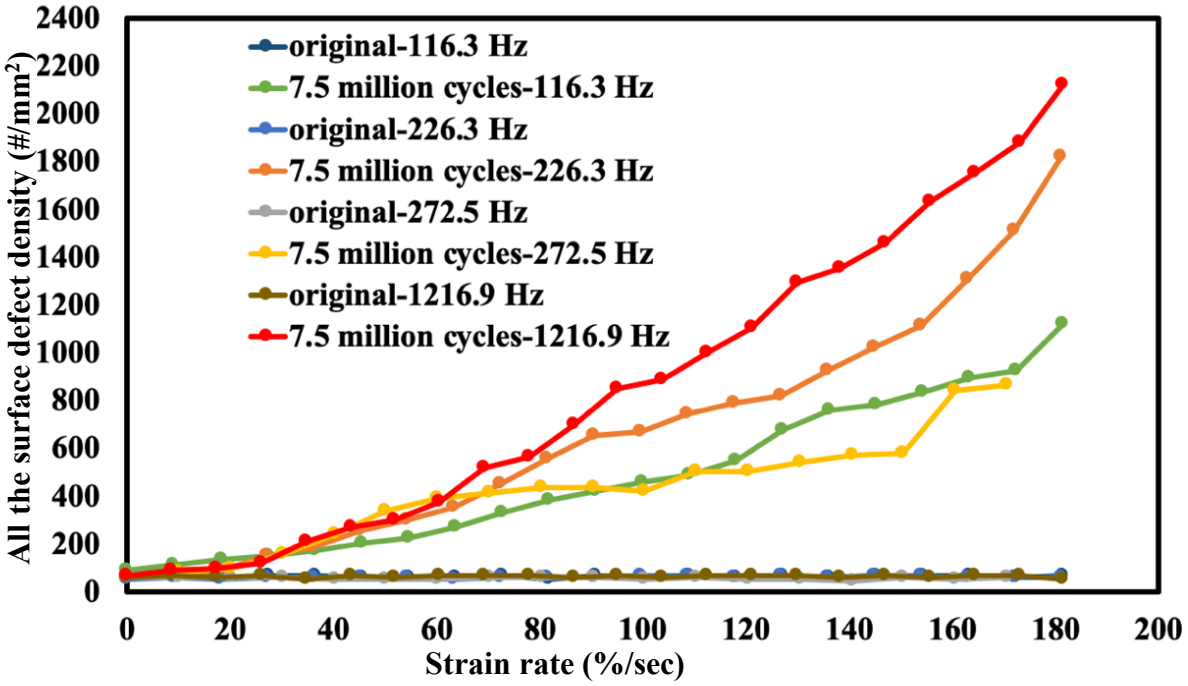


Figure 5.25. All the surface defect density along the cantilever (exhibited as strain rate) for four different frequencies. The "original" corresponds to the initial defect density before cyclic bending.

The density of surface defects formed only during the cyclic bending is shown clearly as a function of strain amplitude (Figure 5.26 (a)) and strain rate (Figure 5.26 (b)). The defect density is frequency dependent except for the case of 272.5 Hz, as already talked in detail in Figure 5.25. The cyclic bending at 272.5 Hz followed this frequency dependent law with the strain amplitude smaller than 0.15 % (Figure 5.26 (a)), which corresponds to about 50 % of the length of the cantilever. The defect density difference between two neighboring frequencies at a fixed strain amplitude increases with the corresponding difference of the frequency value. For example, the defect density difference between 1216.9 Hz and 226.3 Hz is about 1600/mm$^2$ while that between 226.3 Hz and 116.3 Hz is only 90/mm$^2$ at strain amplitude of 0.075 %. This density difference does not follow the same tendency for fixed strain rate with strain rate larger than 100 %/sec where the strain rate effect is distinct for all the frequencies. The defect density difference between 1216.9 Hz and 226.3 Hz as well as 226.3 Hz and 116.3 Hz is almost the same from 50% the cantilever length to the fixed end. It indicates that the frequency dependent influence is more significant for fixed strain amplitude than for fixed strain rate at low T.

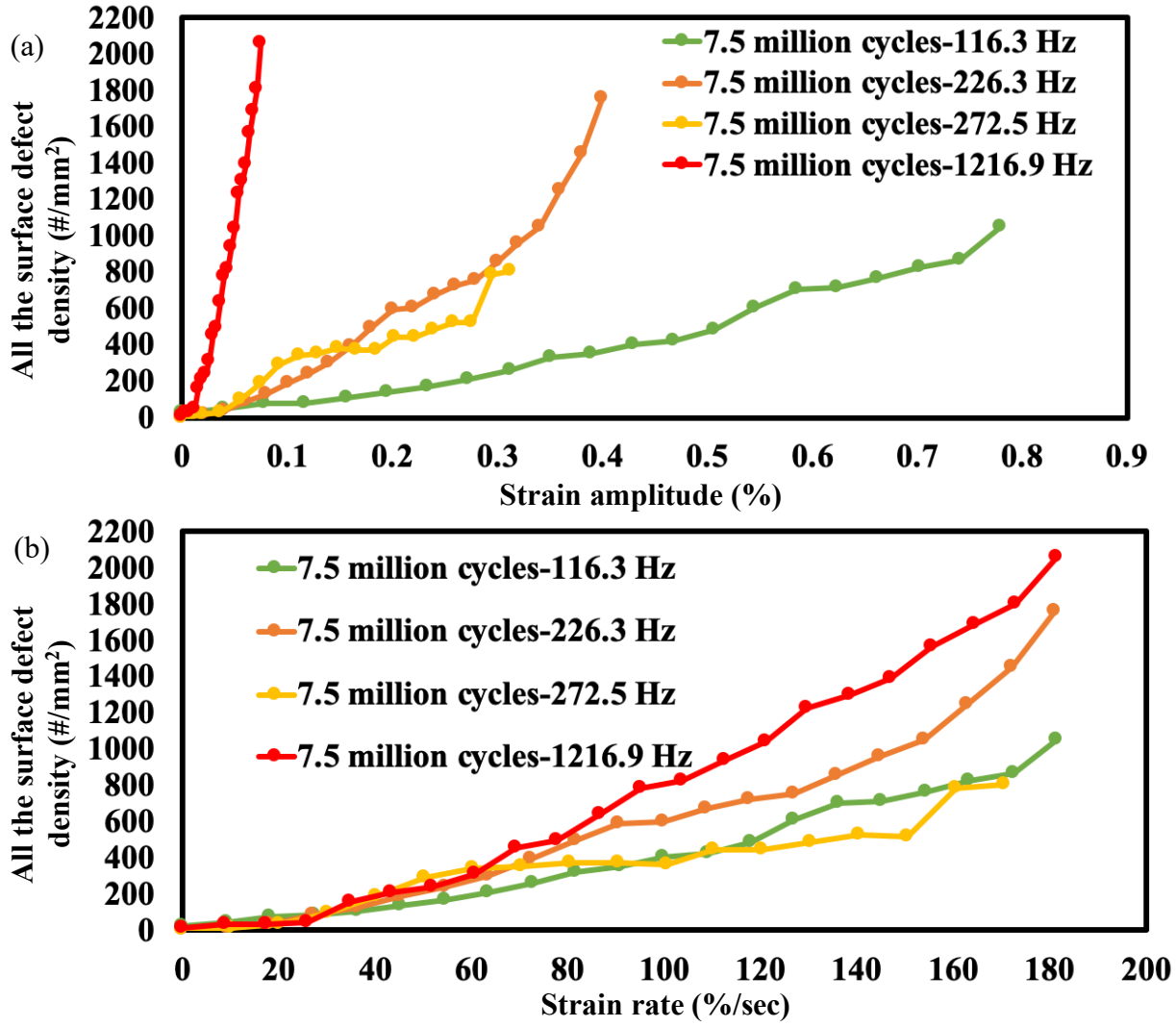


Figure 5.26. Plots of all the surface defect density along the cantilever (exhibited as variables of strain amplitude (a)/strain rate(d)) for four different resonant frequencies

The threshold strain amplitude for the significant NW formation is decreasing with increasing resonant frequency. The value is only 0.05 % for 1216.9 Hz and that for 226.3 Hz and 272.5 Hz is about the same at 0.1 %, while the critical strain amplitude for NW formation is 0.3 % at 116.3 Hz (Figure 5.27 (a)). There are even no NWs formation for the other three frequencies while the strain amplitude has already reached the maximum approaching the fixed end of the cantilever for 1216.9 Hz (with a maximum strain amplitude of ~0.08 %). The critical strain rate for NW formation is the same with a value of 80 %/sec (Figure 5.27 (b)) at all frequencies, and it is consistent with the observation in Figure 5.21. The maximum NW density for 226.3 Hz is about twice as that for 116.3 Hz and it is similar to the ratio between these two frequencies, while the

difference between 226.3 Hz and 1216.9 Hz is only 20/mm$^2$ and 272.5 Hz case has the lowest maximum NW density. Combined the analysis obtained from Figure 5.25, the correlation between NW density and frequency is not as clear as that between all the surface defect density and frequency. It is hypothesized that NW density corresponds linearly with the frequency until some critical frequency value, and the NW density increase for frequencies above this threshold becomes much slower than the change of frequencies leading to an ultimate saturation value for NW density at or above a specific frequency. This can be perspective work for future research investigating cyclic bending behavior of cantilevers at more frequencies.

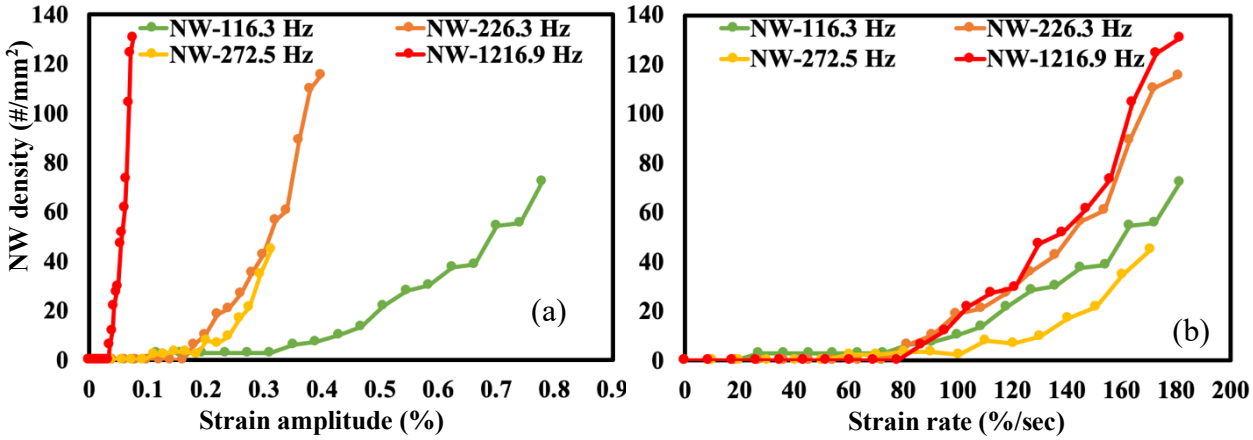


Figure 5.27. Plots of NW density along the cantilever (exhibited as strain amplitude (a)/strain rate (b)) for four different resonant frequencies

The micro-sized surface defect density for cyclic bending at 272.5 Hz is much higher than that for cyclic bending at other frequencies (Figure 5.28). It exhibits a maximum value of over 700/mm$^2$ while the maximum value for other frequencies is only about 400/mm$^2$ at 1216.9 Hz. The micro-sized surface defect density at low T follows the same tendency as that at RT, namely increasing defect density with increasing resonant frequency for the fixed strain amplitude (Figure 5.28 (a)). For the fixed strain rate, the micro-sized surface defect density for cyclic bending at 1216.9 Hz is much larger than that for cyclic bending at 116.3 Hz and 226.3 Hz exhibiting similar defect density distribution along the cantilever until about 20 % of cantilever length from the fixed end. This is consistent with the conclusion that the effectiveness of frequency dependent mechanism becomes obvious with larger strain amplitude/rate.

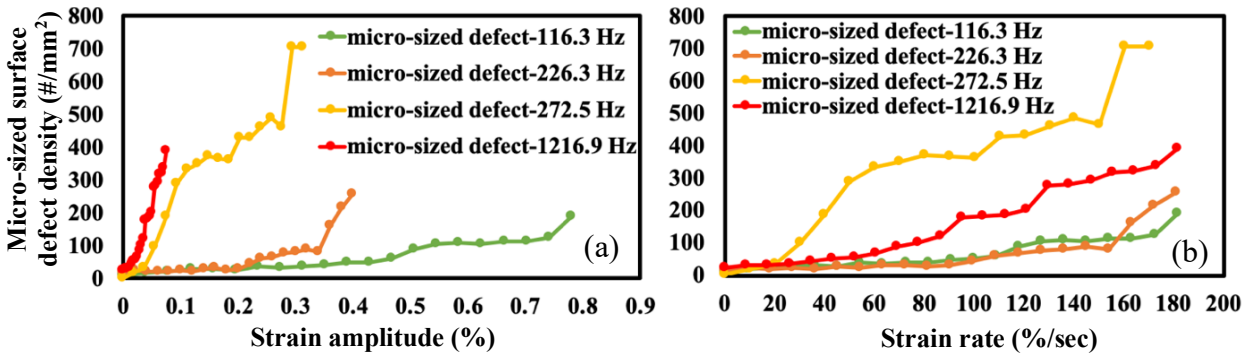


Figure 5.28. Plots of micro-sized surface density along the cantilever (exhibited as strain amplitude (a)/strain rate (b)) for four different resonant frequencies

The IGB density follows the similar defect density distribution as for all the defects (Figure 5.26) at fixed strain amplitude. There is no difference for all the defect density (Figure 5.26 (a)) and IGB density (Figure 5.29 (a)) at 116.3 Hz and 226.3 Hz with strain amplitude smaller than 0.05 %. The IGB density difference between 1216.9 Hz and 226.3 Hz as well as between 226.3 Hz and 116.3 Hz is similar at strain amplitude of 0.075 % compared to that for all the surface defects. It indicates that IGB density evolution follows the same tendency as for all the surface defects except for 272.5 Hz case. The IGB density of 1216.9 Hz and 226.3 Hz derives from that of 116.3 Hz at strain rate of 35 %/sec (corresponds to the position about ~20% of the length from the free end), while the discrepancy of IGB density for 226.3 Hz and 1216.9 Hz happens at strain rate of 90 %/sec (corresponds to the position about ~50% of the cantilever length), as shown in Figure 5.29 (b). It is postulated that the critical strain rate where obvious segregation between two frequencies happens is increasing with increasing frequency. There is no IGB formation from about 80% of the length to the free end (corresponds to a critical strain amplitude/rate of 0.25 % and 140 %/sec) during the cyclic bending at 272.5 Hz, and the IGB density is very small compared to that for the other three frequencies. According to the analysis from Figure 5.25 to Figure 5.29, the defect density always follows the frequency dependent rule for frequencies with similar strain rate distribution no matter what the defect type is for cyclic bending at low T. The cyclic bending at 272.5 Hz shows contradictory low density for IGBs and high density for micro-sized surface defects though they both have grain size in $\mu$m range.

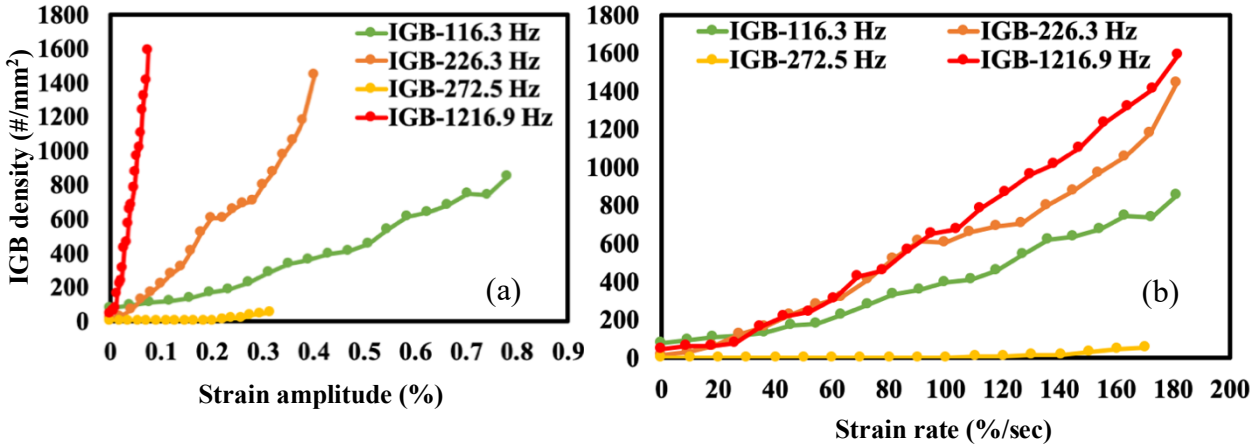


Figure 5.29. Plots of IGB density along the cantilever (exhibited as strain amplitude (a)/strain rate (b)) for four different resonant frequencies

Due to the low IGB density and high micro-sized defect density for low T cyclic bending at 272.5 Hz, it is hypothesized that the sum of these two surface defect types follow the same frequency dependent mechanism due to the similar grain size. To investigate, the defect density besides NWs is exhibited in Figure 5.30. The larger surface defects are frequency dependent from the free end to 50 % of the cantilever length, and then the density at 272.5 Hz shows unusual response with smaller slope of strain distribution. This similar to what has observed for all the surface defect density (Figure 5.26). It is hypothesized that the unusual response from 50 % to the fixed end of the cantilever leads to the discrepancy behavior of cantilevers at 272.5 Hz.

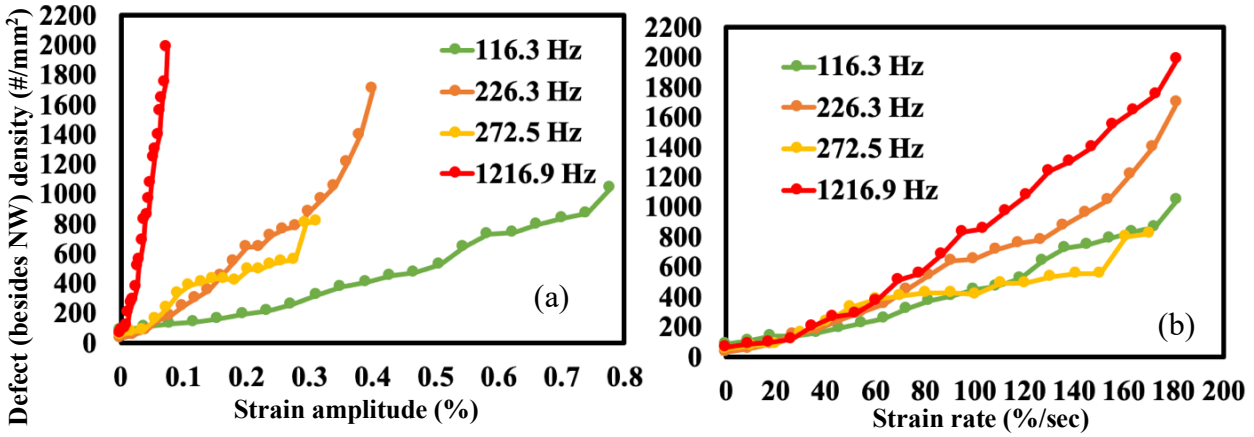


Figure 5.30. Plots of larger surface defect (excluding NW) density along the cantilever (exhibited as strain amplitude (a)/strain rate (b)) for four different resonant frequencies

### 5.3.5 **Discussion**

As exhibited in Chapter 3, the IGB density for cyclic bending at RT at frequencies of 599.38 Hz and 392.5 Hz is very low and a quantitative analysis is not possible. The results for experiments done at 226.3 Hz in this research have shown that there is significant IGB density even without the influence of temperature (Figure 5.16). It is inferred that both low T and low frequency promote IGB formation.

The nucleation and growth for NW is limited to GBs or the extrusions of IGBs with short-range diffusion and mass transport as a response to the repeated rapid transition between tensile and compressive stress during cyclic bending, which is analyzed in detail in Chapter 3. The critical strain accumulation for NW formation is much smaller compared to that for micro-sized surface defect formation. For micro-sized surface defects, the nucleation site is either a pre-existing in-plane grain or a newly formed grain. The growth of micro-sized defects is achieved by the overall lift-up of the defect grain compared to a nucleation site smaller than 1 $\mu$m for NWs.

The situation for IGBs becomes much more complicated compared to that for other surface defects. The open morphology of IGBs is composed of several extrusions and intrusions with porous regions at GBs or in the grain beneath the IGB (Figure 5.13 and Figure 5.14), and some IGBs expand across several in-plane grains especially for low T experiment. It is hypothesized that IGB formation requires more strain energy due to the complicated morphology and larger activating basal area compared to that for NWs and micro-sized surface defects, that only need a limited nucleation area approaching GBs or extrusions of IGBs and only one in-plane grain, respectively. It leads to fewer IGBs with higher required critical strain amplitude to achieve nucleation than other defects at the same strain amplitude before the density of IGBs soars up. An example is that the critical strain amplitude for IGB formation is about 0.125 %, and the IGB density soars up with strain amplitude higher than 0.2 % for cyclic bending at RT (Figure 5.17 (c)). This threshold strain amplitude for IGB formation is higher than that for NWs with a value of 0.1 % at RT (Figure 5.17 (b)). It indicates that the strain amplitude distribution along the cantilever for each cycle during cyclic bending experiment is very important for IGB formation. For experiment done at low frequencies, the slope of the strain amplitude distribution along the cantilever for each cycle is steep with large tip displacement at the free end. It is favored to overcome the large threshold stain amplitude, which increases IGB formation.

The above analysis puts forward the hypothesis for the enhancement of IGB formation due to the low frequency. Now the focus switches to the influence of low T for defect density. Both the more severely damaged surface due to more IGBs after cyclic bending at low T than that at RT and the different defect density for all the surface defects as well as the partitioning between the density of different defect types indicate that temperature has a strong effect on the response of tin films during cyclic bending. The following discussion will firstly focus on the smaller NW density and then switch to the preferred nucleation of IGBs at low T. Increasing creep resistance and decreasing diffusion due to low T plays a role in the underlying mechanism for defect formation.

NWs form near specific GBs due to the local stress state, and they continue to grow and become curved due to the self-weight increase. When the driving force cannot overcome the weight increase of NW with continuing growth after certain number of cyclic bending even with curvature of NWs (Figure 3.14 and Figure 5.7), the NW will break due to the force imbalance as a consequence. NW formation is not strongly dependent on temperature. The smaller density of NWs for cyclic bending at low T is hypothesized to be due to the entire or partial "fall-off" of NWs observed for cyclic bending at low T (Figure 5.10), and this is not observed for cyclic bending for same number of cycles at RT. It is hypothesized that it is related to the evolution of the surface morphology due to low T, as shown clearly on IGB surface (Figure 5.11). The damage on the surface of NWs is difficult to be observed due to the small diameter of NW though it is postulated to be similar to that of IGBs presented here. The flaking of surface layer is detrimental for NWs while it only causes surface damage for larger surface defects. In a previous study on the tensile properties of Sn-6.5Zn alloy, it was found that the ultimate tensile strength (UTS) and yield stress (YS) increases with decreasing temperature resulting from the less significant dynamic recovery process at low T [77]. It is hypothesized that the ductile-to-brittle transition temperature for tin films initials for 223 K used in this research. The UTS and YS for tin films are increasing with decreasing temperature, and tin reaches a ductile-to-brittle transition. The brittleness of NWs at low T facilitates the "fall-off" of NWs compared to that at RT.

The multiple IGBs that is approaching the NW root may influence the local stress state that can facilitate the "fall-off" phenomenon of NWs during cyclic bending. Thus, both damage on NW surface and the local stress state approaching the NW root contribute to the decreasing NW density at low T compared to that at RT. The cracks on the extrusions (Figure 5.11 (d)) due to low T can also change the stress state for a local area with the cracks acting as one kind of stress relaxation

mechanisms that decreases the driving force for NW formation. The surface damage of NWs can be examined by high magnification scanning transmission electron microscopy (STEM) in the future.

As shown in the quantitative analysis (Figure 5.17), there is a transition from micro-sized surface defects to IGBs for low T with the total density of these two kinds of defects constant regardless of the temperature effect (Figure 5.17 (d)). The horizontal striations at the edge of the IGB (Figure 3.17 (b) and (e)) indicate the formation of an initial micro-sized surface defect before IGB formation. IGBs can also develop from in-plane surface grains (Figure 5.8 (c) and (f)). Wrinkles appear on the surface of in-plane grains or pre-existing surface defects as a further response to the increasing stress accumulation during the cyclic bending process. Extrusions grow out of the surface and intrusions grow inside the surface grain corresponding to the traces of the wrinkles acting as preferred sites for damage due to the high local stress state. The extrusions and intrusions can evolve into more complicated morphologies resulting from more wrinkles forming on the film surface with increasing number of cycles.

It is hypothesized that the dominant defect type transition from NWs to micro-sized surface defects to IGBs with increasing number of cycles is due to stress accumulation with the combined process of NW fall-off due to the force imbalance (Figure 5.10) and IGB formation from micro-sized surface defects (Figure 5.4) or in-plane grains (Figure 5.9). One example showing the complete transition from NWs to IGBs is exhibited in Figure 5.12. Systematically checking the early stage of cyclic bending can help reveal the transition between NWs and micro-sized surface defects that is lacking for the present evolution. The formation of NWs, micro-sized defects and IGBs can happen simultaneously across the film with different stages in this transition sequence due to the local stress state, and this contributes to the co-existing of all the surface defects on the film surface after cyclic bending at both RT (Figure 3.4) and low T (Figure 5.2). This transition is caused by the different stress accumulation requirement for different defect formation as mentioned before with increasing stress accumulation for more cycles.

Creep dominates the response for the cyclic bending at RT due to the high homologous temperature (~0.58 T) as discussed in Chapter 3. Creep is still active at low T (223 K, homologous temperature of 0.44) though the plastic deformation becomes more difficult at low T due to the decreasing dislocation mobility. Power-law creep occurs at high homologous temperatures by dislocation glide and maybe climb with increasing temperature. GB sliding can also happen with

plastic deformation occurring by creep. It was found in a previous study that the exponent of power-law creep converges towards -1 at RT due to the high homologous temperature, and decreases at lower temperature [78,79]. It is also hypothesized that the width of the dislocation core and partitioning between edge and screw dislocations that has an effect on dislocation mobility is influenced by temperature [80]. Both more screw dislocations and wide dislocation core that reduce dislocation mobility are enhanced at low T. As a consequence, the yield strength and creep resistance of Sn depending on the strain-hardening behavior increases with decreasing temperature. With the increasing difficulty to relax stress by creep and the fact that grains can easily occur plastic deformation are preferred nucleation site for whiskers [18,19], the intragranular cracks dominate, leading to the transition from micro-sized surface defects to IGBs for cyclic bending at low T. Since low T also promotes PSB formation that leads to extrusions and intrusions on film surface during cyclic deformation [72], this also contributes to the increasing density of IGBs at low T.

The diffusion process to sustain defect growth by mass transport is slower for the low T experiment. The corresponding suppressed creep process leads to the decrease of all the surface defect density at low T (Figure 5.15). It is hypothesized that the surface defect density is always smaller at low T compared to that at RT, no matter what the defect type is. The quantitative analysis shows that this is contrast to what has been observed for IGB density (Figure 5.16 (c)), indicating that the mechanism for IGB formation is somehow different from that for NWs and micro-sized surface defects. It was found previously that there are two stress relaxation mechanisms in Al thin films, namely slow and rapid relaxation [81]. Hillock formation is responsible for the slow relaxation process through long-range diffusion. Coble and Nabarro-Herring creep is the possible mechanism for rapid relaxation by short-range diffusion. Thus, IGBs and micro-sized surface defects are responsible for slow relaxation while NWs correspond to rapid relaxation for the present research. It is hypothesized that the low T influence the two relaxation processes differently though the mechanism for this is unclear.

Temperature is also hypothesized to affect the interface between the film and the Cu layer as well as the IMC formation and distribution. IMC distributes at both the vertical GBs and the Cu-Sn interface for cyclic bending at RT (Figure 3.15), while the IMC only forms at the interface and accumulates at the GB approaching the interface beneath IGBs for low T experiment (Figure 5.13 and 5.14). The IMCs at the interface are scallop-like at RT while the variation in IMC

thickness is small at low T. There are two paths for diffusion, one is GBs and the other is the interface between the film and substrate [82]. Thus, the diffusion at GBs is suppressed at low T according to the cross-section analysis, and it is postulated that this suppressed diffusion leads to the increasing possibility of IGBs with the IMC distribution only at the interface. The porous regions in the film for cyclic bending at low T contributes to the low shear strength between tin films and Cu layer [83], and it is hypothesized to effect the stress relaxation mechanisms. The low T experiment also increases the thermal stress in the film due to the CTE difference between Cu and Sn. And the Si substrate, and also the thermal expansion anisotropy of tin will enhance the local variations in stress. This thermal stress is another source of compressive stress that provides additional driving force for defect formation. This situation is favored for IGBs with more strain energy required for nucleation and larger corresponding area over several grains as mentioned above.

There are no voids at the interface beneath the IGB for both RT (Figure 3.18) and low T cyclic bending experiment (Figure 5.13 and Figure 5.14), and it is quite different from the observations of cyclic bending of other materials systems for the interface beneath the extrusions or cracks [42–44,59]. The movement of dislocations through the whole films is based on the "channeling" mechanism [84]. Annihilation of a couple of edge dislocation with opposite signs creates vacancies along the interface followed by diffusion of vacancies to the surface and GBs [43]. One hypothesis for lacking voids at the interface beneath the IGB is related to the mass transport and diffusion during this process. The voids shown in other cyclic bending studies indicate short-range diffusion directly from the interface to the defect formed on the film surface, and it is different from the proposed long-range diffusion sustaining IGB formation, which is consistent with the mechanism for micro-sized surface defect formation. This can be verified through the cross-section images for both defects (Figure 3.15 (d) and Figure 5.13) that there is always IMC accumulation at the GBs approaching the interface beneath the defects, which indicates the same long-range diffusion for both micro-sized surface defects and IGBs [61]. The long-range diffusion makes it possible to achieve the completed interface in the neighboring region beneath IGBs with the mass transport from areas far away from the IGB region.

The other consideration is that as mentioned in cyclic bending of Cu films on polyimide substrates, for some particular grain orientation of <111>, the dislocations deposited at the interface are all pure screw type, and they do not lead to the voids composed of vacancies [43].

The same mechanism can happen due to the polycrystal structure of Sn film without preferred orientations. For grains near IGB, it is hypothesized that they have specific orientation distribution resulting in pure screw dislocation at the interface. To get the particular orientation, effective EBSD data is needed. It is a prospective aspect for future study.

For interrupted cyclic bending at low T, it follows the same rule that the defect density is negligible after the first interruption. The continuous stress relaxation is the main reason for the limited nucleation of new defects. Compared to the results got for cyclic bending at RT (Figure 4.1), the maximum density difference for all the surface defects between 7.5M and 14M cycles for 600 Hz at RT is similar to that for 116.3 Hz at low T (Figure 5.20 (b)), with a value of 200/mm$^2$. Since the defect density difference between the interruptions at the same number of cycles is smaller for lower resonant frequency (Figure 3.22), it can be inferred that the density difference for 116.3 Hz at RT should be less than 200/mm$^2$. The defect density difference between neighboring interruptions is enhanced by low T.

The formation of larger surface defects excluding NWs is through the primary and secondary stages of typical creep curves before the first interruption (Figure 4.4 (a)) as discussed in Chapter 4, and the suppression effect caused by low T decreases the degree that the film experiences the secondary stage. Thus, when the film is under tension or is static during the interrupted cyclic bending with oxidation formation (Figure 4.4 (b)), the response of some local areas of the film can go back into the primary stage. This contributes to more defect nucleation for the following compressive half cycle with a higher creep rate at the primary stage compared to that at secondary stage, and this contributes to the large defect density difference between interruptions at low T.

Another phenomenon observed for interrupted cyclic bending is that the extent of defect density difference decreases with increasing number of interruptions. It indicates that the process of stress relaxation happens much faster than the accumulation of stress acting as a driving force for defect formation during the compressive half cycle. The difference between the stress accumulation and stress relaxation becomes larger with additional cycles. Once the stress accumulated during the whole process including the initial stress originated from plating process and IMC formation as well as the stress generated during the compressive half cycles is equal to or less than the continuous stress relaxation by defect formation, creep, GB sliding, etc., the driving force for defect formation is too small to activate defect nucleation. This leads to an unchangeable profile for defect density distribution along the cantilever with additional cycles, and it is similar

to the plateau observed for cyclic bending of AFM cantilevers (Figure 2.11). The majority of stress relaxation happens with oxidation layer formation when the film is static. Increasing stress relaxation and thicker oxide layer on film surface with more time the film is not experiencing the cyclic bending process inhibits defect formation without enough stress accumulation. The smaller the interval between each interruption (i.e. more interruptions for the same number of cycles) is, a smaller number of cycles is required for achieving the saturated plateau for defect density.

The unusual response of tin films for cyclic bending at 272.5 Hz compared to that at other frequencies is drawn much attention. One hypothesis is that the response of the film is very sensitive to the strain rate. The slope of strain rate distribution along the cantilever for cyclic bending at 272.5 Hz is obvious smaller than that at other frequencies (Figure 5.24). It is postulated that the transition of dominated stress relaxation response from micro-sized surface defects to IGBs is achieved when the maximum strain rate exceeds some critical value though the mechanism behind this hypothesis is not clear.

The other perspective is the parameters influencing the behavior of the cantilever from 50 % of the length to the fixed end, i.e. the positions that the defect density deviates from the theoretical speculation (Figure 5.26 (b)). The initial surface morphology before the cyclic bending is excluded from the possible factors with the verified SEM images. The cantilever is attached to the piezoelectric piece that is connected to the LDV system with superglue, and the factors during assembly of the installment including adhesion strength, contacting area and the alignment between the cantilever and the piezoelectric piece, etc., can influence the response of the cantilever. The constant low T during cyclic bending is also very critical. Though the temperature is monitored simultaneously by the thermocouple, the fluctuation of temperature due to the storage of $LN_2$ and the distance of the thermocouple from the sample can influence the response of tin films.

The difference between cyclic bending at various frequencies becomes larger towards the fixed end of the cantilever with higher strain amplitude/rate, meaning that the frequency dependent rule for defect formation is more obvious for both RT and low T cyclic bending. The higher the resonant frequency is, the less time is needed to achieve the same number of cycles. The extent of stress relaxation is decreasing with higher frequency due to the less time the film experiences. Since the stress accumulation for the same number of cycles is increasing with higher strain (strain per cycle * number of cycles), the absolute stress accumulation difference between different frequency is larger towards the fixed end, leading to the obvious defect density difference.

## 5.4 **Summary**

In this chapter, the cyclic bending at low T (223 K) was investigated in detail. Large numbers of IGBs show up on the film surface for cyclic bending research at low T. Detailed comparison between cyclic bending at RT and low T was investigated firstly to clarify the influence of temperature. Then the results of interrupted cyclic bending for two frequencies as well as continuous cyclic bending to the same number of cycles for four different frequencies were analyzed in detail. It is similar to what has been done for cyclic bending at RT, and it helps check whether the factors influencing the cyclic bending at RT is the same for low T experiment regardless of the temperature influence. The key points got in this chapter are as follows:

(1) The types of surface defects for low T cyclic bending experiment are still NWs, IGBs and normal micro-sized surface defects, similar to what has been observed for RT experiment. The more complicated morphologies of IGBs with larger corresponding basal area at low T as compared to that at RT indicate more severe surface damage for IGB formation.

(2) Both low frequency and low T promote IGB formation during cyclic bending. Larger maximum strain amplitude for low frequency provides enough stress accumulation to overcome the high critical strain energy required for IGB formation.

(3) The dominated stress relaxation response for cyclic bending at low T are IGBs, followed by micro-sized surface defects with only a few NWs. There are fewer surface defects at low T due to the suppressed creep process by diffusion. The NW density is smaller at low T compared to that at RT, and there is a constant density for larger surface defects excluding NWs at both RT and low T with different partitioning of micro-sized surface defects and IGBs. It is hypothesized that there is a transition from NWs to micro-sized surface defects to finally IGBs for cyclic bending at low T. The decrease in NW density is related to the “fall-off” phenomenon due to NW instability under vibration with surface damage caused by low T. The transition from micro-sized surface defects to IGBs is thought to be related to the higher creep resistance and increasing difficulty to achieve plastic deformation at low T.

(4) There are no voids at the interface between tin films and Cu layer. Two hypotheses are brought up as explanations for this phenomenon: the preferred long-range diffusion to

sustain IGB formation and the particular local grain orientations lead to pure screw dislocations approaching the IGB region.

(5) Both the rules for interrupted cyclic bending and cyclic bending at different frequencies at RT can also be applied to the low T research in this chapter. The defect density increase after the initial interruption is negligible, and the defect density is always frequency dependent for the same number of cycles. The defect density also increases with increasing strain approaching the fixed end of the cantilever at a designated frequency.

(6) The defect density difference between neighboring interruptions is enhanced by low T. It is postulated to be influenced by the early period of secondary stage the films experience before the first interruption due to low T. The gradually decreasing of defect density difference between interruptions with increasing number of interruptions during cyclic bending indicates that the continuous stress relaxation response is faster than the stress accumulation only happen during the compressive half cycle.

(7) The abnormal behavior of cyclic bending at 272.5 Hz is hypothesized to be related to the smaller slope of strain rate distribution compared to that for cyclic bending at other frequencies, and the response of tin films is postulated to be sensitive to the strain rate during cyclic bending. The operation of the experiment and the precision of the temperature control can also influence the behavior of tin films that helps explain the 272.5 Hz case.

# 6. FUTURE WORK

## 6.1 Summary and Impact

A common issue for semiconductor industry is the formation of surface defects on tin films and lead-free solders, causing short circuits and current leakage. While research has been done to investigate the behavior and related mechanisms of tin films under room aging conditions as well as during thermal cycling, there lacks systematic research for tin films with applied mechanical force that is beneficial to provide a guideline for operations of tin films under mechanical stress. Cyclic bending experiment of cantilever is a high-throughput technique with series of strain amplitude/rate along the cantilever for just one experiment set-up. The effect of various parameters can be extracted clearly with cyclic bending at different frequencies and temperature by careful experiment design.

In this thesis, a systematic study on defect formation and evolution during cyclic bending of both AFM and large cantilevers in mm range has been conducted both qualitatively and quantitatively. Mechanical parameters during the cyclic bending including strain amplitude/rate, resonant frequency as well as number of cycles have been investigated in detail for RT and low T environment, respectively. It has also been observed that the interruption during the cyclic bending to follow the surface morphology evolution has a great effect on the nucleation of new surface defects especially on that of larger surface defects excluding NWs.

Films prepared on AFM cantilevers by PVD and electroplating method showed different defect types due to the different film thickness and presence of IMC, and the insufficient strain amplitude along the cantilever leads to the limited nucleation and no additional growth for defects after its initial appearance, as presented in Chapter 2. For cyclic bending of large cantilevers, IGBs and NWs are the new defect morphologies compared to that for tin films under other conditions. The defect density always varies linearly with the strain distribution along the cantilever for a fixed resonant frequency, regardless of the dimension of the cantilevers, the conduct method of the cyclic bending experiment as well as temperature, in consistent with the results from Chapter 2 to Chapter 5. The defect density is frequency dependent for different frequencies both at RT in Chapter 3 and at low T (223 K) in Chapter 5. The comparison between interrupted and continuous cyclic bending reveals the effect of continuous stress relaxation and oxide formation on film surface based on the

typical creep curve in Chapter 4. IGBs are the dominated stress relaxation response at low T due to the more severe damage of film surface and creep resistance, which has been analyzed in detail in Chapter 5. The different active area as well as mass transport and diffusion coefficient for different defect types determine their partitioning, as discussed consistently from Chapter 3 to Chapter 5 for cyclic bending of large cantilevers. It can be concluded that the small strain amplitude/rate along the cantilever, interruptions during cyclic bending, decreasing number of cycles as well as low T inhibit defect formation during cyclic bending based on the analysis from the entire thesis. All these factors should be taken into consideration for design of tin films for cyclic bending applications in the future.

While the research described in this thesis is the first work focusing on the various mechanical parameters and temperature influence in the cyclic bending experiment with the consideration of pre-existing mechanisms for defect formation, including grain geometry, IMC formation, GB sliding and creep, there is still several prospective work needs to be done to provide a more systematic understanding of tin films during cyclic bending. The prospective work includes tracking evolution of local grain orientation where defect forms during the cyclic bending process, analyzing the effect of GB geometry for the defect formation, and investigating the effect of film thickness and surface roughness on cyclic bending experiment.

## 6.2 Global and Local Grain Orientation for Defect Formation

As mentioned earlier, the microstructure of the film with different preferred grain orientations have significant effect on the stress state of the film and thus the response of tin films during the cyclic bending [15,17,34]. It is found that the spread of dislocation core is different for films with different preferred grain orientations [80], and this influences defect formation that is driven by dislocation accumulation. The global and local grain orientations as well as stress and strain gradient are needed to get a better understanding of surface formation during cyclic bending. One effective way to check the grain orientation evolution is by EBSD [16]. The preferred orientation for defects and their relationship with the surface grain and the corresponding neighboring grains as well as the GB misorientations by Mackenzie distribution during the cyclic bending can be decided with this technique.

The issue with this technique is that the as-prepared electroplated films are too rough to get enough indexed points in EBSD measurement. The low yield stress of Sn also increases the

possibility of recrystallization even with very gentle mechanical polishing [23]. One alternative method to decrease the roughness of the film is by ion polishing. The film surface is gently bombast by ions with low accelerating voltage similar to the mechanism of FIB, minimizing damage to film surface. Some preliminary EBSD data (Figure 6.1) shows that there is good agreement between SEM images and orientation maps for the as-prepared films after ion milling. There is no preferred orientation for the initial film, and both high and low angle GBs distribute through the film. The dominated large-angle GBs for the as-prepared films (Figure 6.1 (d)) facilitates crack initiation at GBs by PSB impingement [72], and it leads to IGB formation which is influenced by GB misorientation angle as discussed in Chapter 3, indicating that the ratio and partitioning of different GBs play a role in determining surface defect formation during cyclic bending.

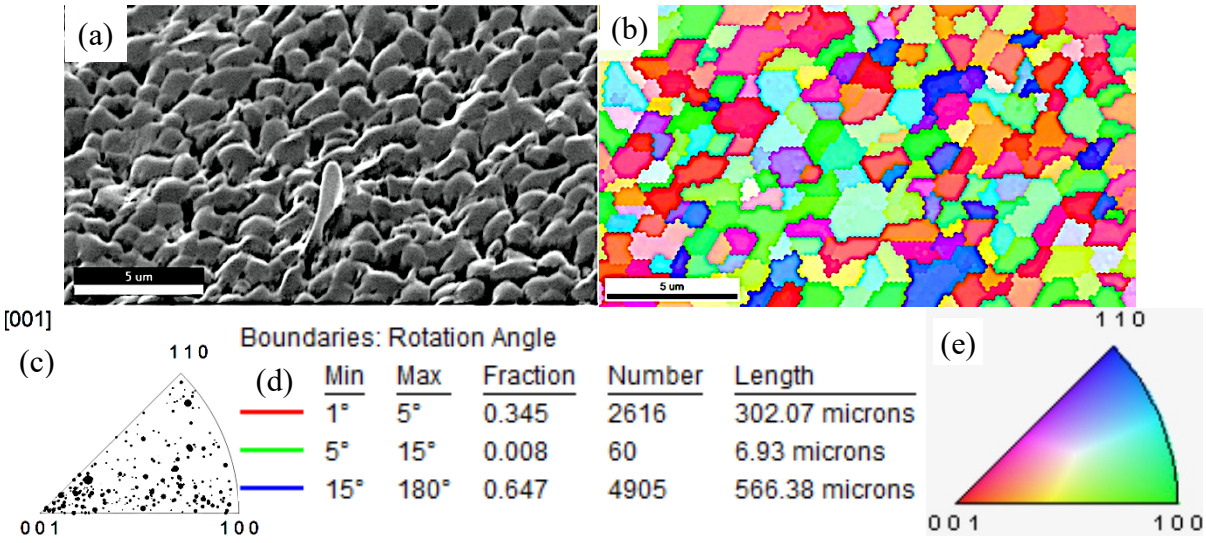


Figure 6.1. (a) SEM image; (b) corresponding normal direction (ND) grain orientation map; (c) inverse pole figure; (d) GB rotation angle distribution; (e) color triangle showing the orientation in fig. (b) for the same random selected area on tin films

While ion milling helps provide reliable EBSD data for cyclic bending with a much larger milling area than that for FIB, there are still some issues with this technique. One is that contrast to FIB that the milling area can be observed clearly through the real-time SEM, the exact area where the surface is milled cannot be located during ion milling without the real-time imaging. This increases the difficulty to position the area that is interested in, such as the area approaching the fixed end of the cantilever with the most severe defect evolution. The ion polishing process also changes the surface roughness even with the minimum damage, and it may be a critical factor

influencing the defect density as similar to the influence of substrate roughness [85–87]. The film damage after the cyclic bending is usually very severe for areas with high strain amplitude/rate and resonant frequency. It is especially difficult to get the effective EBSD mapping for IGBs with highly complicated morphology and NW with a very small diameter and nucleation site. Point analysis is an alternative method to get the orientation relationship for highly damaged area.

Synchrotron micro-diffraction is another method to measure local grain orientation and elastic strain for a large area before and after the cyclic bending [15,24,78]. The elastic strain energy density (ESED) can also be calculated from the measured local strain with the plane stress assumption. This can help identify stress relaxation area with lower ESED. The evolutions of local grain orientation and GB sliding as well as geometrical necessary dislocation (GND) can be determined by x-ray synchrotron without damage to film surface. Since the beam resolution of synchrotron micro-diffraction should be much smaller than the grain size (1-5 $\mu$m in this research), it becomes more difficult to achieve NW orientation with higher beam resolution requirement. The penetration depth of x-ray is also larger than that of electrons, and it can generate information for Cu layer and substrate besides Sn surface grains, increasing the inaccuracy of the data obtained. Thus, doing ion milling with more gentle voltage and doing synchrotron for samples with a larger grain size is some work can be considered in the future.

## 6.3 **GB Geometry for NWs**

As mentioned earlier, the GB geometry is very important for surface defect formation due to its influence on mass transport mechanism to sustain defect growth [12,34,88]. Multiple GB geometry for micro-sized surface defects and IGBs revealed by FIB cut have been shown in the thesis, while only one GB beneath the NW is shown (Figure 3.15 (b)) due to the difficulty to locate the NW. It does not show the exact nucleation site of the NW and it fails to verify the small curvature hypothesis mentioned in Figure 3.25. If cantilevers with large grain size can be prepared, a sequence of NWs formed along a very long GB is an expected consequence. Then multiple cuts can be done along the GB thus increases the possibility to hit the root of NWs. The evolution of cross-section grain orientation can also be obtained before and after cyclic bending since the cut at GB has negligible influence for cyclic bending process with the length of GB in mm range. Chen et al [88] prepared SAC 305 sample with mm-sized in-plane grains by using a standard multi-zone reflow profile in a commercial Pb-free reflow sample. The surface morphology of a GB

(Figure 6.2 (a)) and the corresponding vertical (Figure 6.2 (b)) and inclined GB (Figure 6.2 (c)) show the GB difference for different surface damages. The critical point for this idea is to find the appropriate reflow profile for tin films.

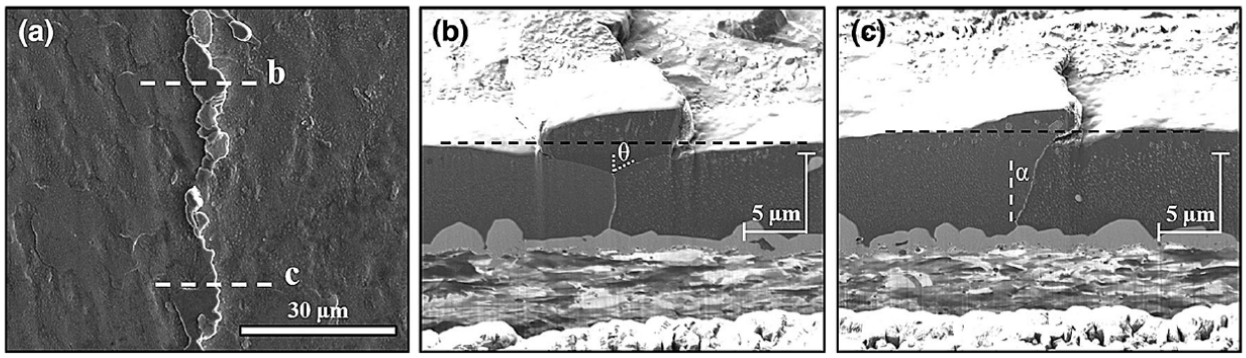


Figure 6.2. (a) SEM image shows surface defects and GB sliding. FIB images (Cut location indicated by dashed lines in (a)) show that (b) a vertical GB plane beneath the shallow surface defect, (c) inclined GB beneath the GB sliding. From JOM, vol. 68, no. 11, Chen et al, "Heterogeneous Stress Relaxation Processes at Grain Boundaries in High-Sn Solder Films: Effects of Sn Anisotropy and Grain Geometry During Thermal Cycling", pp 2888-2899, copyright 1996, with permission from Springer. [88]

A simple trial for obtaining large-grained samples is by heating the as-prepared samples to the temperature just above Sn melting temperature (for example, 520 K) and then cooled down immediately after aging for a very short time at that temperature. The heating process leads to the melting of the film and the cooling leads to the rearrangement of Sn atoms during the solidification process, like a simplified reflow process. Another approach is heating the sample to the temperature just beneath the melting temperature (such as 500 K), causing grain growth due to the temperature influence. A layer of flux is applied on the film surface as protection with the whole experiment is done in open atmosphere, and a detailed process for this is shown in Figure 6.3.

The recrystallized film after reheating to 520 K is uniform with a grain size of ~ 2 $\mu$m, and it is similar to that for electroplated films with less roughness (Figure 6.4). Many pores distributed within the grain resulting from the heating-cooling process. Limited numbers of IGBs are the only defect morphology can be seen on the film surface with random distribution along the cantilever. Compared to the IGB morphology during cyclic bending at RT and low T, many extrusions of the IGB in this experiment are still in-plane of the film with a smaller radius. A NW is also developing

from the extrusion of the IGB (Figure 6.4 (b) and (d)), and it is similar to NW formation from IGB extrusions as discussed before.

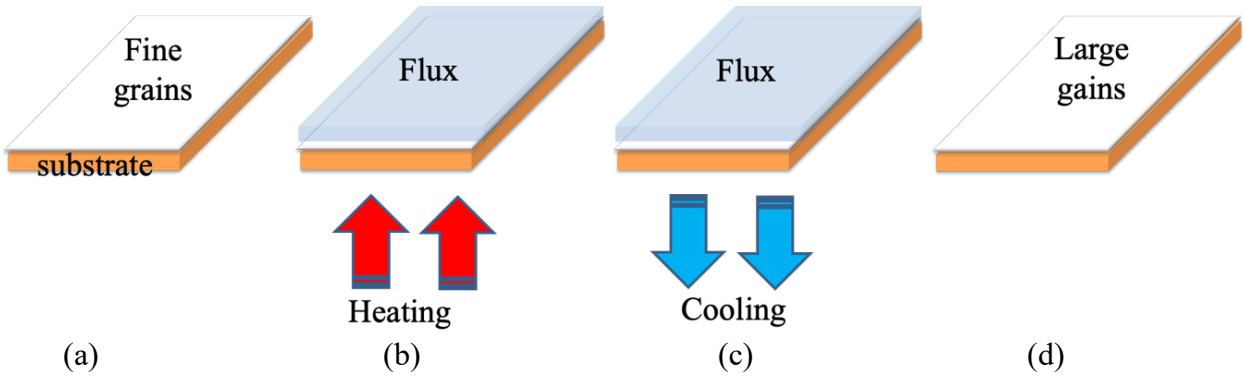


Figure 6.3. A series of schematics shows the proposed preparation process for large-grained films. (a) electroplated fine-grained films; (b) heating process on the hot plate with flux protection; (c) cooling process with the sample taken off the hot plate; (d) the desired large-grained film with flux washed away. The whole process is conducted in the open atmosphere.

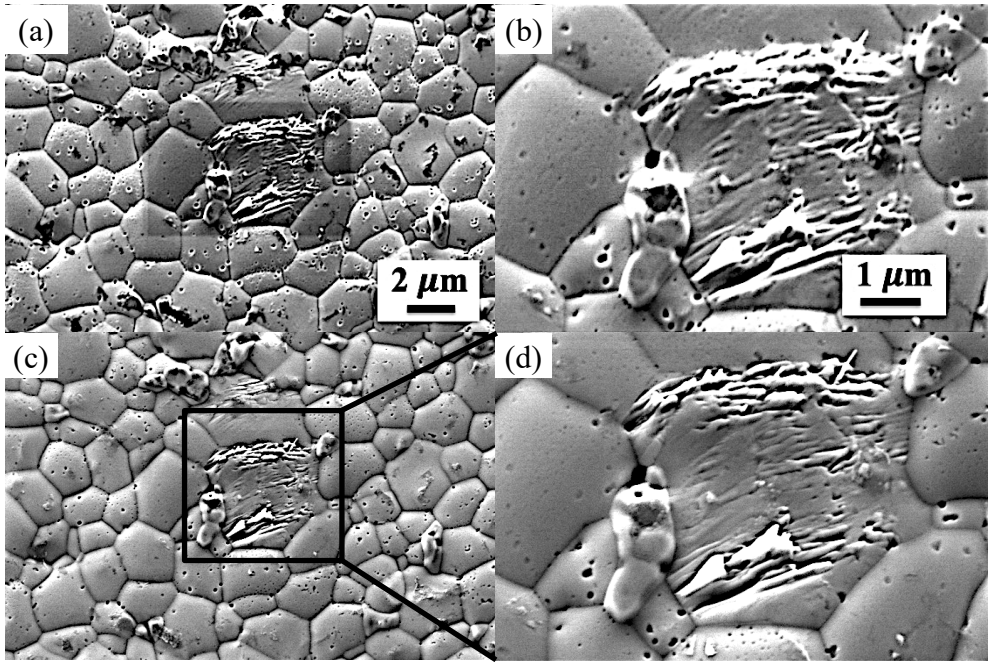


Figure 6.4. SEM images of morphology for electroplated tin films in the same area with process of reheating to 520 K during cyclic bending. (a), (b) after 3.24M cycles; (c), (d) after 5.4M cycles. (b), (d) is the enlarged image of the area of fig. (a), (c), respectively

When the heating temperature is below the melting temperature (~500 K), the grain size is similar as for as-prepared electroplated films or films experiencing melting (Figure 6.5). The film roughness decreases further as compared to recrystallized films without pores. The response of the film is mainly defects growing out of the sunken areas with the progression of GB showing clearly through the traces. This is similar to what has been observed for whiskers [30]. It confirms that GB sliding occurs in defect formation process as a result of coupling between shear stress and GB migration. Additional cyclic bending shows continuous evolution of GB detours, as seen clearly comparing Figure 6.5 (c) with (f). There still lacks clear relationship between defect distribution and strain amplitude/stress along the cantilever. Defect density for both recrystallized films and films aging below the melting temperature is much smaller compared to that for electroplated films. It is hypothesized that GB geometry and migration, mass transport as well as corresponding diffusion is influenced by the heat treatment process, and it posed effect on the defect types during cyclic bending. The unclear relationship between the position along the cantilever and defect density is also postulated to be due to stress accumulation and relaxation influenced by the heating and cooling process the film experiences.

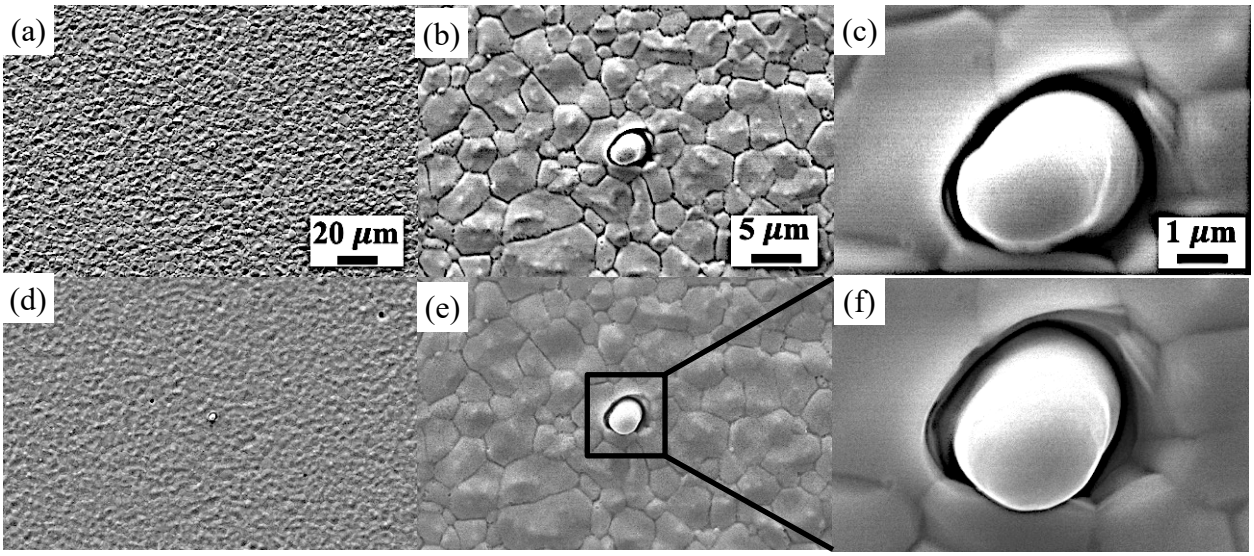


Figure 6.5. SEM images of morphology for tin films in the same area with process of reheating to 500 K during cyclic bending. (a), (b), (c) after 3.24M cycles; (d), (e), (f) after 5.4M cycles

Both the present recrystallization and grain growth method do not work for the idea of large-grained films. For recrystallization process, the reflow process for Sn needs to be redesigned to

find the appropriate parameters. For grain growth condition, insufficient time for sample to stay at 500 K to complete grain growth is proposed to be the main reason for the similar grain size as for electroplated films.

## 6.4 Effect of Film Thickness and Morphology on Cyclic Bending Experiment

For the present study, three kinds of cantilevers are used: PVD AFM cantilevers, electroplated AFM cantilevers and large cantilevers in mm range. It is well known that the grain size corresponds to the film thickness for film deposition process, and thicker films always have a larger grain size for the same deposition conditions. Table 6.1 summarizes the film thickness and grain size as well as IMC formation for the different samples in the research.

Table 6.1. Grain size and film thickness for different samples in this research

| Samples | PVD AFM cantilevers | Electroplated AFM cantilevers | Large cantilevers |
|---|---|---|---|
| **Grain Size ($\mu$m)** | 1 | 3 | 2~5 |
| **Film Thickness ($\mu$m)** | 1 | 12 | 5 |
| **IMC** | No | Yes | Yes |

There have already been research focusing on the influence of film thickness for cyclic bending of other materials. For the cyclic bending of Cu films on silicon nitride AFM cantilevers [36], the dominate damage for sub-100 nm thick films is the formation of GB grooves while that for the 200 nm and thicker films is the formation of twin boundary (TB) extrusions. The stress-strain curves for Cu films with different film thickness on polyimide substrates show that the maximum stress is 300 MPa for 0.8 and 3.0 $\mu$m film exhibiting very similar stress/strain behavior while that for 0.4 $\mu$m film is much higher with a value of 420 MPa [43]. The surface SEM images and FIB analysis reveal that there are more extrusions in the thicker films. The ratio of extrusion height to original film thickness is also smaller in thicker films though the absolute extrusion height is larger than that for thin films. All these show that the film thickness influence the defect types and damage conditions for films during cyclic bending.

As mentioned in Chason's study [50], film thickness influences IMC volume and stress as well as whisker density for room aging experiment which can also pose an effect for cyclic bending experiment due to different driving force for defect formation on films with different thickness. It

has already been discussed in Chapter 2 that one hypothesis for the different response of PVD and electroplated film is due to the film thickness. The same “etching-back” method [50] can be used to etch the film back to the same film thickness, and the comparison between PVD and electroplated films can be done again eliminating the film thickness difference. Similar experiment for films on large cantilevers with same grain size but different film thickness can also help separate the independent influence of grain size and film thickness for cyclic bending experiment, indicating the critical factor for defect formation during cyclic bending besides the mechanical parameters. This can be prospective work for the future.

There have already been several previous studies focusing on the influence of substrate roughness [23,85,86]. It is concluded that the whisker density is lower for films prepared on rougher substrates. This is related to the morphology of the IMC layer. The less compressive stress from the more uniform IMC layer at the interface between rougher substrate and film decreases the driving force for defect formation. The response of the film also varies for films with different surface morphologies and roughness due to the heat treatment the film experiences, as shown in Chapter 2 for PVD and electroplated AFM cantilevers as well as in section 6.3. It is hypothesized that the preparation method and heat treatment have effect on the stress state of the film highly depending on the IMC distribution and morphologies. More systematic work on this can provide some guidelines for designing the film morphology determined by preparation methods to inhibit the proposed risk of tin films during cyclic bending.

# APPENDIX A. MODULUS EFFECT ON THE STRAIN DISTRIBUTION ALONG THE CANTILEVER

The modulus of Si <111> is $E_{Si}$ =169 GPa and that of Sn is in the range of 41~45 GPa, and Sn may exhibit plastic deformation with stiff Si substrate beneath it even at small strain amplitude due to the obvious modulus difference. For large cantilevers in mm range, the effect of tin films can be negligible due to much thinner layer of Sn compared to Si substrate. For AFM cantilever, the thickness of the film is comparable to the thickness of the substrate in the same magnitude. It is always a concern that the strain distribution along the cantilever varies with the onset of plastic deformation for tin films. Here, a simple assumption was used to check the influence of modulus drop of tin films due to the plastic deformation.

The theory used is just the reverse of what is shown in [44]. The free vibration of the cantilever was converted into an equivalent constant force $P_z$ at the free end of the cantilever with relationship between $u_z^{max}$ and $\varepsilon_a(x)$ :

$$u_z^{max} = \frac{P_z x^2 (3L-x)}{6EI} \quad \text{Eq. B-1}$$

$$I = \frac{wt^3}{12} \quad \text{Eq. B-2}$$

$$\varepsilon_a(x) = \frac{3u_z^{max} t}{2L^3}(x-L) \quad \text{Eq. B-3}$$

$$t = t_{Si} + t_{Sn} \quad \text{Eq. B-4}$$

$$EI = \frac{E_{Sn} t_{Sn}^3 + E_{Si} t_{Si}^3}{12} * w \quad \text{Eq. B-5}$$

Where $w$ is the width of the AFM cantilever, and $w$ = 50 $\mu$m. $E_{Sn}$ is selected as the average reported in the literature, and $E_{Sn}$ = 43 GPa. $t_{Si}$ = 2 $\mu$m and $t_{Sn1}$ = 1 $\mu$m for PVD tin films and $t_{Sn2}$ = 12 $\mu$m for electroplated tin films. $I$ is the second moment of inertia. It can be concluded that the strain along the cantilever $\varepsilon_a(x)$ is determined by the EI difference with other constants. Thus, the influence of modulus will be discussed through the value of $EI$ as shown in Eq. B-5.

$$EI_1 = \frac{E_{Sn1} t_{Sn2}^3 + E_{Si} t_{Si}^3}{12} * w = (43*1^3+169*2^3)/12*50*10^{-15} = 6*10^{-12}$$

$$EI_2 = \frac{E_{Sn2} t_{Sn2}^3 + E_{Si} t_{Si}^3}{12} * w = (43*12^3+169*2^3)/12*50*10^{-15} = 3.15*10^{-10}$$

Assume Sn modulus drops 5 % $E_{Sn}$ =(1-5 %) *45=40.85 GPa

$$EI_1 = \frac{E_{Sn1} t_{Sn2}^3 + E_{Si} t_{Si}^3}{12} * w = (40.85*1^3+169*2^3)/12*50*10^{-15} = 5.80*10^{-12}$$

$$EI_2 = \frac{E_{Sn2}t_{Sn2}^3+E_{Si}t_{Si}^3}{12} * w = (40.85*12^3+169*2^3)/12*50*10^{-15}=3.00*10^{-12}$$

*EI* difference for PVD tin films is (6-5.80)/6=3.33 % and *EI* difference for electroplated tin films is (3.15-3)/3.15=4.76 %.

Assume Sn modulus drops 10 % $E_{Sn}$ = (1-10 %) *45=38.7 GPa

$$EI_1 = \frac{E_{Sn1}t_{Sn2}^3+E_{Si}t_{Si}^3}{12} * w = (38.7*1^3+169*2^3)/12*50*10^{-15}=5.79*10^{-12}$$

$$EI_2 = \frac{E_{Sn2}t_{Sn2}^3+E_{Si}t_{Si}^3}{12} * w = ( (38.7*1^3+169*2^3)/12*50*10^{-15}=2.84*10^{-12}$$

E*I* difference for PVD tin films is (6-5.79)/6=3.5 % and *EI* difference for electroplated tin film is (3.15-2.84)/3.15=9.84 %. Since the *EI* difference is still less than 10 % even with the modulus drop of Sn by 10 %, it confirms that the strain distribution along the cantilever does not change much even with plastic deformation of tin films for AFM cantilevers.

# APPENDIX B. THERMAL ENERGY GENERATED BY CYCLIC BENDING

Since the cyclic bending experiment involves the repeated quick transition between tension and compression, energy is generated in this process and it can lead to temperature fluctuation. If obvious temperature increase happens, this can have significant influence on cyclic bending by evolving the effect of CTE mismatch. It is reasonable to check the approximate energy generated in the process to decide if the thermal effect can be negligible.

With the relationship shown in Eq. B-6 between tip displacement and force, the actual cyclic bending process can be transferred into a simplified point bending problem shown clearly in Eq. B-6.

$$u_z^{max} = \frac{P_z L^3}{3EI} \rightarrow P_z = \frac{3EIu_z^{max}}{L^3} \quad \text{Eq. B-6}$$

With the modulus of Si <111> is $E_{Si}$ = 169 GPa and the definition of *I* in Appendix. A, the stress along the cantilever generated by this equivalent stress $\sigma_z^{surf}(x)$ and the corresponding internal energy *U* are shown clearly in Eq. B-7 and B-8. The maximum displacement at the free end $u_{z1}^{max}$= 0.3236 mm and $u_{z2}^{max}$= 0.5064 mm measured by LDV system for 599.38 Hz and 392.5 Hz, respectively was used as an example to check the maximum temperature (T) difference during cyclic bending.

$$\sigma_z^{surf}(x) = \frac{P_z(x-L)t_{sub}}{2I} \quad \text{Eq. B-7}$$

$$\mathrm{U}=\int_0^{10} t_{sub} w \frac{\sigma_z^{surf}(x)2}{2E} x dx = \mathrm{d}\int_0^{10} t_{sub}^3 w \frac{9Eu_z^{max}2}{8L6}(x^3 - 2Lx^2 + L^2x)\mathrm{dx}$$

$$= \frac{9Eu_z^{max}2}{8L6}\ t_{sub}^3 \mathrm{w}\left(\frac{x^4}{4} - \frac{2Lx^3}{3} + \frac{L^2x^2}{2}\right)\Big|_0^{10} \quad \text{Eq. B-8}$$

$$U = nRT \rightarrow T = U/nR \quad \text{Eq. B-9}$$

Here *n* is the amount of substance (in moles) and R is the gas constant (8.31J·K$^{-1}$·mol$^{-1}$). For tin films, assuming the film thickness is 5 $\mu$m and the density of tin is $\rho_{Sn}$ = 7.31 g/cm$^3$, the total mass of tin film $m_{Sn}$ is about

$$m_{Sn} = \rho_{Sn} V_{Sn} = 7.31 \cdot 5 * 10^{-4} \cdot 1 \cdot 0.2 = 7.31 * 10^{-4}\ \mathrm{g}$$

thus $n = \frac{m_{Sn}}{M_{Sn}} = \frac{7.31 * 10^{-4}}{118.71} = 6.16 * 10^{-6}$ mol, and this can be used in Eq. B-9 to determine T.

According to Eq. B-8, the corresponding $U$ are $U_1 = 6.4303*10^{-8}$ J and $U_2 = 1.5747*10^{-7}$ J for 599.38 Hz and 392.5 Hz, respectively. With the correlation between $U$ and temperature change $T$ shown in Eq. B-9, $T$ can be decided as $T_1 = 0.0104$ K and $T_2 = 0.0256$ K, respectively.

The minor temperature change for each cycle guarantee that the effect of T can be neglected for this research. Though there exists energy accumulation for increasing number of cycles, the open-atmosphere experiment and ongoing stress relaxation makes the ignorance of temperature influence reasonable.

# LIST OF REFERENCES


[1] B.Z. Lee, D.N. Lee, Spontaneous growth mechanism of tin whiskers, Acta Mater. 46 (1998) 3701–3714. https://doi.org/10.1016/S1359-6454(98)00045-7.

[2] S. Arnold, K. Compton, A. Mendizza, Filamentary growth of metal surface-Whiskers. Corrosion. 7 (1951) 327–334. https://doi.org/10.5006/0010-9312-7.10.327.

[3] S. Arnold, Repressing the growth of tin whiskers. Plating. 53 (1996) 96–99. https://search-proquest-com.ezproxy.lib.purdue.edu/docview/22261292?accountid=13360.

[4] P.T. Vianco, J.A. Rejent, Dynamic recrystallization (DRX) as the mechanism for Sn whisker development. Part I: A model, J. Electron. Mater. 38 (2009) 1815–1825. https://doi.org/10.1007/s11664-009-0879-z.

[5] T.R. Bieler, H. Jiang, L.P. Lehman, T. Kirkpatrick, E.J. Cotts, B. Nandagopal, Influence of Sn grain size and orientation on the thermomechanical response and reliability of Pb-free solder joints, IEEE Trans. Components Packag. Technol. 31 (2008) 370–381. https://doi.org/10.1109/TCAPT.2008.916835.

[6] B. Zhou, T.R. Bieler, T.K. Lee, K.C. Liu, Methodology for analyzing slip behavior in ball grid array lead-free solder joints after simple shear, J. Electron. Mater. 38 (2009) 2702–2711. https://doi.org/10.1007/s11664-009-0929-6.

[7] R.M. Fisher, L.S. Darken, K.G. Carroll, Accelerated growth of tin whiskers, Acta Metall. 2 (1954). https://doi.org/10.1016/0001-6160(54)90053-X.

[8] K.N. Tu, J.C.M. Li, Spontaneous whisker growth on lead-free solder finishes, Mater. Sci. Eng. A. 409 (2005) 131–139. https://doi.org/10.1016/j.msea.2005.06.074.

[9] N.G. Clore, Identification and counting procedure for tin whiskers, hillocks and other surface defects. M.S. Thesis, Purdue University, West Lafayette, IN, 2011. https://search-proquest-com.ezproxy.lib.purdue.edu/docview/963704909?accountid=13360

[10] J.W. Osenbach, Creep and its effect on Sn whisker growth, J. Appl. Phys. 106 (2009). https://doi.org/10.1063/1.3248277.

[11] C. V. Thompson, Grain growth in polycrystalline thin films of semiconductors, Interface Sci. 6 (1998) 85–93. https://doi.org/10.1023/A:1008616620663.

[12] P. Sarobol, J.E. Blendell, C.A. Handwerker, Whisker and hillock growth via coupled localized Coble creep, grain boundary sliding, and shear induced grain boundary migration, Acta Mater. 61 (2013) 1991–2003. https://doi.org/10.1016/j.actamat.2012.12.019.

[13] M.E. Williams, K.W. Moon, W.J. Boettinger, D. Josell, A.D. Deal, Hillock and whisker growth on Sn and SnCu electrodeposits on a substrate not forming interfacial intermetallic compounds, J. Electron. Mater. 36 (2007) 214–219. https://doi.org/10.1007/s11664-006-0071-7.

[14] A.E. Pedigo, The influence of the effective physical properties of tin electroplated films on the growth of tin whiskers, PhD thesis, Purdue University, West Lafayette, IN, 2011. https://search-proquest-com.ezproxy.lib.purdue.edu/docview/901130588?accountid=1336.

[15] W.J. Choi, T.Y. Lee, K.N. Tu, N. Tamura, R.S. Celestre, A.A. MacDowell, Y.Y. Bong, L. Nguyen, Tin whiskers studied by synchrotron radiation scanning X-ray micro-diffraction, Acta Mater. 51 (2003) 6253–6261. https://doi.org/10.1016/S1359-6454(03)00448-8.

[16] F. Pei, N. Jadhav, E. Chason, Correlating whisker growth and grain structure on Sn-Cu samples by real-time scanning electron microscopy and backscattering diffraction characterization, Appl. Phys. Lett. 100 (2012) 1–5. https://doi.org/10.1063/1.4721661.

[17] W.H. Chen, P. Sarobol, J.R. Holaday, C.A. Handwerker, J.E. Blendell, Effect of crystallographic texture, anisotropic elasticity, and thermal expansion on whisker formation in β-Sn thin films, J. Mater. Res. 29 (2014) 197–206. https://doi.org/10.1557/jmr.2013.378.

[18] N. Jadhav, E. Buchovecky, E. Chason, A. Bower, Real-time SEM/FIB studies of whisker growth and surface modification, Jom. 62 (2010) 30–37. https://doi.org/10.1007/s11837-010-0105-8.

[19] P. Sarobol, A.E. Pedigo, P. Su, J.E. Blendell, C.A. Handwerker, Defect morphology and texture in Sn, Sn-Cu, and Sn-Cu-Pb electroplated films, IEEE Trans. Electron. Packag. Manuf. 33 (2010) 159–164. https://doi.org/10.1109/TEPM.2010.2046172.

[20] J. Smetana, Theory of tin whisker growth: “The end game,” IEEE Trans. Electron. Packag. Manuf. 30 (2007) 11–22. https://doi.org/10.1109/TEPM.2006.890645.

[21] W.J. Boettinger, C.E. Johnson, L.A. Bendersky, K.W. Moon, M.E. Williams, G.R. Stafford, Whisker and hillock formation on Sn, Sn-Cu and Sn-Pb electrodeposits, Acta Mater. 53 (2005) 5033–5050. https://doi.org/10.1016/j.actamat.2005.07.016.

[22] G.T. Galyon, L. Palmer, An integrated theory of whisker formation: The physical metallurgy of whisker formation and the role of internal stresses, IEEE Trans. Electron. Packag. Manuf. 28 (2005) 17–30. https://doi.org/10.1109/TEPM.2005.847443.

[23] Y. Wang, Microstructure evolution and surface defect formation in tin films, PhD thesis, Purdue University, West Lafayette, IN, 2014. https://search-proquest-com.ezproxy.lib.purdue.edu/docview/1615059052?accountid=13360

[24] K.N. Tu, C. Chen, A.T. Wu, Stress analysis of spontaneous Sn whisker growth, J. Mater. Sci. Mater. Electron. 18 (2007) 269–281. https://doi.org/10.1007/s10854-006-9029-z.

[25] J. Cheng, F. Yang, P.T. Vianco, B. Zhang, J.C.M. Li, Optimum thickness of Sn film for whisker growth, J. Electron. Mater. 40 (2011) 2069–2075. https://doi.org/10.1007/s11664-011-1708-8.

[26] E. Chason, N. Jadhav, W.L. Chan, L. Reinbold, K.S. Kumar, Whisker formation in Sn and Pb-Sn coatings: Role of intermetallic growth, stress evolution, and plastic deformation processes, Appl. Phys. Lett. 92 (2008) 1–4. https://doi.org/10.1063/1.2912528.

[27] E. Chason, F. Pei, N. Jain, A. Hitt, Studying the effect of grain size on whisker nucleation and growth kinetics using thermal strain, J. Electron. Mater. 48 (2019) 17–24. https://doi.org/10.1007/s11664-018-6594-x.

[28] J. Shin, E. Chason, Stress behavior of electroplated Sn films during thermal cycling, J. Mater. Res. 24 (2011) 1522–1528. https://doi.org/10.1557/jmr.2009.0172.

[29] S. Jeong, Y. Sato, H. Miura, Mechanical properties of intermetallic compounds formed at the interface between a tin bump and an electroplated copper thin film, 2008 10th Int. Conf. Electron. Mater. Packag. EMAP 2008. (2008) 149–152. https://doi.org/10.1109/EMAP.2008.4784251.

[30] M. Dittes, P. Oberndorff, P. Crema, P. Su, Tin whisker formation - A stress relieve phenomenon, AIP Conf. Proc. 817 (2006) 348–359. https://doi.org/10.1063/1.2173568.

[31] P. Oberndorff, M. Dittes, P. Crema, S. Chopin, Whisker formation on matte Sn influencing of high humidity, Proc. - Electron. Components Technol. Conf. 1 (2005) 429–433. https://doi.org/10.1109/ectc.2005.1441300.

[32] K.N. Tu, Irreversible processes of spontaneous whisker growth in bimetallic Cu-Sn thin-film reactions, Phys. Rev. B. 49 (1994) 2030–2034. https://doi.org/10.1103/PhysRevB.49.2030.

[33] T. Shibutani, J. Wu, Q. Yu, M. Pecht, Key reliability concerns with lead-free connectors, Microelectron. Reliab. 48 (2008) 1613–1627. https://doi.org/10.1016/j.microrel.2008.06.004.

[34] P. Sarobol, Y. Wang, W.H. Chen, A.E. Pedigo, J.P. Koppes, J.E. Blendell, C.A. Handwerker, A predictive model for whisker formation based on local microstructure and grain boundary properties, Jom. 65 (2013) 1350–1361. https://doi.org/10.1007/s11837-013-0717-x.

[35] Y. Wang, J.E. Blendell, C.A. Handwerker, Evolution of tin whiskers and subsiding grains in thermal cycling, J. Mater. Sci. 49 (2014) 1099–1113. https://doi.org/10.1007/s10853-013-7788-5.

[36] P. Adeva, G. Caruana, O.A. Ruano, M. Torralba, Microstructure and high temperature mechanical properties of tin, Mater. Sci. Eng. A. 194 (1995) 17–23. https://doi.org/10.1016/0921-5093(94)09654-6.

[37] T. Kato, C.A. Handwerker, J. Bath, Mitigating tin whisker risks: Theory and practice. IEEE Press. (2016) 228-236. https://onlinelibrary-wiley-com.ezproxy.lib.purdue.edu/doi/pdf/10.1002/9781119011965.

[38] T. Shibutani, Q. Yu, M. Shiratori, M.G. Pecht, Pressure-induced tin whisker formation, Microelectron. Reliab. 48 (2008) 1033–1039. https://doi.org/10.1016/j.microrel.2008.04.009.

[39] P. Darbandi, T.K. Lee, T.R. Bieler, F. Pourboghrat, Crystal plasticity finite element study of deformation behavior in commonly observed microstructures in lead free solder joints, Comput. Mater. Sci. 85 (2014) 236–243. https://doi.org/10.1016/j.commatsci.2014.01.002.

[40] K. Suganuma, A. Baated, K.S. Kim, K. Hamasaki, N. Nemoto, T. Nakagawa, T. Yamada, Sn whisker growth during thermal cycling, Acta Mater. 59 (2011) 7255–7267. https://doi.org/10.1016/j.actamat.2011.08.017.

[41] F. Pei, E. Buchovecky, A. Bower, E. Chason, Stress evolution and whisker growth during thermal cycling of Sn films: A comparison of analytical modeling and experiments, Acta Mater. 129 (2017) 462–473. https://doi.org/10.1016/j.actamat.2017.03.005.

[42] C. Trinks, C.A. Volkert, Transition from dislocation glide to creep controlled damage in fatigued thin Cu films, J. Appl. Phys. 114 (2013). https://doi.org/10.1063/1.4819760.

[43] R. Schwaiger, G. Dehm, O. Kraft, Cyclic deformation of polycrystalline Cu films, Philos. Mag. 83 (2003) 693–710. https://doi.org/10.1080/0141861021000056690.

[44] S.A. Burger, High cycle fatigue of Al and Cu thin films by a novel high-throughput method, PhD thesis, KIT, Germany, 2012. https://doi.org/10.5445/KSP/1000034759.

[45] C. Eberl, R. Spolenak, E. Arzt, F. Kubat, A. Leidl, W. Ruile, O. Kraft, Ultra high-cycle fatigue in pure Al thin films and line structures, Mater. Sci. Eng. A. 421 (2006) 68–76. https://doi.org/10.1016/j.msea.2005.10.007.

[46] O. Kraft, R. Schwaiger, P. Wellner, Fatigue in thin films: Lifetime and damage formation, Mater. Sci. Eng. A. 319–321 (2001) 919–923. https://doi.org/10.1016/S0921-5093(01)00990-X.

[47] M.A. Hopcroft, W.D. Nix, T.W. Kenny, What is the Young's modulus of silicon?, J. Microelectromechanical Syst. 19 (2010) 229–238. https://doi.org/10.1109/JMEMS.2009.2039697.

[48] A. Erturk, P.A. Tarazaga, J.R. Farmer, D.J. Inman, Effect of strain nodes and electrode configuration on piezoelectric energy harvesting from cantilevered beams, J. Vib. Acoust. Trans. ASME. 131 (2009) 0110101–01101011. https://doi.org/10.1115/1.2981094.

[49] U. Rabe, K. Janser, W. Arnold, Vibrations of free and surface-coupled atomic force microscope cantilevers: Theory and experiment, Rev. Sci. Instrum. 67 (1996) 3281–3293. https://doi.org/10.1063/1.1147409.

[50] E. Chason, N. Jadhav, F. Pei, Effect of layer properties on stress evolution, intermetallic volume, and density during tin whisker formation, Jom. 63 (2011) 62–68. https://doi.org/10.1007/s11837-011-0178-z.

[51] J.G. Lee, A. Telang, K.N. Subramanian, T.R. Bieler, Modeling thermomechanical fatigue behavior of Sn-Ag solder joints, J. Electron. Mater. 31 (2002) 1152–1159. https://doi.org/10.1007/s11664-002-0004-z.

[52] K.P. Venkatesh, R. Pratap, Capturing higher modes of vibration of micromachined resonators, J. Phys. Conf. Ser. 181 (2009). https://doi.org/10.1088/1742-6596/181/1/012079.

[53] O.B. Ozdoganlar, B.D. Hansche, T.G. Carne, Experimental modal analysis for microelectromechanical systems, Exp. Mech. 45 (2005) 498–506. https://doi.org/10.1177/0014485105059991.

[54] L. Meinshausen, S. Bhassyvasantha, B.S. Majumdar, I. Dutta, Influence of indium addition on whisker mitigation in electroplated tin coatings on copper substrates, J. Electron. Mater. 45 (2016) 791–801. https://doi.org/10.1007/s11664-015-4204-8.

[55] S. Bhassyvasantha, N. Fredj, S.D. Mahapatra, W. Jennings, I. Dutta, B.S. Majumdar, Whisker mitigation mechanisms in indium-doped tin thin films: Role of the surface, J. Electron. Mater. 47 (2018) 6229–6240. https://doi.org/10.1007/s11664-018-6522-0.

[56] E. Chason, F. Pei, Measuring the stress dependence of nucleation and growth processes in Sn whisker formation, Jom. 67 (2015) 2416–2424. https://doi.org/10.1007/s11837-015-1557-7.

[57] F. Yang, J.C.M. Li, Deformation behavior of tin and some tin alloys, J. Mater. Sci. Mater. Electron. 18 (2007) 191–210. https://doi.org/10.1007/s10854-006-9016-4.

[58] F. Pei, E. Chason, In situ measurement of stress and whisker/hillock density during thermal cycling of Sn layers, J. Electron. Mater. 43 (2014) 80–87. https://doi.org/10.1007/s11664-013-2878-3.

[59] S. Burger, C. Eberl, A. Siegel, A. Ludwig, O. Kraft, A novel high-throughput fatigue testing method for metallic thin films, Sci. Technol. Adv. Mater. 12 (2011). https://doi.org/10.1088/1468-6996/12/5/054202.

[60] S.E. Koonce, S.M. Arnold, Growth of metal whiskers, J. Appl. Phys. 24 (n.d.) 365–366. https://doi.org/10.1063/1.1721283.

[61] G.T.T. Sheng, C.F. Hu, W.J. Choi, K.N. Tu, Y.Y. Bong, L. Nguyen, Tin whiskers studied by focused ion beam imaging and transmission electron microscopy, J. Appl. Phys. 92 (2002) 64–69. https://doi.org/10.1063/1.1481202.

[62] R.L. Coble, A Model for boundarydiffusion controlled creep inpolycrystalline materials, J. Appl. Phys. 34 (1963) 1679–1682. https://doi.org/10.1063/1.1702656.

[63] R. Raj, M.F. Ashby, On grain boundary sliding and diffusional creep, Metall. Trans. 2 (1971) 1113–1127. https://doi.org/10.1007/BF02664244.

[64] N.Y. Genin, Effect of stress on grain boundary motion in thin films, J. Appl. Phys. 77 (1995) 5130–5137. https://doi.org/10.1016/j.actamat.2010.09.067.

[65] G. Fox-Rabinovich, J.M. Paiva, I. Gershman, M. Aramesh, D. Cavelli, K. Yamamoto, G. Dosbaeva, S. Veldhuis, Control of self-organized criticality through adaptive behavior of nano-structured thin film coatings, Entropy. 18 (2016). https://doi.org/10.3390/e18080290.

[66] E. Altshuler, T.H. Johansen, Y. Paltiel, P. Jin, K.E. Bassler, O. Ramos, Q.Y. Chen, G.F. Reiter, E. Zeldov, C.W. Chu, Vortex avalanches with robust statistics observed in superconducting niobium, Phys. Rev. B - Condens. Matter Mater. Phys. 70 (2004) 2–5. https://doi.org/10.1103/PhysRevB.70.140505.

[67] J. Bowman, M.B. Barker, A methodology for describing creep-fatigue interactions in thermoplastic components, Polym. Eng. Sci. 26 (1986) 1582–1590. https://doi.org/10.1002/pen.760262209.

[68] K. Nakai, T. Sakamoto, S. Kobayashi, M. Takamizawa, K. Murakami, M. Hino, A model for nucleation of tin whisker through dislocation behavior, J. Phys. Conf. Ser. 165 (2009) 1–5. https://doi.org/10.1088/1742-6596/165/1/012089.

[69] J.P. Koppes, Effect of crystallographic orientation on hiillock formation in thermally cycled large grain tin films, PhD thesis, Purdue University, West Lafayette, IN, 2014. https://search.proquest.com/docview/1220885508?accountid=13360.

[70] A. Tasooji, L. Lara, K. Lee, Effect of grain boundary misorientation on electromigration in lead-free solder joints, J. Electron. Mater. 43 (2014) 4386–4394. https://doi.org/10.1007/s11664-014-3321-0.

[71] P.J.E. Forsyth, Exudation of material from slip bands at the surface of fatigued crystals of an aluminium-copper alloy, Nature. 171 (1953) 172–173. https://doi.org/10.1038/171172a0.

[72] P. Lukáš, L. Kunz, Role of persistent slip bands in fatigue, Philos. Mag. 84 (2004) 317–330. https://doi.org/10.1080/14786430310001610339.

[73] K.S. Kumar, L. Reinbold, A.F. Bower, E. Chason, Plastic deformation processes in Cu/Sn bimetallic films, J. Mater. Res. 23 (2008) 2916–2934. https://doi.org/10.1557/JMR.2008.0351.

[74] J.K. Wright, J.A. Simpson, R.N. Wright, L.J. Carroll, T.L. Sham, Strain rate sensitivity of alloys 800H and 617, Am. Soc. Mech. Eng. Press. Vessel. Pip. Div. PVP. 1 A (2013). https://doi.org/10.1115/PVP2013-98045.

[75] Y. Lee, C. Basaran, Molecular dynamics of viscoplasticity in β-tin lattice and grain boundary, Comput. Mater. Sci. 68 (2013) 290–296. https://doi.org/10.1016/j.commatsci.2012.10.029.

[76] R.A. Shenoi, H.G. Allen, S.D. Clark, Cyclic creep and creep-fatigue interaction in sandwich beams, J. Strain Anal. Eng. Des. 32 (1997) 1–18. https://doi.org/10.1243/0309324971513175.

[77] A.A. El-Daly, A.E. Hammad, G.S. Al-Ganainy, A.A. Ibrahiem, Design of lead-free candidate alloys for low-temperature soldering applications based on the hypoeutectic Sn-6.5Zn alloy, Mater. Des. 56 (2014) 594–603. https://doi.org/10.1016/j.matdes.2013.11.064.

[78] B. Philippi, C. Kirchlechner, J.S. Micha, G. Dehm, Size and orientation dependent mechanical behavior of body-centered tetragonal Sn at 0.6 of the melting temperature, Acta Mater. 115 (2016) 76–82. https://doi.org/10.1016/j.actamat.2016.05.055.

[79] V.M. Chernov, B.K. Kardashev, K.A. Moroz, Low-temperature embrittlement and fracture of metals with different crystal lattices – Dislocation mechanisms, Nucl. Mater. Energy. 9 (2016) 496–501. https://doi.org/10.1016/j.nme.2016.02.002.

[80] M.A. Bhatia, M. Azarnoush, I. Adlakha, G. Lu, K.N. Solanki, Dislocation core properties of β-tin: A first-principles study, Model. Simul. Mater. Sci. Eng. 25 (2017). https://doi.org/10.1088/1361-651X/aa57d0.

[81] S.J. Hwang, Y.D. Lee, Y.B. Park, J.H. Lee, C.O. Jeong, Y.C. Joo, In situ study of stress relaxation mechanisms of pure Al thin films during isothermal annealing, Scr. Mater. 54 (2006) 1841–1846. https://doi.org/10.1016/j.scriptamat.2006.02.024.

[82] M. Mashita, Hillock growth in thin aluminum films, Shinku/Journal Vac. Soc. Japan. 15 (1972) 196–204. https://doi.org/10.3131/jvsj.15.196.

[83] E.E.M. Noor, N.M. Sharif, C.K. Yew, T. Ariga, A.B. Ismail, Z. Hussain, Wettability and strength of In-Bi-Sn lead-free solder alloy on copper substrate, J. Alloys Compd. 507 (2010) 290–296. https://doi.org/10.1016/j.jallcom.2010.07.182.

[84] V.T. Gillard, W.D. Nix, L.B. Freund, Role of dislocation blocking in limiting strain relaxation in heteroepitaxial films, J. Appl. Phys. 76 (1994) 7280–7287. https://doi.org/10.1063/1.358013.

[85] C.L. Rodekohr, G.T. Flowers, J.C. Suhling, M.J. Bozack, Influence of substrate surface roughness on tin whisker growth, Electr. Contacts, Proc. Annu. Holm Conf. Electr. Contacts. (2008) 245–248. https://doi.org/10.1109/HOLM.2008.ECP.51.

[86] G. Milad, The elimination of whiskers from electroplated tin, Circuit World. 37 (2011) 10–15. https://doi.org/10.1108/03056121111180848.

[87] W. Zhang, A. Egli, F. Schwager, N. Brown, Investigation of Sn-Cu intermetallic compounds by AFM: New aspects of the role of intermetallic compounds in whisker formation, IEEE Trans. Electron. Packag. Manuf. 28 (2005) 85–93. https://doi.org/10.1109/TEPM.2005.847441.

[88] W.H. Chen, P. Sarobol, C.A. Handwerker, J.E. Blendell, Heterogeneous stress relaxation processes at grain boundaries in high-Sn solder films: Effects of Sn anisotropy and grain geometry during thermal cycling, Jom. 68 (2016) 2888–2899. https://doi.org/10.1007/s11837-016-2070-3.

# VITA

Xi Chen was born in Henan, China in 1989. In 2008, she graduated from No. 1 High School of Zhongyuan Oilfield in Puyang, Henan. She continued her education and received her B.S. degree in Materials Science and Engineering from Harbin Institute of Technology in July 2012. With exam-waive and scholarship from Northwestern Polytechnical University (NWPU), she received her M.S degree in Materials Science in March 2015. During her Master's studies, she worked as a graduate research assistant at Science and Technology on Thermostructural Composite Materials Laboratory at NWPU, conducting research on materials preparation and characterization of super high temperature composite ceramics.

In August 2015, Xi came to Purdue University to pursue her PhD in Materials Engineering, advised by Prof. Carol A. Handwerker and John E. Blendell. Her research focused on mechanisms of various kinds of surface defects on tin films during cyclic bending by quantitative analysis. She presented her work at several conferences, including M S&T, Gordon Research Conference and Microelectronics Integrity Meeting (MIM). She will finish her PhD in August 2020.